Katja Rademaker

Rare Earth-Doped Alkali-Lead-Halide Laser Crystals of Low-Phonon Energy

Rare Earth-Doped Alkali-Lead-Halide Laser Crystals of Low-Phonon Energy

Dissertation

Zur Erlangung des Doktorgrades
des Fachbereichs Physik
der Universität Hamburg

vorgelegt von
Katja Rademaker
aus Hamburg

Hamburg,
2005

Bibliografische Information Der Deutschen Bibliothek
Die Deutsche Bibliothek verzeichnet diese Publikation in der Deutschen Nationalbibliografie; detaillierte bibliografische Daten sind im Internet über http://dnb.ddb.de abrufbar.
1. Aufl. - Göttingen : Cuvillier, 2005
Zugl.: Hamburg, Univ., Diss., 2005
ISBN 3-86537-652-5

Gutachter der Dissertation:	Prof. Dr. Günter Huber
	Dr. Stephen A. Payne
Gutachter der Disputation:	Prof. Dr. Günter Huber
	Prof. Dr. Ernst Heumann
Datum der Disputation:	8. April 2005
Vorsitzender des Prüfungsausschusses:	Dr. Klaus Petermann
Vorsitzender des Promotionsausschusses:	Prof. Dr. Günter Huber
Dekan des Fachbereichs Physik:	Prof. Dr. Günter Huber

Nonnenstieg 8, 37075 Göttingen
Telefon: 0551-54724-0
Telefax: 0551-54724-21
www.cuvillier.de

1. Auflage, 2005
Gedruckt auf säurefreiem Papier

ISBN 3-86537-652-5

Abstract

Katja Rademaker,

Rare Earth-Doped Alkali-Lead-Halide Laser Crystals of Low-Phonon Energy

In the context of this study two moisture-resistant bromide host crystals of low-phonon energy doped with the rare earth ions Nd^{3+}, Tb^{3+}, and Eu^{3+} are identified, studied, and their low nonradiative rate is exploited to lase new transitions: potassium-lead-bromide (KPb_2Br_5, KPB) and rubidium-lead-bromide ($RbPb_2Br_5$, RPB). The low multiphonon decay rate and other favorable features render them particularly useful as promising candidates for long wavelength-infrared applications.

Laser activity is achieved with Nd^{3+}-doped KPB and RPB crystals at room temperature. Conventional laser activity at 1.07 µm is observed, as well as laser operation at the new wavelengths 1.18 µm and 0.97 µm resulting from the $^4F_{5/2}+^2H_{9/2}\rightarrow{}^4I_J$ transitions (J=13/2 and 11/2) for the first time for any crystal. Pump-probe spectra are presented to discuss excited state absorption and reabsorption competing with e.g. (laser) emission transitions, as well as depopulation mechanisms of the lower laser levels. Cross relaxation from e.g. the $^4I_{13/2}$ lower laser level is evidenced, providing a pathway for enhanced efficiency of operation for e.g. the 1.18 µm transition. Bright upconversion fluorescence observed in these crystals could also enable short-wavelength lasing. Directly pumpable, broadband 8 µm emission is measured in Tb:KPB samples in addition to 3 µm and 5 µm luminescence due to reduced multiphonon relaxation rates. Emission from the potential 10 µm laser level is also observed.

Detailed spectroscopic investigations at room temperature and below are carried out in this study to characterize these materials and to determine their laser potential. For the same purpose, radiative transition probabilities are calculated and compared with experimentally determined values for relevant (laser) transitions. Beside radiative transition rates nonradiative rates are obtained and fitted to measured rates in order to determine the influence of multiphonon decay and the presence of further quenching mechanisms.

Kurzdarstellung

Katja Rademaker, *Rare Earth-Doped Alkali-Lead-Halide Laser Crystals of Low-Phonon Energy (Selten-Erd-dotierte Alkali-Blei-Halogenid Laserkristalle niedriger Phononenenergie)*

Im Rahmen dieser Arbeit sind mit Kalium-Blei-Bromid (KPb_2Br_5, KPB) und Rubidium-Blei-Bromid ($RbPb_2Br_5$, RPB) feuchtigkeitsbeständige, bromidische Wirtskristalle niedriger Phononenenergie - dotiert mit den Selten-Erd Ionen Nd^{3+}, Tb^{3+} und Eu^{3+} - identifiziert, untersucht und deren niedrige nichtstrahlende Rate dazu genutzt worden, um neue Laserübergänge zu realisieren. Insbesondere die niedrige Multiphononenzerfallsrate lassen diese Materialien besonders für Anwendungen im langwelligen Spektralbereich vielversprechend erscheinen.

Laseraktivität bei Raumtemperatur konnte mit Nd^{3+}-dotierten KPB- und RPB-Kristallen erzielt werden. Neben der Laseraktivität bei 1.07 µm konnte zum ersten Mal in einem Kristall Laseraktivität bei den Wellenlängen 1.18 µm und 0.97 µm, die aus den Übergängen $^4F_{5/2}+^2H_{9/2}\rightarrow{}^4I_J$ (J=13/2 und 11/2) resultieren, nachgewiesen werden. Pump-Probe Spektren werden gezeigt, um die Absorption aus angeregten Zuständen und die Reabsorption zu diskutieren, die u.a. mit den (Laser-)Emissionsübergängen konkurrieren. Zudem werden Entleerungsmechanismen der unteren Laserniveaus diskutiert, wobei u.a. die Kreuzrelaxation von dem unteren $^4I_{13/2}$ Laserniveau nachgewiesen werden konnte. Diese verbessern die Effizienz der Lasertätigkeit für zum Beispiel den 1.18 µm Übergang. Stark leuchtende Upconversion-Fluoreszenz, die in diesen Kristallen beobachtet wurde, könnte Lasertätigkeit im kurzwelligen Spektralbereich ermöglichen. Direkt anregbare, breitbandige 8 µm Emission ist zusätzlich zu der 3 µm und 5 µm Lumineszenz in Tb:KPB Proben gemessen worden, was aus der reduzierten Multiphononenrelaxationsrate in diesen Kristallen resultiert. Emission aus dem potentiellen 10 µm Laser-Emissionsniveau wurde ebenfalls beobachtet.

Detaillierte spektroskopische Untersuchungen bei Raumtemperatur und niedrigeren Temperaturen sind durchgeführt worden, um diese Materialien zu charakterisieren und ihr Laserpotential zu bestimmen. Aus demselben Grund sind strahlende Übergangswahrscheinlichkeiten kalkuliert und mit den experimentell bestimmten Werten relevanter (Laser-)Übergänge verglichen worden. Neben den strahlenden Übergangsraten sind nichtstrahlende Raten bestimmt und an die gemessenen Raten angepasst worden, um den Einfluss des Multiphononenzerfalls und die Anwesenheit weiterer nichtstrahlender Zerfallskanäle zu bestimmen.

Parts of this thesis are published/submitted or are in preparation:

1. K. Rademaker, S.A. Payne, G. Huber, E. Heumann, W.F. Krupke, *New laser transitions for Nd-doped low-phonon frequency hosts*, submitted for U.S. Patent, 2004

2. K. Rademaker, E. Heumann, S.A. Payne, G. Huber, W.F. Krupke, S. Kueck, L.I. Isaenko, A. Burger, *Laser activity at 1.18, 1.07, and 0.97 μm and possible depopulation mechansims of the lower laser levels in Nd^{3+}-doped KPb_2Br_5 and $RbPb_2Br_5$*, Conference on Lasers and Electro-Optics (CLEO), Baltimore, USA, 2005

3. K. Rademaker, S.A. Payne, G. Huber et al., *Temperature dependent nonradiative decay of RE^{3+}-doped KPb_2Br_5*, in preparation

4. K. Rademaker, G. Huber, S.A. Payne, E. Osiac, L.I. Isaenko, *Optical pump-probe processes and depopulation mechanisms of the lower laser levels in Nd^{3+}-doped KPb_2Br_5, $RbPb_2Br_5$, and KPb_2Cl_5*, accepted for JOSA B, 2005

5. K. Rademaker, E. Heumann, G. Huber, S.A. Payne, W.F. Krupke, L.I. Isaenko, A. Burger, *Laser activity at 1.18, 1.07, and 0.97 μm in the low-phonon energy crystalline hosts KPb_2Br_5 and $RbPb_2Br_5$ doped with Nd^{3+}*, Opt. Lett. 30, no. 7, 2005

6. U.N. Roy, R.H. Hawrami, Y. Cui, S. Morgan, A. Burger, K.C. Mandal, C.C. Noblitt, S. Speakman, K. Rademaker, S.A. Payne, *Tb^{3+}-doped KPb_2Br_5: a low-phonon mid-IR laser crystal*, Appl. Phys. Lett. 86, 151911, 2005

7. A.M. Tkachuk, S.E. Ivanova, K. Rademaker, L.I. Isaenko, V.P. Gapontsev, *Upconversion processes in Nd^{3+}-doped KPb_2Cl_5, KPb_2Br_5 and $RbPb_2Br_5$ potential laser crystals*, XII Feovilov Symposium, Yekaterinburg, Russia, 2004

8. A.M. Tkachuk, K. Rademaker, et al., *Upconversion processes in Nd^{3+}-doped KPb_2Cl_5, KPb_2Br_5 and $RbPb_2Br_5$ laser crystals*, Opt. and Spectr., in preparation

9. K. Rademaker, W.F. Krupke, R.H. Page, S.A. Payne, K. Petermann, G. Huber, A.P. Yelisseyev, L.I. Isaenko, U.N. Roy, A. Burger, K.C. Mandal, K. Nitsch, *Optical properties of Nd^{3+}- and Tb^{3+}-doped KPb_2Br_5 and $RbPb_2Br_5$ with low nonradiative decay*, J. Opt. Soc. Am. B 21, no. 12, 2117-2129 (2004)

10. K. Rademaker, K. Petermann, G. Huber, W.F. Krupke, R.H. Page, S.A. Payne, A.P. Yelisseyev, L.I. Isaenko, U.N. Roy, A. Burger, K.C. Mandal, K. Nitsch, *Slow nonradiative decay for rare earths in KPb_2Br_5 and $RbPb_2Br_5$*, Advanced Solid State Photonics (ASSP), Topical Meeting 19, Opt. Soc. Am., Techn. Dig. WB-10, Santa Fe, New Mexico, USA, 2004

Table of Contents

1. Introduction

1.1 Motivation and Background

Long Wavelength Infrared (LWIR) Lasers are of great interest as beneficial sources for remote sensing in the vibrational fingerprint region (pollution monitoring), thermal scene illumination, and infrared spectroscopy in clinical and diagnostic analysis etc. Especially, broadly tunable LWIR laser sources can enable e.g. the detection of various gaseous species that arise both naturally and as by-products of our technological society (Figure 1-1). In particular solid-state lasers are feasible as coherent light sources, because of their compactness, efficiency, brightness, ease of deployment, reliability as well as low fabrication and maintenance costs. Here, rare earth ions as active dopants are advantageous since their energy level structure principally shows energy gaps in the LWIR region (Fig. 1-2) and they have absorption bands to pump the LWIR transitions directly with pump sources readily available on the market (such as diodes). The coverage of a broad wavelength region could in principle be possible with rare earth ions as indicated in Fig. 1-1.

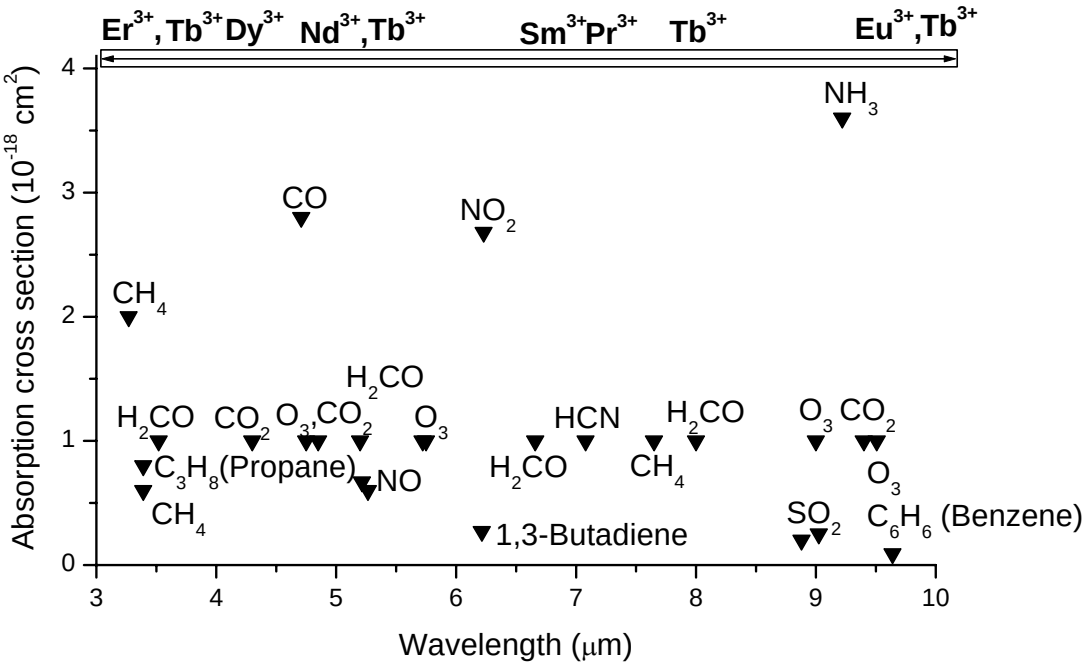

Fig. 1-1. *Absorption cross section of different gaseous species (based on data in [Mea82],[Pla65],[Pug76]). Rare earth-doped low-phonon energy laser host matrices could provide a way for the detection of e.g. pollution gases in the wavelength region 3-10 μm. Possible trivalent rare earth ions are indicated. Gas species of not clearly identified cross section are set to 1x10^{-18} cm^2.*

Currently, more complex and expensive systems such as optical parametric oscillators (OPOs) operate in the wavelength region of interest like e.g. one of the atmospheric transmission windows at ~ 8-13 µm (Appendix A, Fig. A-1). In this context other competitive coherent light sources such as gas lasers (like CO_2) and quantum-cascade (QC) diode lasers ([Fai94], [Bec03], [Pfl03]) have to be noted. However, they show limitations regarding e.g. tunability, efficiency, and/or average power.

Thus, mainly for the purpose mentioned above, herein the potential of rare earth-doped potassium-lead-bromide (KPb_2Br_5 or KPB) and rubidium-lead-bromide ($RbPb_2Br_5$ or RPB) crystals as new solid-state laser host materials is explored.

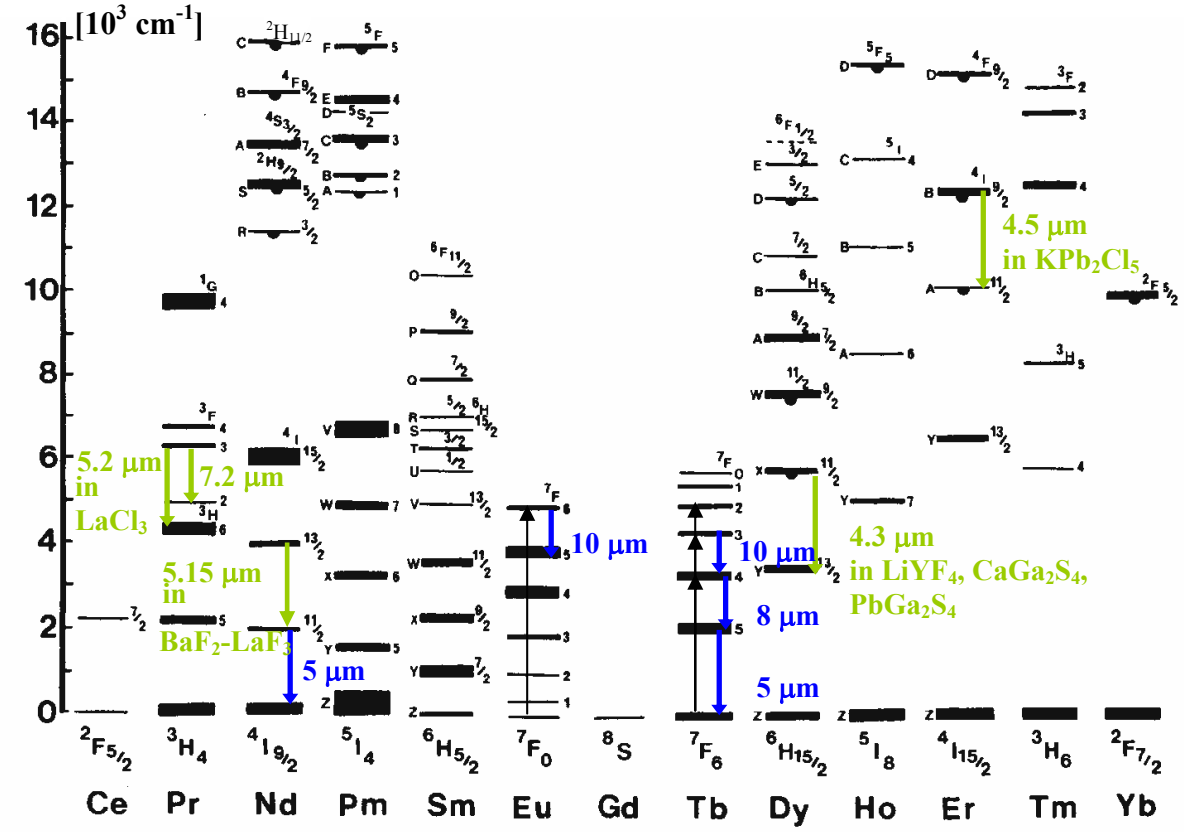

Fig. 1-2. *Energy level diagram of trivalent rare earth ions [Die68]: Room-temperature, solid-state laser transitions beyond 4 µm are rare (green) ([Bow96], [Nos99], [Bow01],[Bas05], [Kam96]). Thus, the investigation of rare earth-doped low-phonon energy host matrices could reveal further (mainly directly pumpable) LWIR laser transitions as indicated (blue) for some transitions of the RE^{3+} ions of this study.*

To achieve acceptable quantum efficiency from a given energy level a rule of thumb demands that at least four to six (maximal energy) phonons span the energy gap to the next lowest level. Otherwise the luminescence is quenched, as it is typical for most fluorides and oxides emitting at wavelengths longer than 4 µm (with maximum phonon energies in excess of

500 cm^{-1}). Solid state lasers beyond 4 μm at room temperature are indicated in Fig. 1-2. As can be seen, laser transitions in the long wavelength region are still rare. Until now the longest laser wavelength in a solid state laser material at room temperature (7.2 μm, Figure 1-2) has been achieved with the low-phonon energy host lanthanum chloride ($LaCl_3$) doped with Pr^{3+} [Bow96]. This chloride host has the disadvantage of being highly hygroscopic, and somewhat impractical. So, it was an important step towards practicality when potassium-lead-chloride (KPb_2Cl_5 or KPC) was identified as a moisture-resistant, low-phonon energy host for mid-IR-applications ([Pag97], [Nos98], [Isa98], [Tka99a], [Tka99b]). In KPC laser operation has been achieved with the rare earth ions Nd^{3+} (1.06 μm) [Nos00a], Dy^{3+} (2.43 μm) [Nos99], and Er^{3+} (1.7 μm, 4.5 μm (Fig. 1-2)) [Bow01].

Further spectroscopic investigations of RE^{3+}-doped KPC crystals have been performed with Pr^{3+} ([Bal02], [Tka02a], [Bal03a], [Bas02]), Nd^{3+} ([Tka02a], [Jen01], [Bas02], [Jen02], [Tka02b]), Tb^{3+} ([But02], [Tka02a]), Er^{3+} ([Tka02a], [Jen03], [Tka03], [Roy03]), Dy^{3+} ([Nos01], [Tig01]), and Ho^{3+} [Tka02a] as well as for doubly-doped systems like Pr^{3+}, Yb^{3+} [Bal03b] and Tb^{3+}, Tm^{3+} [Okh03] in order to evaluate the possibilities of long wavelength laser transitions and to study energy transfer mechanisms and upconversion of this low-phonon energy host material.

The alkali-lead-halide host crystals KPB and RPB reported in this study evidence similar properties to KPC (incorporate rare earth ions, moisture-resistant, transparent in the wavelength region of interest etc.), but with the added advantage of even lower phonon energies (because of the higher mass of the vibrating bromine constituent) with values of ~ 140 cm^{-1} (section 3.1). The vibrational energy is most simply described by

$$\bar{\nu}_{vibr}=(k/\mu)^{1/2}, \qquad (1\text{-}1)$$

where k is an effective force constant and μ is the reduced mass of the vibrating constituents. Therefore, the phonon energy is roughly expected to be ~ 1.5x smaller as one passes the periodic table from chloride to bromide anions. This will minimize the nonradiative decay due to multiphonon interactions, in principle permitting lasing at new wavelengths, e.g. in the LWIR region (perhaps as long as 10 μm), since electronic states which are immediately depleted in oxides and fluorides become metastable. For the same reason new pathways for upconversion lasing can occur.

Here, main focus is on the spectroscopic investigation of Nd^{3+}-doped KPB and RPB as well as Tb^{3+}- and Eu^{3+}-doped KPB with respect to its potential as a new solid state laser material. For example this could mean the possibility of the achievement of LWIR lasing up to 10 μm

in wavelength with dopant ions like Tb^{3+} for example (Fig. 1-2) and also lasers operating at new wavelengths e.g. in the visible or near infrared (e.g. 1.2 µm for Nd-doped MPb_2Br_5 (M=K, Rb)). Laser operation of the latter one will actually be presented in this study. A few of the investigated transitions and processes presented and further described in the following study are illustrated for the rare earth ion Nd^{3+} in Fig. 1-3. This includes emission (EM), excited state absorption (ESA), energy transfer upconversion (ETU), reabsorption (RA), lasing (⇝), and cross relaxation (CR) as well as the influence of multiphonon relaxation (MPR). Ground state absorption (GSA) is not displayed in the figure.

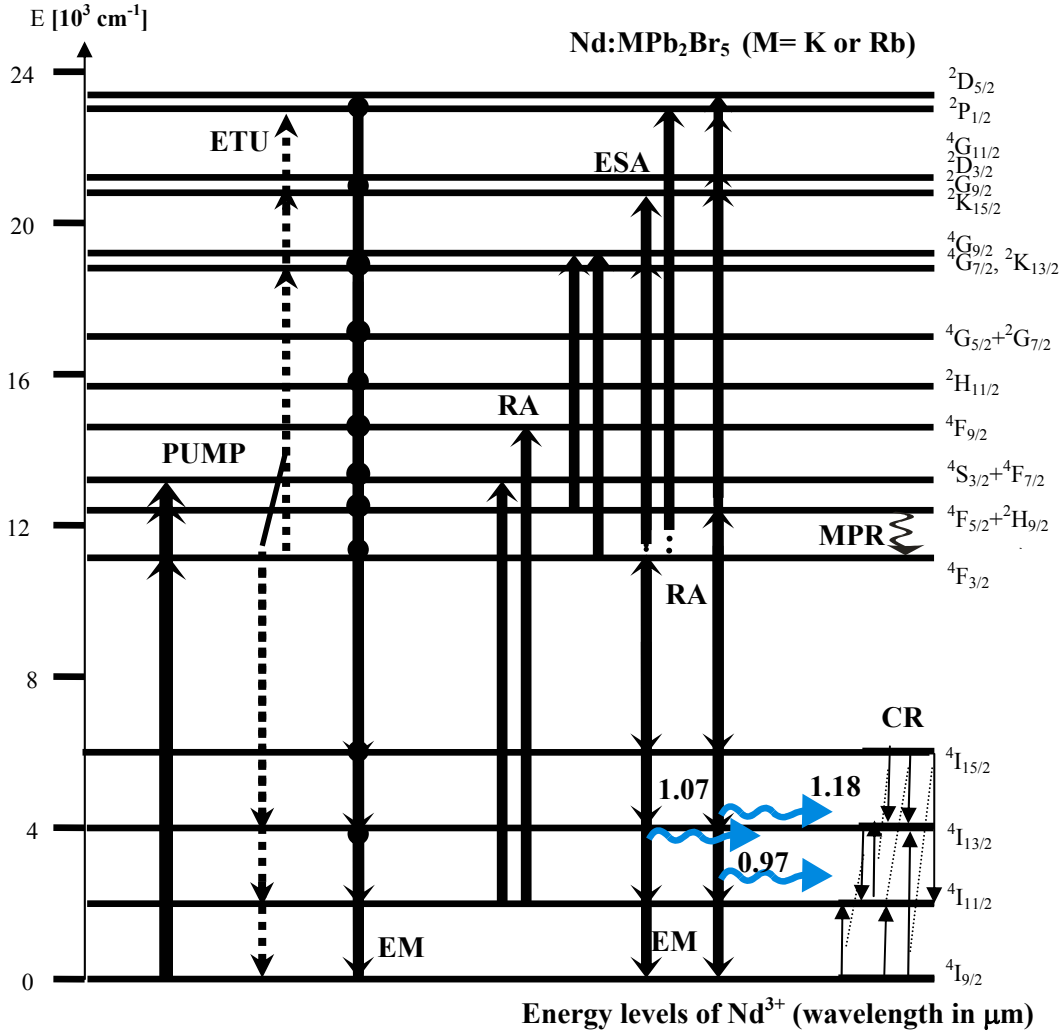

Fig. 1-3. *For illustration, the energy level diagram of Nd:MPB (M= K or Rb) displays some pumping and emitting levels of this study. Laser activity (⇝) will be presented for the first time in moisture-resistant, bromide host crystals of low-phonon energy, also at new wavelengths (with Nd:RPB) for the first time in any crystal. Some of the discussed transitions based on processes such as emission (EM), excited state absorption (ESA), energy transfer upconversion (ETU), cross relaxation (CR), reabsorption (RA), and multiphonon relaxation (MPR) are also indicated. The measured ground state absorption (GSA) and pumping into higher lying levels is not included.*

During the course of this study spectroscopic investigations on the KPB host crystal doped with Er^{3+} and Nd^{3+} have also been presented by Hoemmerich et al. ([Hoe04], [Hoe05]).

This work is structured in 4 chapters. The following section of this first chapter gives a brief overview of the most important theoretical aspects of this thesis. The preparation including crystal growth and physical properties of the rare earth-doped bromide crystals as well as experimental methods used in this study are described in chapter 2.

The results of the spectroscopic investigation and laser operation are described and discussed in chapter 3. The first section of this chapter states the low-phonon energy of the investigated bromide crystals in comparison to other host materials. As a result, nonradiative (multiphonon) decay competes less effectively with the radiative decay in the investigated bromide materials compared with e.g. the chloride analogs as described in section 3.2. Here, the study of slow nonradiative decay includes absorption spectra, emission spectra, emission lifetimes recorded for Nd^{3+}-, Tb^{3+}- and partly Eu^{3+}-doped MPb_2Br_5 (M=Rb, K) samples at room temperature as well as calculations of cross sections, Judd-Ofelt parameters, radiative transition probabilities for relevant (laser) transitions, and multiphonon decay rates.

Nonradiative decay like e.g. multiphonon emission is a temperature dependent process. Thus, temperature dependent quenching is investigated in section 3.3 for long wavelength transitions of Tb^{3+}-doped KPB samples including an approach to fit the temperature dependency of the decay. This provides a way to evidence the energy (and number) of phonons involved in the process which will be compared with the results stated in previous sections. In this context emission from the potential 10 μm emitting level in Tb^{3+}-doped KPB is investigated. Multiphonon fitting parameters characteristic for the host material are also obtained. Low temperature spectroscopy for Nd^{3+}-doped KPB will be presented in section 3.4 where the main purpose was to determine the Stark levels. This is beneficial e.g. for the determination of transition wavelengths which are particularly used in following sections about optical pump-probe processes and upconversion.

Laser results obtained from rare earth-doped KPB and RPB samples will be given in section 3.5. Here, laser activity resulting from new transitions in Nd^{3+}-doped bromide samples is presented which makes also lasing e.g. in the long wavelength-IR region with these materials promising. The main purpose of the study in section 3.6 is to gain further insights into the lasing potential of Nd^{3+} in RPB and KPB, especially for the new laser wavelengths stated in the previous section. Cw pump-probe spectra are presented in order to discuss excited state absorption (ESA) and reabsorption processes (RA) due to the long lived lower laser levels competing with gain, as well as possible depopulation mechanisms feasible for more efficient

laser operation in these bromide crystals. Line strengths of induced electric dipole and of magnetic dipole transitions and effective cross sections of ESA and RA transitions competing with the (laser) emission transitions, as well as cross relaxation (CR) processes among the lower laser levels, will be given. For comparison pump-probe spectra will also be presented for the potassium-lead-chloride host (Nd^{3+}:KPC). The presence of upconversion as illustrated for Nd^{3+}-doped KPB in section 3.7 could lead in principle to the possibility of upconversion lasing. In chapter 4 the results are summarized.

1.2 Theoretical Aspects

In this section a brief overview of the most important theoretical aspects will be presented accompied by references for a detailed study.

1.2.1 Energy Splitting of Trivalent Rare Earth Ions

The active dopant ions Nd^{3+}, Eu^{3+}, and Tb^{3+} discussed in this study are trivalent lanthanide ions. Their electron configuration is given by [Xe]$4f^3$ (Nd^{3+}), [Xe]$4f^6$ (Eu^{3+}), and [Xe]$4f^8$ (Tb^{3+}), respectively [Hoe79].[1] One characteristic is the unfilled 4f shell, which is shielded by the closed $5s^2$ and $5p^6$ Xenon [Xe] orbitals as often represented in the literature by the radial charge distribution of the electrons as a function of the distance to the nucleus [Wyb65]. Therefore, the influence of the crystalline field can be treated as an external small perturbation of the free ion Hamiltonian as described in [Hen89] and the linewidth of the luminescence transitions in the 4f shell of RE^{3+} (RE=rare earth) ions is usually smaller than for transition metals or 4f↔5d transitions of RE^{3+} ions where the electron-phonon coupling is stronger. The configuration coordination model [Hen89] and the ligand-field theory ([Sch80], [Sch73]) explain these differences.[2] Line broadening of the 4f transitions can occur if e.g. the rare earth ion is incorporated on various sides of the crystalline host, if there are crystal defects present etc. [Hen89].

The splitting of the energy and their degeneracy is illustrated in Figure 1-4 indicating the influence of the different Hamilton operators involved (as further described in Henderson&Imbusch [Hen89]). Here, as well as in the energy level schemes shown for the different active dopant ions in following sections (Figs. 3-3, 3-7, 3-11) the different states are indicated after Russell-Sanders coupling (LS-coupling), where the sum of total orbital momentum $\vec{L} = \sum_i \vec{l}_i$ and total spin momentum $\vec{S} = \sum_i \vec{s}_i$ of all electrons i is added to form the total angular momentum $\vec{J} = \vec{L} + \vec{S}$ [Sch88]. Note, that in the case of approximately equal

[1] [Xe]-electron configuration:$1s^2 2s^2 2p^6 3s^2 3p^6 3d^{10} 4s^2 4p^6 4d^{10} 5s^2 5p^6$
[2] also described in the authors diploma thesis [Rad00]

quantity of Coulomb interaction and spin-orbit coupling term, mixing of different LS-states with the same quantum number J appears and therefore, the free ion states are actually linear combinations of different LS-states, so called intermediate coupling [Con70].

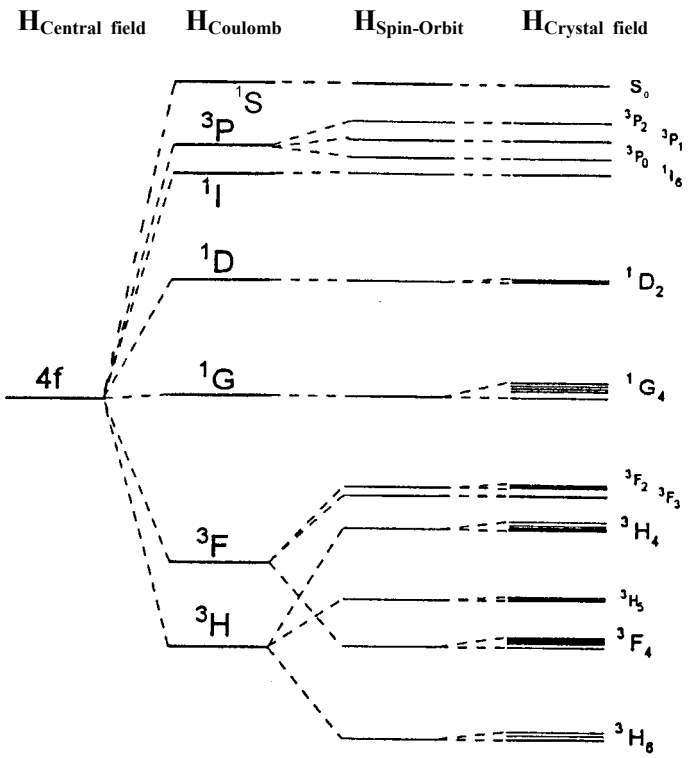

Term	$4f^n$	^{2S+1}L	$^{2S+1}L_J$	Γ_i
Degeneracy	$\binom{14}{12} = 91$	(2L+1)(2S+1)	(2J+1)	Depends on crystal field symmetry
Energy splitting	~10^4-10^5 cm^{-1}	~10^3-10^4 cm^{-1}	~10^3-10^4 cm^{-1}	~10^2-10^3 cm^{-1}

Fig. 1-4: *Energy splitting of Tm^{3+}:YAG ($4f^{12}$) [Gru89].*

The state wavefunctions in the intermediate coupling scheme are most clearly distinguished by using group theory or rather irreducible representations of the group constructed by using tensor operators as shown by Racah [Rac42]. For a detailed study of the classification of f^n configurations (using group theory) see also Judd [Jud63] and Wybourne [Wyb65]. After Kramer's rule, the number of Stark levels is doubly degenerated for an odd number of electrons, rescinded in the presence of a magnetic field.

1.2.2 Radiative Transitions

In this section the most important formulas used to calculate the radiative transition probabilities will mainly be stated. For a detailed study on the theoretical aspects given in this section the following references should be cited: Carnall&Crosswhite [Car77],

Condon&Shortley [Con70], Fano&Racah [Fan59], Goerller-Walrand&Binnemans [Goe98], Judd [Jud62], Kaminskii [Kam96], Krupke ([Kru65], [Kru66], [Kru71], [Kru74]), Ofelt [Ofe62], Weber [Web67], and Wybourne [Wyb65].

1.2.2.1 Transition Probabilities from Absorption Spectra (Judd-Ofelt Theory)

Radiative transitions [Hen89] between electronic states of rare earth ions in crystals are predominantly of electric- and magnetic-dipole character. Their transition rates are proportional to the squared dipole operator matrix elements [Kam96]. Magnetic-dipole transitions within a configuration (intraconfigurational transitions such as 4f-4f) are allowed, but ~ 10^5 less probable than electric-dipole transitions [Sve89]. According to the Laporte selection rule intraconfigurational electric-dipole transitions are parity forbidden [Goe98]. Acentric perturbations can permit these transitions e.g. by admixing electronic states of opposite parity (of which the nearest is the $4f^{n-1}5d$ configuration). These forced transitions are the so called *induced* electric dipole transitions. The selection rules of magnetic-dipole and induced electric-dipole transitions as displayed in Table 1-1 are further described in the literature ([Kam90], [Goe98]). The in section 3.2 discussed hypersensitive transitions obey the selection rules of quadrupole transitions ($|\Delta S|=0$, $|\Delta L|\leq 2$, $|\Delta J|\leq 2$), but are several orders of magnitude too large for the weak quadrupole transitions and therefore, are considered pseudo-quadrupole transitions. Hypersensitive transitions are further described at the end of this section.

Table 1-1. *Selection rules of magnetic dipole and induced electric dipole transitions.*

Induced electric dipole transitions (ED)	*Comment*
$\Delta l=\pm 1$; $\Delta S=0$; $\|\Delta L\|\leq 2l=6$; $\|\Delta J\|\leq 2l=6$, $\|\Delta J\|=2,4,6$ if $J=0$ or $J'=0$	Spin-orbit interactions can lead to violation of the S and L selection rules, but the J rule will hold as long as J remains a "good" quantum number meaning as long as there is no J-mixing.
Magnetic dipole transitions (MD)	
$\Delta l=0$; $\Delta S=\Delta L=0$; $\Delta J=0, \pm 1$, but $0\leftrightarrow 0$ is forbidden	

The theory derived by Judd [Jud62] and independently by Ofelt [Ofe62] allows the calculation of the transition probabilities between electronic levels and is of importance for the interpretation and calculation of the intensities of optical spectra for rare earth ions in e.g. crystalline materials. In the Judd-Ofelt model, a single average energy is ascribed to all states of the perturbing opposite-parity configuration which simplifies the calculation of the dipole matrix element and thus, also the calculation of the transition rates.

A few of the assumptions made in the context of this simplification are stated in the following: The energetic distance of the perturbing opposite-parity states and the $4f^n$ states is assumed to be large, which is usually a valid approximation for the majority of the trivalent lanthanide ions as shown in Appendix A (Fig. A-2). The splitting within multiplets of the excited configurations is assumed to be negligible compared to the energetic distance that the excited configurations as a whole lie above $4f^n$ [Jud62]. As Krupke [Kru65] wrote "each excited orbital is completely degenerate in S, L, and J, but each is separated in energy from the $4f^n$ configuration by an amount characteristic of that particular orbital".

In the context of the theoretical treatments a small number of phenomenological host-dependent intensity parameter are introduced which contain implicitly the radial parts of the $4f^n$ wavefunctions, the wavefunctions of perturbing configurations, and odd-symmetry crystal-field terms which characterize the environment of the ion. These Judd-Ofelt intensity parameters of the particular ion-host system are commonly determined empirically from a best fit of calculated and measured line strengths of selected transitions and can, in turn, be used to calculate radiative transition probabilities between any two J manifolds as can be seen further below.

According to the Judd-Ofelt model, the line strength of an induced electric dipole (ED) transition between an initial J manifold $|4f^n\gamma[SL]J\rangle$[3] and terminal J` manifold $|4f^n\gamma[S`L`]J`\rangle$ is expressed by the sum of the squared reduced matrix elements of tensor operators $U^{(t)}$ of rank t calculated in the intermediate coupling approximation and the Judd-Ofelt intensity parameters Ω_t (t=2,4,6) as follows:

$$S^{ED} = \sum_{t=2,4,6} \Omega_t \left| \left\langle 4f^n \gamma[SL]J \right\| U^{(t)} \left\| 4f^n \gamma[S'L']J' \right\rangle \right|^2 \qquad (1\text{-}2)$$

[3] The with square brackets enclosed quantum numbers shell indicate that these are useful in classifying states, but that they are in themselves not exact quantum numbers. The γ is used for additional quantum numbers not presented in detail. The wavefunctions used to describe the levels of the $4f^n$ configuration in the intermediate coupling scheme are written as a linear combination of wavefunctions of the LS-basis set by using intermediate coupling coefficients as commonly described in the literature ([Kru65], [Web67], [Kam90]).

The squared reduced matrix elements $<||U^{(t)}||>$ vary only slightly from host to host for a given RE^{3+} ion and therefore, are considered to be unchanged. They describe the deviation of the states of the particular ion with respect to a certain mixture in the crystal field. In this study the reduced matrix elements were taken from Kaminskii [Kam96].[4] All reduced matrix elements of U(t) for t>6 become zero between f-electron states and therefore, the line strengths depend only on three parameters Ω_t (t=2,4,6). As Krupke [Kru74] wrote, the description of the line strength in terms of only three parameters is due to averaging dipole moments over the crystal-field split Stark components and the assumption that all the Stark levels of the initial J-manifold are equally populated. The latter one - although at 300 K usually not achieved – remains valid for ions in sites of low symmetry coordination [Kru71].

The integrated absorption cross section of a transition within the $4f^n$ configuration is related to the signal strengths S^{ED} of induced electric dipole transition and S^{MD} of magnetic dipole transitions (MD) as follows:

$$\int \sigma \frac{d\lambda}{\lambda} = \frac{4\pi^2 e^2}{3\hbar c} \cdot \frac{1}{2J+1} \left[\frac{(n^2+2)^2}{9n} S^{ED} + nS^{MD} \right] \qquad (1\text{-}3)$$

where σ is the absorption cross section at wavelength λ, 2J+1 is the degeneracy of the initial level (here, the ground state), and n the refractive index. The factors $(n^2+2)^2/9n$ and n account for the local-field and dielectric environment for electric and magnetic dipole transitions, respectively.

The degeneracy factor (2J+1) implicitly contains the assumption stated above that all levels of the initial J multiplet are equally occupied or that transitions from all crystal field levels of the multiplet are equally probable which makes the Judd-Ofelt theory for example in most cases invalid at low temperature. For one of the here investigated dopant ions such as Europium it is still applicable since the ground state $^7F_0$ is non-degenerate. Note also, that in the case of Europium the ground state level $^7F_0$ and the first excited state level $^7F_1$ are closely spaced in energy (Fig. 1-2) and therefore, both states are populated at room temperature. The non-negligible thermal population of ~ 36% for the $^7F_1$ state necessitate the introduction of the fractional thermal population factor $X_a(T)$ (Appendix B) in the calculation of the Judd-Ofelt intensity parameter for Eu:KPB (section 3.2.3).

By subtracting the line strengths S^{MD} of magnetic dipole transitions (as given further below) from the integrated absorption cross section the line strengths of induced electric dipole

[4] The squared reduced matrix elements calculated in the intermediate coupling scheme can be determined with the reduced matrix elements tabulated in Nielsen&Koster [Nie64] and the 6-j symbols [Rot59] as described in e.g. [Web67] or [Kam96].

transitions S^{ED} can be extracted through measured absorption spectra by eqn. 1-3 in addition to the calculated line strengths given by eqn. 1-2. Thus, the Judd-Ofelt intensity parameters can be found by solving the set of equations that give the best least-square fit of the calculated to the measured line strengths as described in the literature ([Kru71], [Goe98]). Note, that the matrix elements in eqn. 1-2 simply have been added if some of the absorption bands studied (section 3) consisted of two or more transitions. Another advantage of the additivity of the Judd-Ofelt intensity parameters in eqn. 1-2 is that in the presence of non-equivalent host lattice sites - where the rare earth ion is incorporated - an average value of each of the Ω_t parameters is obtained, which makes the parameterization valid for even highly disordered systems such as glass. Note, that in the case of birefringent crystals the polarization dependency leads to the calculation of the Judd-Ofelt intensity parameter by measuring the absorption in each polarization and by suitable averaging the σ– and π- polarized components provided the orientation is known.

The signal strength of magnetic dipole (MD) transitions is given by

$$S^{MD} = (\hbar / 2mc)^2 \left| \left\langle 4f^n \gamma[SL] J \right\| \vec{L} + 2\vec{S} \left\| 4f^n \gamma[S'L'] J' \right\rangle \right|^2 \qquad (1\text{-}4)$$

As mentioned earlier, the enclosement in square brackets [SL] indicates the computation in the intermediate coupling scheme. The line strengths S^{MD} were calculated by using the formulas of references as noted in the individual sections of chapter 3. For a general description of the calculation of S^{MD}, in particular the transformation from the LS coupling scheme into the intermediate coupling scheme, see Nostrand [Nos00b], Carnall *et al.* [Car77], and Weber [Web67].

Once S^{ED} and S^{MD} are determined by eqn. 1-2 and 1-4, respectively, the calculation of the transition probabilities is straightforward. The radiative transition rate for spontaneous emission of dipole radiation between two levels J and J` is given by:

$$A_{JJ'} = \frac{32\pi^3 e^2}{3\hbar c} \cdot \frac{c}{\lambda^3 (2J+1)} \left[\frac{n(n^2+2)^2}{9} S^{ED} + n^3 S^{MD} \right] \qquad (1\text{-}5)$$

where the local field corrections for the rare earth ion in the initial J manifold are $n(n^2+2)^2/9$ and n^3 for electric dipole (ED) and magnetic dipole (MD) transitions, respectively.

The total transition rate from a given J level is given by the summation of the individual rates (summed over all terminal levels J') and is related to the radiative lifetime of level J by:

$$A_J = \sum_{J'} A_{JJ'} = \frac{1}{\tau_J^{rad}} \qquad (1\text{-}6)$$

Once the radiative rates are calculated the radiative branching ratios can easily be obtained by:

$$\beta_{JJ'}^{rad} = \frac{A_{JJ'}}{A_J} = A_{JJ'} \cdot \tau_J^{rad} \tag{1-7}$$

The radiative quantum efficiency of level J can be determined by using:

$$\eta_{J,eff}^{rad} = \frac{\tau_J^{meas}}{\tau_J^{rad}} \ , \tag{1-8}$$

where τ_J^{meas} is the measured lifetime of level J which is reciprocal to the sum of the nonradiative and radiative rates as displayed in section 1.2.3. The Judd-Ofelt calculation of the transition probabilities as shown above is for several investigated ion-host systems a successful approach. Appearing errors adequately reflect e.g. experimental uncertainties.

Hypersensitive transitions are pseudo-quadrupole transitions which are very sensitive to the environment of the lanthanide ion. While usually the intensity of the induced electric dipole transition in lanthanide ions does not vary much in different host matrices, the intensity of hypersensitive transitions can increase e.g. a factor of 200 by going from a complexed lanthanide ion to a lanthanide ion in aqueous solution [Goe98]. Hypersensitivity was associated by Judd [Jud62] with large $U^{(2)}$ reduced matrix elements and described by the absolute magnitude of the Ω_2 parameter if the $U^{(4)}$ and $U^{(6)}$ reduced matrix elements for the particular transition are small. Sometimes, not the absolute magnitude of the Ω_2 parameter is considered, but the relative magnitude of the Ω_2 parameter with respect to Ω_4 and Ω_6 as a measure for the hypersensitive nature of a transition [Hen74]. An example for a hypersensitive transition is the $^4I_{9/2} \rightarrow {}^4G_{5/2}$ transition in Nd^{3+} (which overlaps in energy with the $^4I_{9/2} \rightarrow {}^2G_{7/2}$ transition). Here, $U^{(2)} = 0.8979 > U^{(4)} = 0.4093 >> U^{(6)} = 0.0359$. As can be seen, $U^{(2)}$ is large, but especially the $U^{(4)}$ parameter is in this case also non-negligible. Hypersensitivity is believed to be related to the crystal structure or rather coordination polyhedron (coordination number and site-symmetry) around the rare earth ion, and therefore, the Ω_2 parameter can significantly vary from host to host. Ω_2 can be seen as a measure of the dipolar component.

Note, that radiative transitions such as excited state absorption and reabsorption which can occur in addition to the elementary processes (ground state absorption, spontaneous emission and stimulated emission [Hen89]) will be described in the context of the measurements and data evaluation (section 2.2.6).

1.2.2.2 Transition Probabilities from Emission Spectra

The use of emission spectra is another possibility to calculate radiative transition probabilities such as branching ratios and quantum efficiencies.
Emission cross sections have been determined by using the Fuechtbauer-Ladenburg equation [Aul82]:

$$\sigma_{JJ'}^{em}(\lambda) = \frac{\lambda^5 \beta_{JJ'}^{rad,meas} I(\lambda)}{8\pi c n^2 \tau_J^{rad} \int_{J\to J'} I(\lambda)\lambda d\lambda} \tag{1-9}$$

where I(λ) is the blackbody calibrated emission intensity, τ_J^{rad} the radiative lifetime (by Judd-Ofelt), n and λ the refractive index and wavelength, and $\beta_{JJ'}^{rad,meas}$ the radiative branching ratio. In this case the radiative branching ratios are calculated by using:

$$\beta_{JJ'}^{rad,meas} = \frac{\int_{J\to J'} I(\lambda)\lambda d\lambda}{\sum_{J'} \int_{J\to J'} I(\lambda)\lambda d\lambda} \tag{1-10}$$

A comparison of the measured (this section) and calculated (previous section) branching ratios will be given in section 3.2.1.2 for Nd:MPB (M=Rb, K). Calculations of the radiative quantum efficiency from the measured emission spectrum done specifically for the $^4F_{5/2}+^2H_{9/2}$ level will also be described in that particular section. Generally, the comparison of the measured and calculated transition probabilities can be seen as an approach to test the validity of the results.

1.2.3 Nonradiative Decay: Multiphonon Relaxation and Other Quenching Mechanisms

In addition to radiative transitions between energy levels of rare earth ions, nonradiative relaxation processes can also occur as mentioned in section 1.1. The most common sources of nonradiative decay for excited rare earth ions in crystals are (multi)phonon emission to lower levels, and, at sufficiently high concentrations, e.g. (phonon assisted) energy-transfer and energy-migration also to other quenching centers (Fig. 1-5).
The transition from an energy level E_2 to an energy level E_1 by emitting $p=E_2-E_1/\hbar\omega_{eff}$ phonons is called multiphonon relaxation (Fig. 1-5(a)). It is an intraionic process while energy migration as well as energy transfer processes such as energy transfer upconversion (ETU) and cross-relaxation are interionic processes (Fig. 1-5(b)-(d)).

In the case of ETU and cross relaxation the excited donor D* such as the rare earth ion transfers the energy to the acceptor A which can be either a neighboring (rare earth) ion, an impurity or defect. For the pump intensity dependent ETU process donor and acceptor ion are

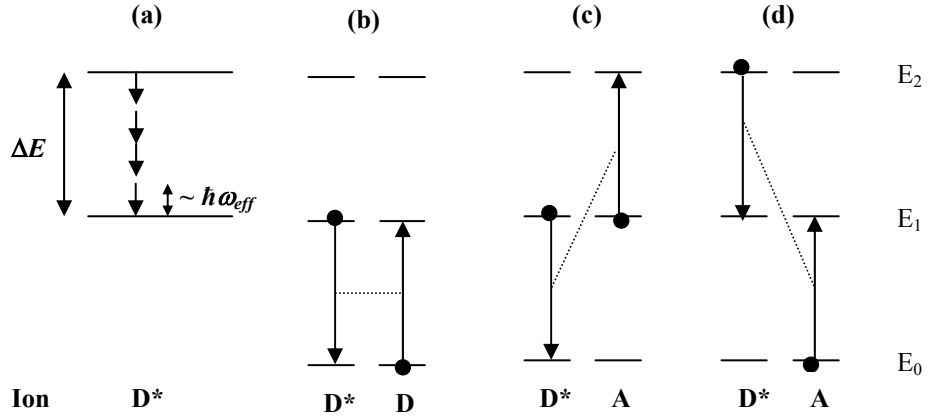

Fig. 1-5. *Intraionic (a) and interionic ((b)-(d)) nonradiative decay mechanisms: Multiphonon emission (a) and concentration dependent energy migration (b) as well as energy transfer such as energy transfer upconversion (c) and cross relaxation (d).*

initially in an excited state (Fig. 1-5(c)). It is usually called Auger upconversion [Pay92] if two ions result from the same level. The donor transfers the energy to the acceptor by going into a lower state of energy while the acceptor is of higher energy than initially, and therefore, lasing at shorter wavelength than the pump wavelength can be realized. In the case of cross relaxation the donor is initially in a state of higher energy than the donor and acceptor after the energy transfer occured (Fig. 1-5(d)). In both processes the energy gaps of the participating donor and acceptor transitions are resonant. Phonon assisted energy transfer can occur in order to bridge non-equivalent energy gaps. Cross relaxation can be a feasible process to depopulate the lower laser level of an active ion e.g. by the use of codopants with high absorption cross sections in the energy range of interest. Energy-migration (Fig. 1-5(b)) can accelerate these two energy transfer processes since the excitation of a donor ion migrates with high velocity between ions of the same type through a wide area of the host material. This can also result in enhanced energy transfer to impurities and defects which leads to lifetime shortening and possibly to high losses for anticipated laser operation. Usually, the Foerster&Dexter static transfer model ([Foe48], [Dex53]) and Burshtein`s hopping model ([Bur72], [Bur85]) are used to calculate the (migration assisted) energy transfer rates provided that parameters such as the overlap integrals, ion concentration etc. are known ([Cai91], [Pay92]).

The total transition rate W_J from a given energy level J is given by the sum of the radiative A_J^{rad} and nonradiative rate W_J^{nr}:

$$W_J = A_J^{rad} + W_J^{nr} \tag{1-11}$$

with

$$W_J^{nr} = W_J^{MP} + W_J^{c} \tag{1-12}$$

where the radiative rate A_J^{rad} and the multiphonon decay rate W_J^{MP} are not concentration dependent while the W_J^c term stands mainly for quenching caused by energy transfer and/or energy migration which is partly mediated by the RE^{3+} concentration (e.g. via the migration-enhanced energy-transfer mechanism [Hen89]). I. e. the transition probability increases with smaller distance of donor and e.g. acceptor [Foe48] and therefore, these processes become most important at higher dopant concentration.
The rates are dependent on temperature as shown further below for the multiphonon decay rate which will be further discussed for the case of Tb^{3+} in the host crystal KPB (section 3.3).

(Multi)phonon emission can happen very fast for levels with small energy gaps compared with the highest energy phonons, so that fluorescence is normally not observed. A phenomenological expression to describe multiphonon decay in a weak coupling ion-lattice interaction case is the so called "energy gap law" ([Lay77], [Kam96]). Here, the multiphonon decay rate W^{MP} from a given level is estimated by:

$$W^{MP} = C\exp(-\chi\Delta E)[1-\exp(-\hbar\omega_{eff}/kT)]^{-p} \tag{1-13}$$

where ΔE is the energy gap to the next lowest level, $\hbar\omega_{eff}$ the effective phonon energy, $p = \Delta E/\hbar\omega_{eff}$ is the "effective order" or the number of phonons involved in the process, and C and χ are host dependent phenomenological constants as calculated for KPB in section 3.2.4 and 3.3.1. Note, that the temperature dependency of the multiphonon decay rate arises from the treatement of phonons after the Bose-Einstein distribution. The Bose-Einstein occupation number for a given frequency of phonons is given by:

$$n(T) = [\exp(\hbar\omega_{eff}/kT) - 1]^{-1}, \tag{1-14}$$

so that the energy gap law can be expressed as:

$$W^{MP} = C\exp(-\chi\Delta E)[n(T)+1)]^{p} \tag{1-15}$$

Here, the 1 in the bracket indicates the spontaneous emission of phonons while the n(T) indicates the stimulated emission of phonons. For T→0 only spontaneous emission occurs and the energy gap law turns into:

$$W_{T=0}^{MP} = C\exp(-\chi\Delta E)\,. \tag{1-16}$$

From the fit to measured data the multiphonon relaxation was observed to occur by emitting the smallest number of phonons consistent with the energy gap and the highest frequency lattice vibrations (e.g. determined from the Raman scattering spectra or IR-cutoff, section 3.1).

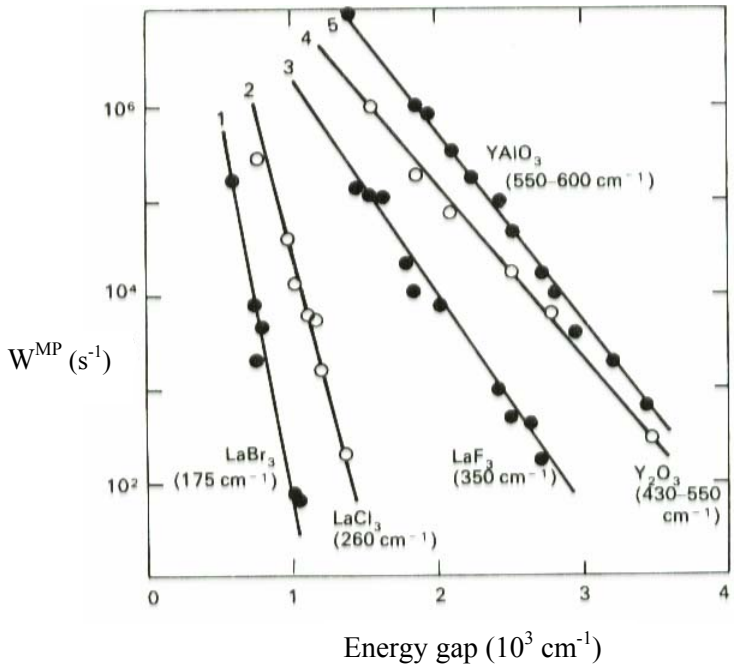

Fig. 1-6. *Decay rate of spontaneous multiphonon emission versus energy gap to the next lowest level for five different host crystals of different phonon energy [Hen89]. The measured points (circle) were determined by subtracting the calculated radiative rate (Judd-Ofelt) from the measured decay rates $1/\tau^{meas}$ for a number of excited states. The plotted lines through the measured points clearly indicate the exponential dependence on the energy gap.*

Figure 1-6 shows the spontaneous multiphonon transition rate versus energy gap to the next lowest level for five different host crystals of different phonon energy. The measured points (circle) were determined by subtracting the calculated radiative rate (Judd-Ofelt) from the measured decay rates $1/\tau^{meas}$. By fitting the data points with the energ gap law, the host dependent phenomenological constants C and χ can be found. The plotted lines (semilogarithmic) through the measured points clearly indicate the exponential dependence on the energy gap across which the decay takes place, independent on the electronic state or rare earth ion. The validity of the exponential dependency of the multiphonon decay rate on energy gap, its temperature dependency etc. has been proven by studies of various rare earth-doped crystalline and glassy host materials ([Par67], [Ris67], [Ris68], [Web67], [Web68] [Web72], [Web73], [Ree73], [Lay75], [Lay77], [Bib95], [Nos01], [Orl02], [Qui03] and many more).

The experimentally determined exponential dependency of the multiphonon decay rate or rather the energy gap law can also be derived theoretically using high order perturbation theory. Here, assumptions like

- the Born-Oppenheimer approximation (separation of electronic and lattice wavefunction in the total wavefunction [Bor27])
- the harmonic oscillator [Hen89] approximation to describe the phonon states,
- weak ion-lattice coupling,

etc. were made. For comprehension the author refers in particular to Layne ([Lay75], [Lay77]), Kiel ([Kie62], [Kie63]), and Riseberg&Moos [Ris68]. There, the interaction of an isolated rare earth ion with its dynamic crystalline field is ascribed to be due to the modulation of the crystalline field by the lattice vibrations. If each ion is assumed to behave as a point charge, this impact can be seen as an displacement of the ions from their equilibrium position, where the crystal field Hamiltonian can be expanded in a Taylor series about this equilibrium position. The interaction Hamiltonian H_{int} can be written as a sum of the static and dynamic crystal field components as follows:

$$H_{\text{int}} = V_{CF} + \sum_i V_i Q_i + \frac{1}{2}\sum_{i,j} V_{ij} Q_i Q_j + \ldots \tag{1-17}$$

Here, the static component V_{CF} contains the free ion Hamiltonian and the effects of the time averaged crystal field, giving the energy level splitting (section 1.2.1). The remaining terms, which involve the normal coordinates Q_i, represent the interaction components with the vibrating lattice. The coefficients V_i, V_{ij} etc. stand for the partial derivatives of the crystal field with respect to the normal modes

$$V_i = \frac{\partial V_{CF}}{\partial Q_i}, \quad V_{ij} = \frac{\partial^2 V_{CF}}{\partial Q_i \partial Q_j}, \quad \ldots. \tag{1-18}$$

So, the different order terms in eqn. 1-17 can be seen as being split: While $V_{i,}$ V_{ij} describes the electronic part of the perturbation operator [Lay75], producing the ionic transitions, Q_i stands for the normal mode of the surrounding complex, which produces the lattice-phonon transitions [Kie63]. In a crystal, the normal coordinates are simplified by using coordinates which have the symmetry of the ion site, and therefore, they could refer to normal modes of vibration of the unit cell centered around the ion [Lay75]. From the quantum mechanical description of a harmonic oscillator those normal coordinates are expressed by the creation and annihiliation operators [Sch88].

The emission of many phonons can be described by the first order term in the expansion (second term in eqn. 1-17) using higher order of perturbation theory as considered by Kiel [Kie63] and Layne [Lay75]. Alternatively, multiphonon emission can arise from a higher order term in the expansion (eqn. 1-17) taken in low order perturbation theory. The following expression of the transition rate from an initial atomic state to a final state $|\psi_a\rangle \rightarrow |\psi_b\rangle$ with the emission of p phonons, includes both mechanisms [Ris68]:

$$\begin{aligned} W_{(p)} = \frac{2\pi}{\hbar} \cdot \sum_{i\cdots j, m_1 \cdots m_{p-1}} & \left|\left\langle n_i + 1 \middle| Q_i \middle| n_i \right\rangle\right|^2 \cdots \left|\left\langle n_j + 1 \middle| Q_j \middle| n_j \right\rangle\right|^2 \\ & \times \frac{\left|\left\langle \psi_b \middle| V_i \middle| \psi_{m_{p-1}} \right\rangle\right|^2 \cdots \left|\left\langle \psi_{m_1} \middle| V_j \middle| \psi_a \right\rangle\right|^2}{(E_{m_{p-1}} + \hbar\omega_j + \cdots + \hbar\omega_{i-1} - E_a)^2 \cdots (E_{m1} + \hbar\omega_j - E_a)^2} \\ & \times g(\omega_i) \cdots g(\omega_j) \delta(E_b + (\hbar\omega_i + \cdots + \hbar\omega_j) - E_a) \\ + \frac{2\pi}{\hbar} \cdot \sum_{i\cdots j} (1/p!)^2 & \left|\left\langle \psi_b \middle| V_{i\cdots j} \middle| \psi_a \right\rangle\right|^2 \left|\left\langle n_i + 1 \middle| Q_i \middle| n_i \right\rangle\right|^2 \cdots \left|\left\langle n_j + 1 \middle| Q_j \middle| n_j \right\rangle\right|^2 \\ & \times g(\omega_i) \cdots g(\omega_j) \delta(E_b + (\hbar\omega_i + \cdots + \hbar\omega_j) - E_a) \end{aligned} \qquad (1\text{-}19)$$

Here, beside the energy conserving δ function, $n_i \cdots n_j$ are phonon occupation numbers, $|\psi_{m1}\rangle \cdots |\psi_{mp-1}\rangle$ are intermediate virtual states, and $g(\omega_i) \cdots g(\omega_j)$ are the densities of phonon states. Obviously, the calculation of the transition rate after eqn. 1-19 is very complex since e.g. all the intermediate states would have to be known, which makes it quite intractable. Layne ([Lay75], [Lay77]) expressed the ratio ε of the rates of a p phonon process to a p-1 order phonon process as:

$$\frac{W_{(p)}}{W_{(p-1)}} = \varepsilon = \frac{\hbar}{2M\omega_{eff}} 4m^2 \frac{\left|\left\langle \psi_a \middle| \overline{V}_{CF}^{''} \middle| \psi_b \right\rangle\right|^2}{(\hbar\omega_{eff})^2} [n(T)+1] = \varepsilon'[n(T)+1], \qquad (1\text{-}20)$$

where M is a mass-related coefficient, m the number of phonon modes, $n(T)$ and $\hbar\omega_{eff}$ the effective phonon occupation number and energy (assumption that phonons of ~ equal energy are involved in the transition), and $\left|\left\langle \psi_a \middle| \overline{V}_{CF}^{''} \middle| \psi_b \right\rangle\right|$ an averaged matrix element, by assuming that it is the same for a p and p-1 order process and different initial and final states. An averaged matrix element $\left|\left\langle \psi_a \middle| \overline{V}_{CF}^{''} \middle| \psi_b \right\rangle\right|$ in this expression arises from the assumption that precise features of modes and levels are statistically-averaged out for high order processes, which is likely so because of the large number of interacting phonon modes and intermediate states [Ris68]. Usually, the highest energy phonon is used for the effective phonon energy $\hbar\omega_{eff}$.

If the perturbing potential is small, which is a condition in order for the perturbation theory above to apply [Lay75], the transition rate for a pth order process should be smaller than for a p-1 order process [Kie63]:

$$\frac{W_{(p)}}{W_{(p-1)}} = \varepsilon << 1. \tag{1-21}$$

Kiel [Kie63] found also that the coupling constant ε can be as large as ~ 0.05 (or somewhat greater). ε is independent of p and can physically be seen as the amplitude of the vibration divided by the energy of the vibration [Lay75]. The following extension by Riseberg and Moss [Ris68] has been made in order to show the transition rate as an exponential function of the energy gap:

$$\begin{aligned} W_{(p)} &= W_{(p-1)} \cdot \varepsilon \\ W_{(p)} &= W_{(p-2)} \cdot \varepsilon^2 \\ \vdots \qquad &\qquad \vdots \\ W_{(p)} &= W_{(0)} \cdot \varepsilon^p \end{aligned}, \tag{1-22}$$

This way the exponential dependency of the nonradiative (multiphonon) decay rate is deduced as:

$$W_{(p)} = C \cdot \exp(p \ln(\varepsilon)) = C \cdot \exp(\ln(\varepsilon) \cdot \frac{\Delta E}{\hbar \omega_{eff}}) \tag{1-23}$$

with $p=\Delta E/\hbar\omega_{eff}$. The nonradiative multiphonon decay rate decreases with lower phonon energy and higher energy gap which also means it decreases with effective order p. Stronger electron-phonon coupling yields to faster multiphonon decay rates. The temperature dependency can be made more conceivable by using $\varepsilon = \varepsilon'[n(T)+1]$ from eqn. 1-20:

$$W^{MP} = W_{(p)} = C \cdot \exp(p \ln(\varepsilon'))[n(T)+1]^p = C \cdot \exp(-\chi \Delta E) \cdot [n(T)+1]^p \tag{1-24}$$

with $\chi=\ln(1/\varepsilon')/\hbar\omega_{eff}$. This way the experimental determined energy gap law is deduced (eqn. 1-15). From the fit to the experimental results it was shown that only the highest energy vibrations $\hbar\omega_{eff}$ from the phonon spectrum are important, which is implied through the dependence on p in the energy gap law (minimizing of the order of the process). The number of phonons p involved can usually be determined by a plot of W^{MP} against temperature since this temperature dependency is quite distinct for different p as can be seen exemplary in Orlovskii *et al.* [Orl02].

So, from the studies made it was concluded that the multiphonon decay involves high energy phonons and occurs in the lowest order possible consistent with energy conservation and the cutoff in the phonon spectrum [Ree73]. While the radiative rate experiences a decrease with longer wavelength ($A^{rad} \sim 1/\lambda^3$, previous section), the nonradiative rate increases near exponentially with decreasing energy gap; this leads to lower quantum efficiency towards longer wavelengths ($\eta^{rad}_{eff} = A^{rad}/(W^{nr}+A^{rad})$). The nonradiative decay rate depends both on the energy gap to the next lowest level as well as on the phonon energy, while the lattice vibrations seem to have a small effect on the radiative rate. Therefore, the choice of a suitable host with low-phonon energy can result in higher quantum efficiency for the particular transition meaning that nonradiative (multiphonon) decay competes less effectively with the radiative decay which increases the possibility of e.g. LWIR lasing. Additionally, the decrease of the vibrational energy along the halide series F-Cl-Br-I due to the increasing mass of the vibrating constituents (eqn. 1-1) can open up new pathways for e.g. upconversion processes in chlorides, bromides and iodides, since electronic states which are immediately depleted in oxides and fluorides become metastable in these materials due to the reduced efficiency of multiphonon relaxation processes. An interesting study related to the investigation of new upconversion processes along the series Cl-Br-I is given by Guedel *et al.* [Gue00] and Hehlen *et al.* [Heh94].

2. Preparation and Experimental Methods

2.1 Preparation of RE^{3+}-Doped KPb_2Br_5 and $RbPb_2Br_5$ Crystals

This section describes collaborative efforts (especially in the area of crystal growth), and the author would like to refer on the following collaborators and their colleagues: Prof. Arnold Burger (Center for Photonic Materials and Devices, Department of Physics, Fisk University, TN, USA), Prof. Ludmila I. Isaenko and Dr. Alexander P. Yelissejev (Design and Technological Institute for Monocrystals (DTIM), Novosibirsk, Russia), Dr. Krishna C. Mandal (EIC Laboratories, Inc., MS, USA), and Dr. Karel Nitsch (Institute of Physics, Academy of Sciences of the Czech Republic, Prague, Czech Republic).

2.1.1 Crystal Growth: Procedure and Results

Single crystals of KPb_2Br_5 and $RbPb_2Br_5$ doped with Nd^{3+}, Tb^{3+}, and Eu^{3+} were grown by the Bridgman technique ([Lau70],[Bri86]) from a stoichiometric and congruent melting composition [Col71] at 382°C, as illustrated for KPb_2Br_5 in Figure 2-1. At Fisk University and DTIM a phase transition in KPb_2Br_5 is observed at a temperature of 256°C and 246°C, respectively, which matches the value of 242°C reported in the literature ([Col71], [Nit96]). In $RbPb_2Br_5$ a phase transition was described at 267°C ([Col71]).

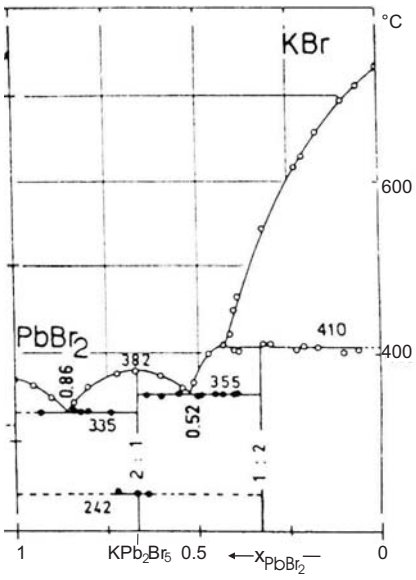

Fig. 2-1. *Phase diagram of KPb_2Br_5 [Col71].*

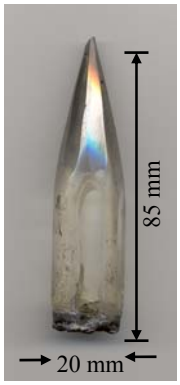

Fig. 2-2. *Undoped KPb_2Br_5 crystal grown by the Bridgman technique.*

The Nd^{3+}-doped bromide crystals were mainly grown at DTIM. Initial components taken as bromides were purified using directed crystallization. Oxidic compounds like lead hydroxide bromide Pb(OH)Br and lead oxide bromide $PbBr_2$*PbO are formed easily during heating of $PbBr_2$ with traces of moisture [Nit93], which can be present in lead bromide. Therefore, the latter was purified under Br_2+HBr gaseous mixture. The doping component, $NdBr_3$, was prepared by distillation. The (rare earth-doped) KPb_2Br_5 (Fig. 2-2) and $RbPb_2Br_5$ crystals were grown in evacuated silica ampoules in a double-zone furnace, providing a temperature gradient

of ~ 20°C/cm. The translation velocity was 1mm/day-1mm/hr. The investigated RE^{3+}:KPb_2Cl_5 crystals (section 3) were grown by a similar procedure [Nos00b].

The single crystalline Tb^{3+}- and Eu^{3+}-doped KPB samples were mainly grown at Fisk University and at EIC Laboratories, Inc. by the Bridgman technique. At Fisk University, KPB was synthesized from a stoichiometric mixture under high purity Ar with 310 mbar over atmospheric pressure. The synthesized material was then zone refined [Pfa52] in an evacuated ampoule for several passes. About 8-9 mm of the last to freeze portion was completely black and unusable. Possibly the decomposition products of $PbBr_2$ were segregated towards the last-to-freeze portion of the zone refined ingot. Temperature gradients were about 5 - 10 °C/cm and a translation speed of ~ 6-6.5 mm/day was used. At EIC Laboratories, Inc. crystals were synthesized and grown in evacuated quartz ampoules backfilled with argon overpressure or bromine overpressure to prevent out-diffusion of Br_2 and to maintain the stoichometric growth conditions avoiding any defect formation during crystal growth as well as to reduce the water content. The investigated crystals were grown in a three zone vertical Bridgman furnace at 1 mm/hr translation speed of the ampoule. The temperature gradients were approximately 12 °C/cm. The crystals were typically 60 mm long and 10 mm in diameter.

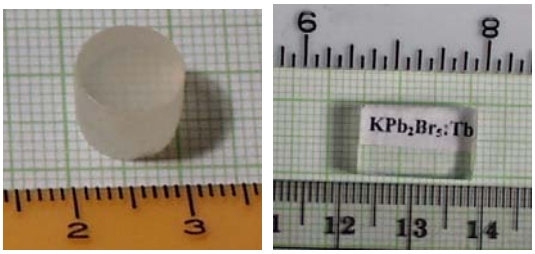

Fig. 2-3. *KPb_2Br_5:Tb crystals cut from grown ingot: (left) a polished cylindrical crystal (10 mm diameter and 7.8 mm long) and (right) a polished wafer grown under Br_2 - overpressure (1.6x0.9x0.45 cm^3).*

The grown crystals are moisture-resistant. The polished samples are ~ 2-10 mm in path lengths and typically colorless as shown for illustration in Fig. 2-3. Some of the Nd^{3+}-doped samples turned out to be violet-bluish due to a higher dopant content, while some of the Br_2-overpressure grown Tb^{3+}-doped samples are of yellow coloring and appear to be more susceptible to cracking. The Eu^{3+}-doped KPB samples are dark brown, which one could assume to be due to 4f-5d (Eu^{2+}) [Kob80], charge transfer transitions [Dem02] etc. Europium is likely to appear in the divalent state due to the reduced reduction potential for $Eu^{3+} \rightarrow Eu^{2+}$ (0.35 V) compared with other RE^{3+} ions ([Wic99], [Car79]); however, the presence of Eu^{2+} causes usually yellowish coloring due to its absorption bands [Kob80], as can be seen for an Europium-doped KPC crystal in Voda et al. [Vod04]. Charge transfer transitions were found at ~ 410 nm in Eu^{3+}:$CsCdBr_3$ [Dem02]. Thus, further investigations are needed to fully determine the dark brown crystal color. The segregation coefficient for the grown crystals was determined at EIC and DTIM to be approximately ~ 0.8 or even higher.

Structural imperfections like e.g. mosaic structure/low-angle grain boundaries [Lau70] and growth striae like in Nd:GGG [Bel73] are observed as shown by microscopic pictures (Fig. 2-4).[5] Their occurrence can be due to the observed phase transitions (mosaic structure), the use of dopant ions (growth striae), growth conditions etc. By measuring the Nd concentration at different crystal positions (over a range of 100 μm) via microprobe analysis (section 2.1.2) variations from 0.03 to 0.11 weight percent neodymium were found in a Nd:KPB crystal. Further studies are needed to determine if there are very high Nd concentrations accumulated in certain regions of observed structural imperfections, which could increase processes such as migration enhanced energy-transfer mechanisms (section 1.2.3 and 3.2.2.3). The refractive index measured at different positions of a Nd:KPB sample (orientation not known) by the ellipsometry technique [Ben78] varies from n = 1.99 to 2.1, but this is probably more due to the birefringence of the crystal (next section).

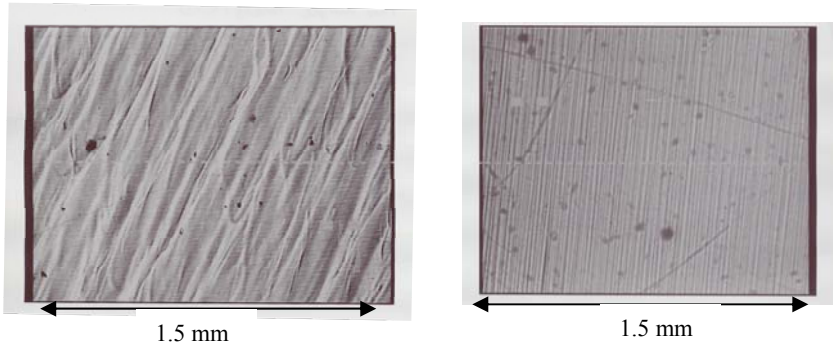

Fig. 2-4. *Nd^{3+}doped KPb_2Br_5 crystalline samples: Microscopic pictures indicate structural deviations such as mosaic structure (left) and growth striae (right) for rare earth-doped bromide crystals which have a high impact on lasing these materials. Black spots are e.g. due to lead inclusions.*

However, the structural deviations have a major impact on lasing these crystalline materials. Scattering and beam splitting was observed by using a Helium-Neon laser going through the crystals. While for an undoped sample multispots seem to be not existent (Fig. 2-5(left)) it seems that the effect of beam splitting (Fig. 2-5(right)) increases with increasing dopant concentration. The use of a CO_2 laser at 10.6 μm - in the LWIR region of interest - gives transmission losses ranging from 20-40 % (includes Fresnel losses) for the Tb^{3+}-doped KPB samples. No multispots were observed, but this can be due to the simple detection system of using heat film and therefore, this loss mechanism can still be present preventing the bromide samples from lasing in the LWIR region. Attempts of lowering the translation velocity from 1 mm/hr to 1mm/day as well as the use of low dopant concentrations seem to give the best results in crystal quality. Due to the previous stated observations it is believed that the

[5] The possible occurrence of other imperfections such as twinning needs to be further investigated.

incorporation of RE^{3+} ions has a major impact regarding the formation of structural imperfections in the bromide crystals. A comparison of the ionic radii of the active dopant ions and the substituted host lattice site will be given in the next section.

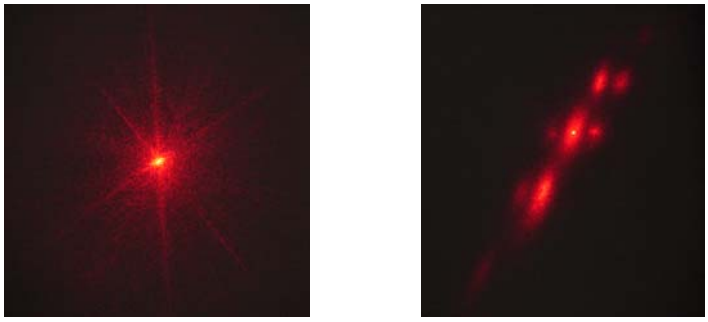

Fig. 2-5. *Scattering and beam splitting (right) of a HeNe laser going through an undoped (left, path length ~ 3 mm) and a Tb^{3+}-doped KPb_2Br_5 sample (right, path length ~ 7.6 mm, Tb concentration ~ $1.8x10^{20}$ cm^{-3}). The beam splitting is believed to increase with higher dopant concentration of the rare earth ion.*

An absorption spectrum taken in the long wavelength region (Section 3.1, Fig. 3-2) shows also the presence of water/OH^- [Mcc78] and/or NH_4^+ ([Poh32], [Rei21], [Crc82]) at a peak value of 3.13 μm and at 7.18 μm which if not suppressed might compromise laser action in rare earth-doped MPb_2Br_5 (M= Rb, K) crystals such as terbium. In the Tb:KPB absorption spectra (Section 3.2.2.1, Fig. 3-1) an additional peak at ~ 6.2/6.3 μm was observed possibly resulting from NH_3 [Pug76] or water. The height of these absorption peaks relative to the absorption peaks of the rare earth ions vary from crystal to crystal (section 3.3.1). In order to reduce the water content in the Tb:KPB crystals, before synthesis, the stoichometric material was heated at 150°C (Fisk University) or 230°C (EIC Laboratories) under dynamic vacuum. Also, as described above the crystals were grown and/or synthesized in sealed quartz ampoules with argon or Br_2 overpressure to reduce the water content.

2.1.2 Physical Properties

The investigated moisture-resistant crystals KPb_2Br_5 and $RbPb_2Br_5$ belong to the same chemical compound family APb_2X_5, where A= K, Rb, NH_4 and X= Cl, Br, I. KPb_2Br_5 and $RbPb_2Br_5$ have different crystal structures. The $RbPb_2Br_5$ crystal is uniaxial and has a tetragonal crystal structure with space group symmetry I4/mcm (point group symmetry 4/mmm) [Pow37]. With the lattice constants a = 8.41 Å, c = 14.5 Å, and Z=4 ([Pow37], [Col71]) the density is determined to be 5.82 g/cm^3. The KPb_2Br_5 crystal is biaxial and has a monoclinic crystal structure with a space group symmetry $P2_1/c$-C_{2h}^5 (established by reflection analyses), point group symmetry 2/m, and the C_2 axis along b in the unit cell. From an x-ray

single crystal diffraction study of KPb_2Br_5 the lattice parameters were determined to be a = 9.256(2) Å, b = 8.365(2) Å, c = 13.025(3) Å, β = 90.00(3)º. These values were obtained for crystals evidencing substantial structural imperfections. For crystals with no structural imperfections the given lattice parameters are observed to change to e.g. higher β values, but further work at Design and Technological Institute for Monocrystals is needed to clarify this situation for both crystalline host materials. The number of molecules in a unit cell is Z=4. With the lattice constants the KPb_2Br_5 density is determined to be 5.62 g/cm^3 which matches the value of 5.60 g/cm^3 found in the literature [Col71]. In previous studies it was observed that the monoclinic [Bec86a] or orthorhombic [Jan68] structure is formed under high temperature whereas a tetragonal ([Jan68], [Pow37], [Bec86a]) or orthorhombic [Col71] structure appeared under low temperature. A tetragonal structure was also found under high pressure [Bec86a]. Studies at Fisk University revealed that the crystal structure of the KPb_2Br_5 crystals grown by Bridgman method is monoclinic up to 200°C and fully transforms to orthorhombic at 300°C (described in detail in publication 6, see list of publications).

Table 2-1. *Coordination number dependent ionic radii (6-fold and 7-fold) of trivalent Nd^{3+}, Eu^{3+}, $Tb^{3+}$and of the substituted divalent Pb^{2+} ion in fluoride surrounding [Kam90]. Bromide surrounding was not found in the literature, but the relation is assumed to be similar.*

Ion	Ionic radius [Å] (coordination number)
Nd^{3+}	1.14 (6), -
Eu^{3+}	1.09 (6), 1.17 (7)
Tb^{3+}	1.06 (6), 1.16 (7)
Pb^{2+}	1.32 (6), -

It is believed that the KPB crystals are isomorphous to $RbPb_2Cl_5$ with two [Nit95] non-equivalent Pb^{2+} sites.[6] The rare earth ions replace Pb^{2+} ions with associated K^+/Rb^+ vacancies which are assumed to be responsible for charge compensation (similar to KPb_2Cl_5) [Isa98]. KPb_2Cl_5 and $RbPb_2Cl_5$ have monoclinic crystal structure [Nit95] like the KPb_2Br_5 crystal. It was proposed for KPC that RE^{3+} ions substitute Pb^{2+} at two sites [Nit95]. One site is 7-fold coordinated with 6 ions approximately octahedral orientated and one ion close nearby (coordination polyhedra are shown in [Nit95] and [Nos00b]), and a low symmetry one with the coordination number 9, 7 or 6 ([Nit95], [Tka02b], [Yel02]). Predominant substitution into the first one is observed [Tka02b]. This is believed to be similar for the investigated KPB crystals. Further studies are needed for RPB. At DTIM it is believed that there is probably only one lead site in RPB which is 8-fold coordinated. However, Table 2-1 shows a comparison of the different trivalent rare earth dopant ions and the divalent lead site. The observed differences in the ionic radii can cause the crystal quality issues discussed in the previous section.

[6] Four lead places were once reported in Nikl et al. [Nik91].

The thermal conductivity was measured at EIC Laboratories, Inc. to be 4.2 W/mK for KPB and 3.4 W/mK for RPB which is smaller than 4.6 W/mK determined for KPC.

The Nd, Tb, and Eu concentrations in the investigated crystals were measured with the inductively coupled plasma-mass spectrometry technique or by microprobe analysis (this wavelength dispersive x-ray analysis is further described in [Rad00]) and are noted in the individual sections of chapter 3. Both methods are not able to distinguish between different valencies of the incorporated ions.

Table 2-2. *Refractive indices of MPb_2Br_5 (M=K, Rb).*

λ [nm]	n	
	KPb_2Br_5 (+/- 5 *10^{-3})	**$RbPb_2Br_5$** (+/- 1 *10^{-3})
633	n_x= 2.191 n_y= 2.189 n_z= 2.247	n_o= 2.2410 n_e = 1.9654
1500	n_x= 2.104 n_y= 2.102 n_z= 2.148	n_o= 2.1718 n_e= 1. 9339
4000	n_x= 2.091 n_y= 2.089 n_z= 2.133	n_o= 2.1548 n_e= 1. 9245

The refractive indices of pure KPb_2Br_5 and $RbPb_2Br_5$ were measured at DTIM with the prism technique and are given in Table 2-2. The averaged refractive index of KPb_2Br_5 at 633 nm matches the value of n=2.2 estimated by comparison of the refractive indices of $PbBr_2$ [Ren00], $PbCl_2$ [Web86] and KPb_2Cl_5 [Nos01].

Table 2-3. *Physical properties of MPb_2X_5 (M=K, Rb; X=Br, Cl).*

Host	**KPb_2Br_5**	**$RbPb_2Br_5$**	**KPb_2Cl_5**	**$RbPb_2Cl_5$**	[Ref.], collaborator
Space group*	$P2_1/c$	I4/mcm	$P2_1/c$	$P2_1/c$	[Pow37], [Nit95], DTIM
Lattice symmetry	monoclinic	tetragonal	monoclinic	monoclinic	
Number of molecules/unit cell	4	4	4	4	[Nit95], DTIM
Lattice parameters	a= 9.256 Å b= 8.365 Å c= 13.025 Å	a= 8.41 Å c= 14.50 Å	a= 8.831 Å b=7.886 Å c= 12.430 Å	a= 8.915 Å b= 7.950 Å c= 12.445 Å	[Nos01], [Nit95], DTIM
Density	5.62 g/cm^3	5.82 g/cm^3	4.84 g/cm^3	5.10 g/cm^3	This study
Band gap	3.5 eV	3.4 eV	4.0 eV	-	DTIM
Melting point	382 °C	382 °C	434°C	423°C	[Col71], [Gab85], [Nit95] [Nit96]
Thermal conductivity	4.2 W/mK	3.4 W/mK	4.6 W/mK	-	EIC
Mohs-hardness	-	-	2.5	-	DTIM

*as further described in [Hah95]

The result of the refractive index measurements of $RbPb_2Br_5$ indicates large birefringence in this negative uniaxial crystal ($n_o > n_e$; n_x, $n_y = n_o$; $n_z = n_e$). The energy gap between the valence and conduction band of KPB (~ 3.5 eV), RPB (~ 3.4 eV), and KPC (~ 4.0 eV) was determined at DTIM by analyzing the absorption edge of the host material. Some of the physical properties of the investigated host materials in comparison to their chloride analogs are summarized in Table 2-3. Here, the higher density of the bromides versus the chlorides can also be seen. Note, that features like phonon energy and transparency range are described in section 3.1.

2.2 Measurements and Data Evaluation

In this section a description of the experimental setups for the different measuring techniques is provided. Moreover, it is shown how the characteristic values e.g. absorption cross sections are calculated.

2.2.1 Raman Scattering

Phonon energies of host crystalline matrices can be determined by the inelastic scattering of photons on the crystalline lattice, so called Raman scattering (photon experiences frequency shift). Raman scattering spectra (section 3.1) from single crystals were obtained by using a DilorXY Triple Ramanspectrophotometer (1.5 cm^{-1} spectral resolution), a CCD camera, and a 532 nm Nd:YVO_4 laser excitation for the bromide samples (University of Hamburg) or a Ramanor U-1000 spectrometer (1 cm^{-1} spectral resolution), a CCD camera, and a 514 nm argon-laser excitation for the chloride crystals (DTIM).

2.2.2 Absorption

The absorption spectra (section 3.2) were taken at LLNL with a commercial Perkin Elmer Lambda 9 UV/VIS/NIR spectrophotometer, a Perkin Elmer 983 Infrared spectrophotometer, and/or a Fourier Transform Infrared (FTIR) spectrophotometer. Alternatively, transmission measurements e.g. for the Stark level determination at low temperatures (10 K and 77 K) were performed with part of the experimental setup shown in Figure 2-7, section 2.2.6 (no pump just probe source involved).

The decrease in intensity of the incoming beam I_0 by passing through the absorbing medium of length l can be described by Lambert-Beer's law. For small intensities the transmitted intensity I is given by:

$$I(\lambda) = I_0(\lambda) \cdot e^{-\alpha(\lambda) \cdot l} \qquad (2\text{-}1)$$

From this it follows that the absorption coefficient can be written as:

$$\alpha(\lambda) = \frac{1}{l}\ln\left[\frac{I_0(\lambda)}{I(\lambda)}\right] = \frac{1}{l \cdot \log e}\log\left[\frac{I_0(\lambda)}{I(\lambda)}\right], \qquad (2\text{-}2)$$

where the optical density ratio (extinction) OD=log[$I_0(\lambda)/I(\lambda)$] is measured by the two beam Perkin Elmer spectrophotometers or in case of using the setup in Figure 2-7 by measuring the spectrum with and without crystal sample.

With the absorption coefficient α and the concentration of the absorption centers (e.g. ions) n_{ion} the absorption cross section $\sigma(\lambda)$ was calculated by:

$$\sigma(\lambda) = \frac{\alpha(\lambda)}{n_{ion}} \qquad (2\text{-}3)$$

The cross sections were used to calculate the transition probabilities given in section 3-2 by using the Judd-Ofelt theory described in section 1.2.2.1. Note, that it is not possible to distinguish between the different absorbing centers with this method in contrast to excitation measurements (section 2.2.4).

2.2.3 Emission

The (blackbody corrected) emission spectra of Nd:KPB and Nd:RPB crystalline samples (section 3.2.1.2, section 3.4, and section 3.7) were obtained by using a liquid nitrogen cooled InSb-detector, a ½ m- monochromator [500 nm blazed grating (1200 l/mm), 1μm blazed grating (600 l/mm) or 2μm blazed grating (300 l/mm)], and a Ti:Sapphire laser to excite the $^4F_{7/2}$ level at a wavelength of 0.75 μm, the $^4F_{5/2}$ level at 0.81 μm, or the $^4F_{3/2}$ level at 0.89 μm. Upconversion emission spectra (section 3.7) were obtained by using a Silicon detector or photomultiplier with S-1 characteristic. The blackbody correction was performed with a tungsten lamp or other appropriate (commercially available) sources. Optical pyrometers were used to determine their temperature. The emission cross sections are calculated by using the Fuechtbauer-Ladenburg equation as described in section 1.2.2.2 (Eqn. 1-9).

The (blackbody corrected) room temperature emission spectra of Tb:KPB (section 3.2.2.2) were measured by pumping into the $^7F_2$ level using a pulsed Co:MgF_2 laser tuned to ~ 2 μm and a 1m-McPherson Monochromator (4 μm blazed grating, 150 l/mm) or a ¼ m Digikroem Monochromator (4 μm blazed grating, 150 l/mm or 8 μm blazed grating, 75 l/mm), together with appropriate long pass filters. The 3 μm fluorescence was detected with a liquid nitrogen cooled InSb-detector (and pre-amplifier) and the 8 μm and 5 μm fluorescence was measured by using a liquid nitrogen cooled HgCdTe-detector (and pre-amplifier). The emission cross

section was also determined with the Fuechtbauer-Ladenburg equation, using the branching ratios and radiative lifetimes calculated from the Omega values (section 3.2.2).

For the temperature dependent measurements a helium cryostat system was used. While for the spectra in the visible and NIR windows made of e.g. fused Silica (transmissive ~ 0.19-2.5 μm [Red05]) or BK7 glass (transmissive ~ 0.33-2.1 μm [Red05]) are sufficient, the determination of LWIR spectra needed special windows transmissive for the particular wavelength region. Here, (AR coated) ZnSe (transmissive ~ 0.5-22 μm [Kor04]) or CaF_2 (at least transmissive ~ 0.17-7.8 μm [Red05]) windows were used. Likewise, appropriate short pass and long pass LWIR filters like thin film filters made out of thin film layers processed onto substrates like germanium (max. transmissive 2-12 μm [Alm04]) or semiconductor material filters as well as ZnSe or CaF_2 lenses were used.

The signal was processed using lock-in amplifiers or boxcar averagers together with a computerized readout. The additional use of boxcars was especially important for the measurements in section 3.3.3 where different settings of the time gate were necessary in order to distinguish between different emission signals.

2.2.4 Excitation

Excitation spectra were measured with a Fluorolog 3-21 unit (Fig. 2-6). Excitation source was a continuous high pressure Xenon-lamp. The excitation light enters the sample chamber through a double-grating monochromator. The fluorescence of the crystal sample was detected with a one-grating monochromator and a photomultiplier (PM) by using appropriate edge filters. For the low temperature excitation spectra at 10 K a closed-cycle Helium cryostat was installed in the sample chamber. Excitation spectra determined during the course of the upconversion study (section 3.7) were measured in the same setup as used for emission spectra, but in this case the wavelength of the Ti:Sapphire was scanned, while the monochromator wavelength was fixed.

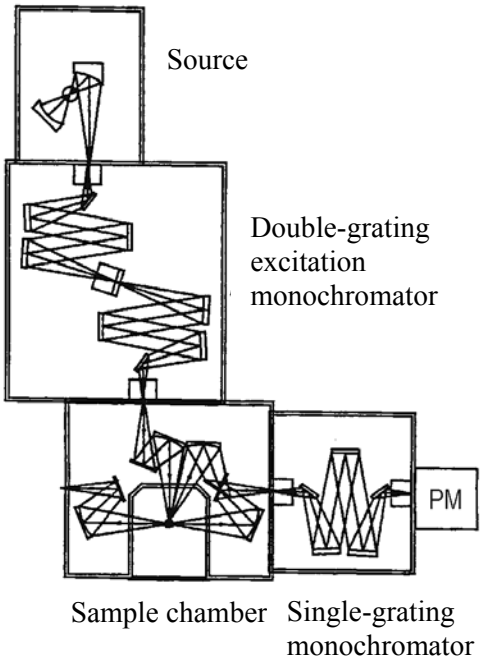

***Figure 2-6**. Fluorolog Setup [Isa96].*

2.2.5 Emission Lifetime

The fluorescence decays - in the visible and near infrared - from emitting levels of Nd^{3+}-doped MPX (M=Rb, K, X=Cl, Br) samples were usually measured with a ¼ m monochromator, a photomultiplier with S-1 characteristic, appropriate filters to block unwanted wavelengths, and an OPO system used to excite the $^4F_{3/2}$ or $^4F_{5/2}$+ $^2H_{9/2}$ levels (or higher lying levels as noted in the particular section), to observe their emission. Exponential fits of the lifetimes were deduced, as listed in Table 3.4, section 3.2.1.3 and section 3.7. For longer wavelengths only an appropriate detector and filters were used for detection.

The emission liftimes of mainly the $^7F_4$ level and $^7F_5$ level of Tb:KPB samples (section 3.2.2.3 and 3.3) were determined in the temperature range ~ 30 K – 300 K by exciting the $^7F_2$ level (Fig. 3-7) with a Co:MgF_2 laser tuned to 2.0 μm. The resulting fluorescence was captured by a liquid nitrogen cooled HgCdTe-detector and pre-amplifier or InSb-detector and pre-amplifier. The different transitions were distinguished by using appropriate long pass and short pass filters. For some lifetime measurements a ¼ m monochromator (4 μm blaze grating, 150 l/mm or 8 μm blaze grating, 75 l/mm) was used additionally. The lifetimes were determined by an exponential decay fit. For low temperature measurements a He-Kryostat with AR coated ZnSe windows was placed directly at the entrance slit of the Digikroem monochromator.

2.2.6 Pump-Probe- and Gain-Measurements

Beside the ground state absorption (section 2.2.2) the excited state absorption and reabsorption are important absorption processes. The excited state absorption is similar to ground state absorption with the difference that the absorption results from an excited state. This process can be seen as a loss mechanism if the initial level is an upper laser/pump level (depopulation and therefore, e.g. lower efficiency) or as a feasible intraionic upconversion mechanism to populate higher lying levels with respect to upconversion lasing. If a lower (laser) level is long lived reabsorption can occur. Reabsorption is a process where the stimulated or spontaneous emitted photon is absorbed again by the same activator type. In particular in dense media the radiation is trapped. It is known as a loss mechanism especially for ground state lasers.

Excited state absorption and reabsorption spectra for the Nd-doped bromide and chloride crystals (section 3.6) were determined by a pump and probe method using the setup in Figure 2-7. The technique described in the following was previously used to study e.g. Nd^{3+}-doped oxides and fluorides like $Y_3Al_5O_{12}$, $YAlO_3$, Y_2O_3, YVO_4, $GdVO_4$, $Sr_5(PO_4)_3F$, $LaSc_3(BO_3)_4$,

$CaWO_4$, $YLiF_4$, etc. ([Kue98], [For98], [For99]). An unpolarized halogen lamp was used as the probe source while a cw Ti:Sapphire laser tuned to 0.75 μm, 0.81 μm, and 0.89 μm pumped the $^4F_{7/2}$+$^4S_{3/2}$ level, $^4F_{5/2}$+$^2H_{9/2}$ level, and $^4F_{3/2}$ level, respectively.

The crystals were placed behind a 500 μm diameter pinhole, to ensure good overlap between pump and probe beam. The transmitted intensity was detected by using a liquid nitrogen cooled InSb-detector and a ½ m, 1μm blazed grating (600 l/mm) monochromator. In the double modulation technique described in detail by Koetke *et al.* [Koe95] two lock-in amplifiers were used. The first lock-in amplifier detected the probe signal I_u modulated by a high frequency chopper (~ 1 kHz). The second lock-in amplifier isolates and amplifies the signal difference I_p-I_u of the pumped and unpumped signal intensity using a low frequency chopper (~ 10-15 Hz) to modulate the pump beam. The difference of the pumped and unpumped signal intensity I_p-I_u as well as the transmitted signal intensity I_u in absence of the pump beam are detected simultaneously.

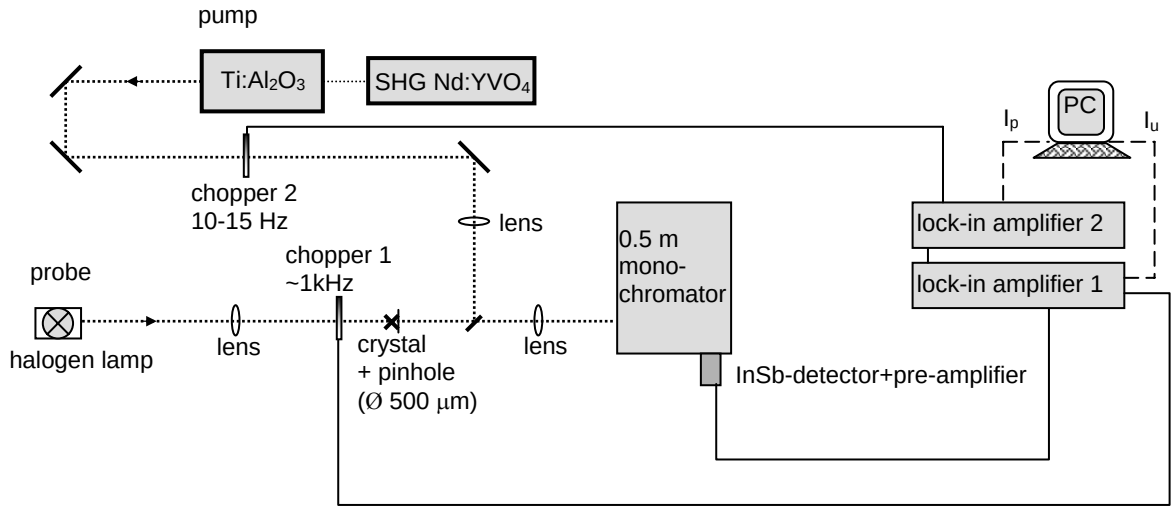

Figure 2-7. *Experimental setup of the cw pump-probe technique*

The following equation illustrates the relation between the measured signal intensities and the competing ground state absorption (GSA), stimulated emission (em), excited state absorption (ESA), and reabsorption (RA) processes as shown for $I_p \approx I_u$ (valid in the case of small pump power densities meaning when the number of excited ions is small compared to the ground state density in the crystal):

$$\frac{I_p - I_u}{I_u} = C \cdot n_e \cdot l \cdot [\sigma_{GSA} + \sum_i \frac{n_i}{n_e}(\sigma_{em,i} - \sigma_{ESA/RA,i})] \qquad (2\text{-}4)$$

where C is a constant, σ_{em}, $\sigma_{ESA,RA}$, σ_{GSA} are the cross sections, *l* the transmission path length, n_i is the population density of level i, and $n_e = \Sigma n_i$ the total excitation density summed over all

excited levels i. Appendix C reveals how this equation is determined. When ESA and/or reabsorption processes predominate the measured signal is negative while the signal is positive due to bleaching and/or stimulated emission.

In this study the determination of ESA cross sections appeared to be difficult due to the fact that more than one metastable level is significantly populated in these materials. Here, the upper laser levels such as the $^4F_{3/2}$ and $^4F_{5/2}+^2H_{9/2}$ levels, as well as the lower long lived laser levels ^4I_J (J= e.g. 11/2, 13/2), contribute to the relevant population densities. Reabsorption competing with stimulated emission and/or ground state absorption occuring in the same wavelength region makes it difficult to establish an accurate value for the ESA cross section. Thus, a more qualitative discussion of the spectra is presented which includes the calculation of effective cross sections (section 3.6, eqn. 3-12) and line strengths of electric and magnetic dipole transitions (section 1.2.2.2 and section 3.6). The emission spectra presented in section 3.6 were performed by using the same monochromator-detector system and excitation source as described for the pump-probe spectra.

Gain measurements were attempted with a similar setup like shown in Figure 2-7 using different pump and probe sources. For the time resolved gain measurements around ~ 1.06 μm and 0.965 μm a laser diode (tunable in the case of 1.06 μm) was used as the probe source, and a pulsed Cr:LiSAF laser (167 μs pulse length, 1-2 Hz rep. rate) was used as the pump source. Instead of using a monochromator detector system the light was captured directly with an InGaAs detector mounted onto an integrating sphere by using appropriate bandpass filters.

2.2.7 Laser Experiments

Laser experiments for the polished, uncoated Nd-doped samples were attempted with three different pump lasers: a chopped cw-Ti:Sapphire, a pulsed Cr:LiSAF laser (167 μs pulse length, 1-2 Hz rep. rate), and a short pulsed OPO-system (10 ns pulse length, 10 Hz rep. rate) tuned to 0.89 μm and 0.81 μm to pump the $^4F_{5/2}+^2H_{9/2}$ level and $^4F_{3/2}$ level, respectively.

A nearly concentric cavity was used for the laser experiments at the University of Hamburg by the use of mainly an OPO system as a pump source and for some attempts also a Ti:Sapphire laser. Laser activity was achieved (section 3.5) with two 100 mm concave laser mirrors (high reflector transmission for the pump wavelength, output coupling as described in section 3.5) and using the OPO system. The pump spot size in the crystal was ~ 100 μm (radial). Mode matching between pump spot and the cavity mode has been achieved by optimizing the resonator length.

Laser experiments at LLNL have been attempted with a Cr:LiSAF laser as a pump source using a confocal cavity. Concave laser mirrors with a radius of curvature (ROC) of 5 cm were used. These are high transmissive at the pump wavelengths 0.81 μm and 0.89 μm, high reflecting at the wavelengths 1.19 μm, 1.06 μm and/or 0.96 μm and have an output coupling of 5%.

Laser experiments with the Tb-doped samples were attempted at LLNL in a concentric cavity for e.g. the 8 μm transition with a Co:MgF_2 laser (~ 50 μs pulse length, 1-5 Hz rep. rate) tuned to 1.97 μm to pump the $^7F_2$ level. This pump wavelength was chosen because the 8 μm AR coated ZnSe mirrors (ROC ~ 20 cm) are highly transmissive at 1.97 μm. The pump spot size was measured to be ~ 144 μm, and the laser spot size ~ 160 μm. In future laser experiments – possibly also at low temperature - a 3μm Er:YAG laser might be anticipated to pump directly into the upper laser level $^7F_4$. Here, Kryostat windows out of ZnSe as well as the laser mirrors were chosen to be transmissive for the emission- and/or pump wavelength of interest.

The threshold energy for pulse operation can be estimated by use of [Nos00b]:

$$E_{p,th} = [\pi(w_p{}^2 + w_l{}^2)/4(\sigma_{em} - \sigma_{esa}][hc/\lambda_p][L+T][T_S(1-e^{-\alpha l})\eta_P]^{-1} \qquad (2\text{-}5)$$

where λ_p is the pump wavelength, w_l the cavity mode size (radial), w_p the beam pump spot size (radial), σ_{em} the emission cross section, σ_{esa} the ESA cross section, L the passive losses, T the losses due to output coupling, T_s the transmission into the sample, (1-exp(-αl)) the absorbed pump power, and η_p the pump pulse efficiency.

3. Spectroscopy and Laser Operation

3.1 Phonon Energies of Bromides Versus Other Host Crystals

In this section the phonon energy of MPB in comparison to MPC (M=K, Rb) (Fig. 3-1) as well as of other host materials is shown. For this investigation undoped KPB, KPC, and RPC single crystals were grown in Novosibirsk, Russia and an undoped RPB crystal was grown in Prague, Czech Republic.

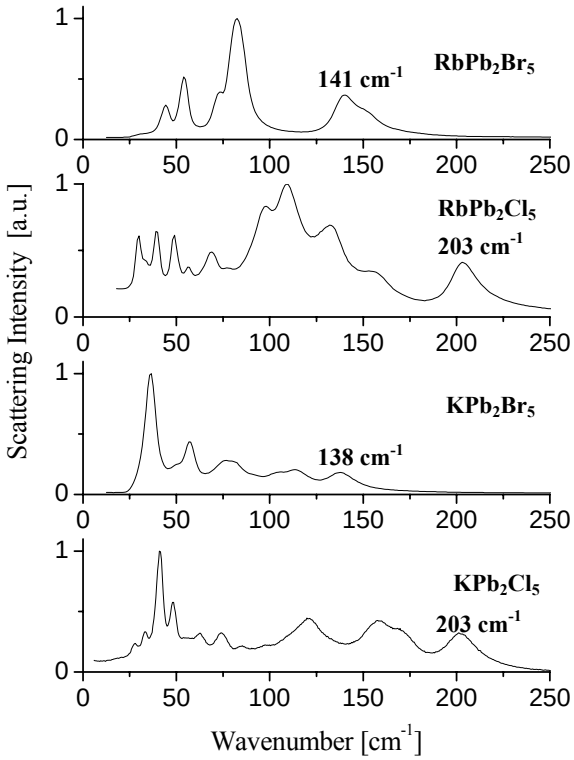

***Fig. 3-1**. Raman scattering spectra: the maximum phonon energies in the MPb_2Br_5 crystals (M= K, Rb) are even lower than those of the MPb_2Cl_5 crystals.*

The phonon energy of KPB was obtained by taking a Raman scattering spectrum (section 2.2.1) from a single KPb_2Br_5 crystal. The maximum phonon energy was determined from the highest energy peak to be 138 cm^{-1} (Fig. 3-1). The phonon energy of a single RPB crystal was measured with the same setup to be 141 cm^{-1} (Fig. 3-1). The phonon energy for $RbPb_2Cl_5$ (203 cm^{-1}, Fig. 3-1) was measured in the course of this study from a single $RbPb_2Cl_5$ crystal to be the same as the phonon energy of KPb_2Cl_5 (Fig. 3-1) ([She03], [Nos01]). As expected the phonon energies of the bromide crystals are lower than those of the chloride crystals because of the higher mass of the vibrating constituents (section 1.1, eqn. 1-1). As for the

monoclinic KPb_2Cl_5 structure [Nos01][7] it is believed that the observed spectrum of e.g. KPb_2Br_5 can be described in terms of K^+, Br^-, and Pb^{2+} activity. The lower energy features could be due to Pb^{2+} modes (due to the high mass), while the features above might be associated with vibrations involving also Br^- and K^+ (including bonds of K-Br, Pb-Br etc.). Note, that the covalency increases for the Pb-X bond (X= Cl, Br, I) along Cl→Br→I and therefore, could also modify the effective force constant [Nik91]. In principle, this could also cause a change in the phonon energy, but at this point it is assumed that the change in the mass is the main factor.

The similar maximum phonon energies of KPC and RPC as well as of KPB and RPB confirm that the different halogen anions mainly cause the change in the maximum phonon energies. The phonon energies are reduced by a factor of ~ 1.5, which is close to the change predicted on the basis of the square root of the reduced masses of bromide and chloride ions [Ric63].

As it will be shown (section 3.2 and 3.3), taking the maximum peak value of the highest Raman energy phonon band can be a first approximation for calculating the number of phonons 'p' (section 1.2.3) involved in the process in order to determine the nonradiative rates. However, as it will be shown in section 3.3, a maximum phonon energy value taken from the wing of the Raman spectrum is the best fit representation of the effective phonon energy $\hbar\omega_{eff}$.

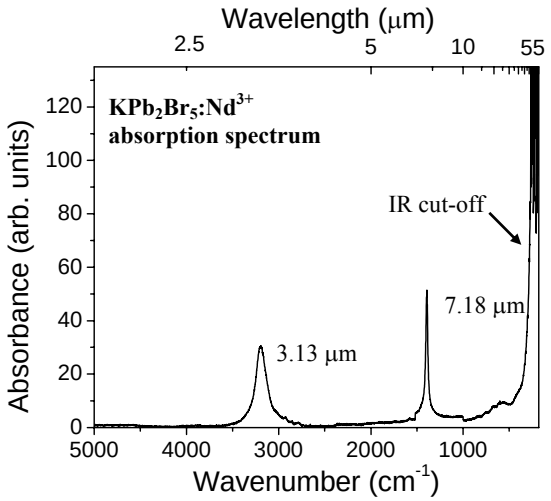

***Fig. 3-2**. Absorption spectrum of $KPb_2Br_5:Nd^{3+}$: The IR cut-off in the long wavelength region gives a phonon energy of 130 -140 cm^{-1}. The relatively sharp feature near 1400 cm^{-1} is due to the presence of NH_4^+ ions, and the broader feature near 3200 cm^{-1} is due to e.g. OH^- ions and/or NH_4^+ ions.*

[7] In KPC 96 dispersion branches are expected as $24A_g + 24B_g + 24A_u + 24B_u$ [Nos01]. The superposition of these branches produces the ~ 15 bands resolved in the phonon energy spectrum of KPC (Fig. 3-1).

The absorption spectrum of $KPb_2Br_5:Nd^{3+}$ shown in Fig. 3-2 was measured with the Perkin-Elmer Lambda 983 spectrophotometer (section 2.2.2). From the IR cut-off in the long wavelength region the maximum phonon energy of the KPb_2Br_5 crystal is estimated to be 130 cm^{-1} by comparison with the IR cut-off and maximum phonon energy of KPb_2Cl_5. A value of 140 cm^{-1} is found when the author determines it directly from the IR cut-off of KPb_2Br_5, assuming that the IR cut-off occurs with a two phonon absorption [Nos00]. These values are consistent with the phonon energy determined by Raman spectroscopy. The transparency region of KPB and RPB is ~ 0.35-35 μm and ~0.36-35 μm, respectively, determined from the IR cut-off and by analyzing the absorption edge in the short wavelength region of these crystals (section 2.1.2).

Table 3-1. *Max. phonon energy E_{phonon} of various host crystals ([Kam96],[Nos01],[Gue00], [Heh94],[Rie95],[She03], [Ree73] and this study).*

Host	**E_{phonon} [cm^{-1}]**
YVO_4	880, 943
$Y_3Al_5O_{12}$	700
$YAlO_3$	550-600
Y_2O_3	430-550, 600
$YLiF_4$	400, 560
SrF_2	350, 360
LaF_3	305, 350
$Cs_3Er_2Cl_9$	285
$LaCl_3$	260
$RbPb_2Cl_5$	203
KPb_2Cl_5	203
$Cs_3Er_2Br_9$	190
$LaBr_3$	175
$CsCdBr_3$	163
$Cs_3Er_2I_9$	160
$RbPb_2Br_5$	141
KPb_2Br_5	138

The phonon energies of MPX (M=Rb, K; X= Br, Cl) in comparison to other host crystals are summarized in Table 3-1. The listed phonon energies are mainly determined from Raman scattering spectra instead of using temperature dependent lifetime measurements (energy gap law). It clearly shows that fluoride and oxide materials can not compete as materials for LWIR applications due to their higher phonon energies caused by the lower mass of the vibrating constituents. Most of the bromide, chloride, and iodide materials such as $LaBr_3$ and $LaCl_3$ are known to be highly hygroscopic and of higher phonon energy if compared with KPB and RPB. In systems such as $CsCdBr_3$ [Coc92] and $Cs_3Er_2X_9$ (X= Cl, Br, I) [Heh94] dimer-formation can be problematic since it can increase all types of non-radiative energy transfer processes e.g. cross relaxation rates.

Future studies on further AB_2X_5 (X= Cl, Br, I) compounds ([Loe03], [Bec86a], [Bec86b]) could help to determine possible influences of the A and B ions on the phonon energy spectrum in more detail and to find further potential hosts. In order to achieve even lower phonon energies the growth of iodides was attempted, but unsuccessful. At this point mixtures of bromide and iodide ions are suggested to stabilize the system in order to

possibly succeed in even lower phonon energy host materials. The growth of mixtures are successfully shown for other hosts e.g. $AgCl_xBr_{1-x}$ [Dek02], $CsPbCl_2X$ (X=Br, I), and $CsPbCl_{3x}Br_{3(1-x)}$ [Pid97] (x=0...1).

3.2 Slow Nonradiative Decay for RE^{3+}-Doped Bromide Crystals

Due to the low-phonon energies presented in the previous section it is in particular interesting to actively dope these bromide materials since low nonradiative transition rates are expected. The results of the spectroscopic investigation described in this section include absorption spectra, emission spectra, and emission lifetimes recorded for Nd^{3+}-, Tb^{3+}-, and Eu^{3+}-doped MPB (M=K, Rb) samples at room temperature. Calculations of cross sections, Judd-Ofelt parameters and radiative transition probabilities for relevant (laser) transitions as well as calculations of multiphonon decay rates are included.

3.2.1 Nd^{3+}-Doped KPb_2Br_5 and $RbPb_2Br_5$ Crystals

Nd^{3+} incorporated in different host materials is one of the most studied rare earth ion in crystalline host laser materials since it possesses sufficiently intense absorption and luminescence transitions for excitation and production of stimulated emission. Due to its complex energy level structure (Fig. 3-3) it offers various laser transition wavelengths ([Kam90], [Kam96]). As revealed in the following new (possible) laser transitions resulting from e.g. the $^4F_{5/2}+^2H_{9/2}$ level, in addition to conventional laser transitions from the $^4F_{3/2}$ level can be shown in KPB and RPB due to its previously described properties.

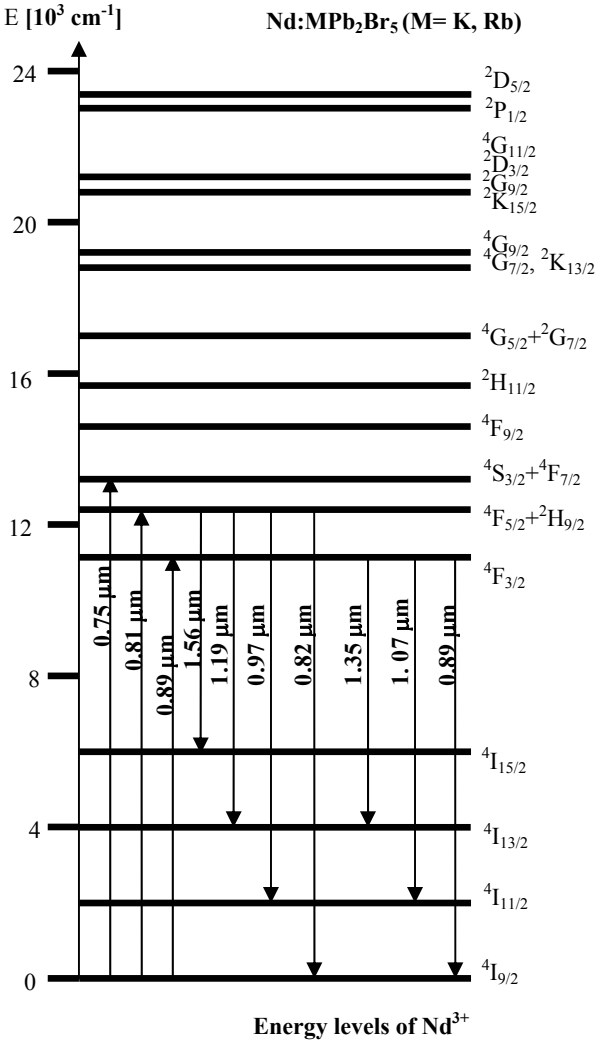

***Fig. 3-3**. Energy level diagram of Nd:MPB (M= K, Rb) displays (possible) new laser transitions from the $^4F_{5/2}+ {}^2H_{9/2}$ level, in addition to conventional laser transitions from the $^4F_{3/2}$ level. Possible pump wavelengths are indicated.*

3.2.1.1 Absorption and Radiative Transition Probabilities

The unpolarized absorption spectra (Fig. 3-4) taken with a commercial Perkin-Elmer Lambda 9 spectrophotometer show peaks assigned to transitions (Fig. 3-3) of the Nd^{3+} ion in KPB and RPB. In these spectra, absorptions due to long tails originating from the band edges at the shorter wavelengths have been subtracted. For the determinations of absorption cross sections, dopant concentrations of $5.59x10^{+18}$ cm^{-3} or Nd 0.023 wt% for the RPB crystal, and $9.38x10^{+18}$ cm^{-3} or Nd 0.04 wt% for the KPB crystal were used. These concentrations were determined with the inductively coupled plasma-mass spectrometry technique (section 2.1).

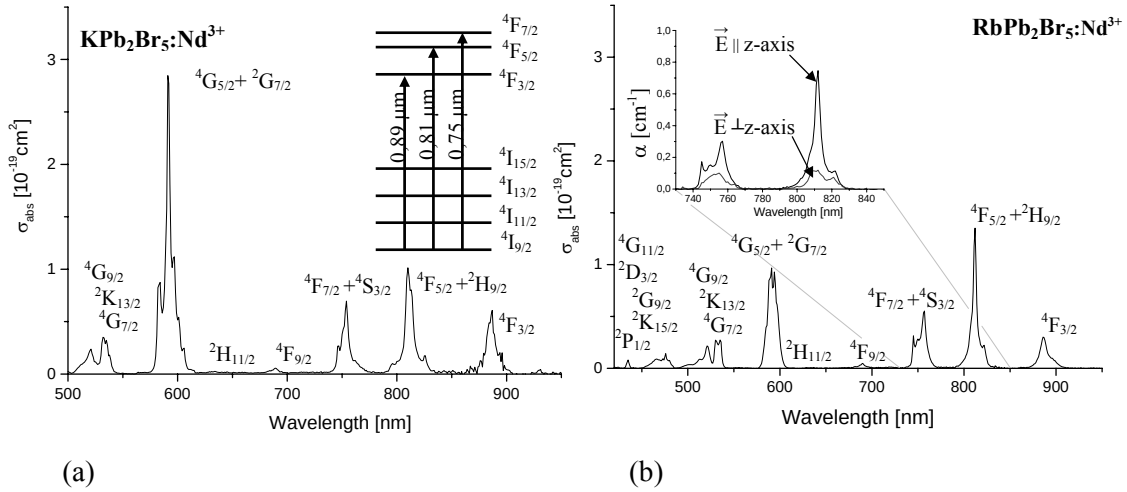

Fig. 3-4. *Absorption spectra of Nd^{3+} doped KPb_2Br_5 (a) and $RbPb_2Br_5$ (b) shows peaks assigned to transitions of the Nd^{3+} ion. Host crystal absorptions at the shorter wavelengths have been subtracted. The polarized absorption spectrum inset in (b) shows the importance of the crystal orientation for pumping the ^4F levels in future laser experiments.*

Note the hypersensitive nature (section 1.2.2.1) of the $^4G_{5/2}+^2G_{7/2}$ band in Nd:KPB in contrast to Nd:RPB.

Especially in the Nd^{3+}-doped RPB crystal a strong dependence of absorption on polarization is observed. The absorption spectrum inset in Fig. 3-4 (b) shows the importance of the crystal orientation for pumping the $^4F_{5/2}+ {}^2H_{9/2}$ level at 0.81 μm or the $^4F_{7/2}$ level at 0.75 μm in laser experiments.

The following host-dependent Judd-Ofelt intensity parameters Ω_t (t= 2, 4, 6) (section 1.2.2.1) of Nd:KPB were determined by taking into account eight unpolarized absorption bands in the spectral range 500 nm - 1000 nm and assuming that some of them are comprised of two transitions (Fig. 3-4 (a)):

$$\Omega_2 = 15.7 \times 10^{-20}\ \mathrm{cm}^2$$
$$\Omega_4 = 6.3 \times 10^{-20}\ \mathrm{cm}^2 \qquad (3\text{-}1)$$
$$\Omega_6 = 3.0 \times 10^{-20}\ \mathrm{cm}^2$$

By comparing the results with a second sample, the Nd Judd-Ofelt error is estimated to be +/- 15 %. The line strengths of magnetic dipole transitions S_{MD} are small compared to the electric dipole contributions and have been neglected here. The high Ω_2 value, which reflects the hypersensitive nature of the $^4G_{5/2}+^2G_{7/2}$ band (Fig. 3-4 (a)) in Nd:KPB, is noteworthy and could be advantageous for certain laser transitions. Comparable values for Judd-Ofelt intensity parameters Ω_t (t= 2, 4, 6) of the Nd:KPC crystal are reported to be in the range Ω_2 = 5.3 - 13.3 x 10^{-20} cm^2, Ω_4 = 5.6 - 13.1 x 10^{-20} cm^2, Ω_6 = 4.7 - 8.0 x 10^{-20} cm^2 ([Jen02], [Tka02b], [Nos02]).

Table 3-2(a). *Calculated line strengths S of induced electric dipole (ED) and of magnetic dipole (MD) transitions, spontaneous emission rates A^{ED} and A^{MD}, radiative branching ratios $\beta^{rad,\ calc}$ and radiative lifetimes τ^{rad} for relevant (laser) transitions in a Nd:KPB crystal. The electric dipole quantities were calculated with the following Judd-0felt intensity parameters Ω_2= 15.70, Ω_4= 6.25, Ω_6= 2.96 [x10^{-20} cm^2] and n=2.16.*

Transition (J→J')	**λ (μm)**	**S^{ED} (x10^{-20}cm^2)**	**S^{MD} (x10^{-20}cm^2)**	**A^{ED} (s^{-1})**	**A^{MD} (s^{-1})**	**$\beta^{rad,\ calc}$**	**τ^{rad} (ms)**
$^4F_{3/2}\rightarrow{}^4I_{15/2}$	1.85	0.09	0.00	25.9	0.0	0.003	
$^4F_{3/2}\rightarrow{}^4I_{13/2}$	1.35	0.62	0.00	483.7	0.0	0.061	0.126
$^4F_{3/2}\rightarrow{}^4I_{11/2}$	1.07	1.92	0.00	3030.8	0.0	0.383	
$^4F_{3/2}\rightarrow{}^4I_{9/2}$	0.89	1.60	0.00	4365.0	0.0	0.552	
$^4F_{5/2}\rightarrow{}^4F_{3/2}$	9.87	1.58	0.34	2.1	0.4	0.000	
$^4F_{5/2}\rightarrow{}^4I_{15/2}$	1.56	0.68	0.00	230.4	0.0	0.023	
$^4F_{5/2}\rightarrow{}^4I_{13/2}$	1.19	2.32	0.00	1765.3	0.0	0.178	0.101
$^4F_{5/2}\rightarrow{}^4I_{11/2}$	0.97	1.16	0.00	1652.4	0.0	0.167	
$^4F_{5/2}\rightarrow{}^4I_{9/2}$	0.82	2.67	0.00	6242.1	0.0	0.631	
$^2H_{9/2}\rightarrow{}^4F_{5/2}$	55.56	0.31	0.00	0.0	0.0	0.000	
$^2H_{9/2}\rightarrow{}^4F_{3/2}$	8.38	0.15	0.00	0.2	0.0	0.000	
$^2H_{9/2}\rightarrow{}^4I_{15/2}$	1.52	1.55	0.00	341.0	0.0	0.195	0.572
$^2H_{9/2}\rightarrow{}^4I_{13/2}$	1.17	0.99	0.00	480.6	0.0	0.275	
$^2H_{9/2}\rightarrow{}^4I_{11/2}$	0.95	0.12	0.01	107.5	5.7	0.065	
$^2H_{9/2}\rightarrow{}^4I_{9/2}$	0.81	0.54	0.02	785.1	27.7	0.465	

Using these Ω_t values, radiative transition probabilities from the $^4F_{3/2}$, $^4F_{5/2}$ and $^2H_{9/2}$ states are calculated using the method developed by Judd and Ofelt (section 1.2.2.1). The line strengths S of induced electric dipole (ED) and of magnetic dipole (MD) transitions, the spontaneous emission rates A^{ED} and A^{MD}, the radiative branching ratios $\beta^{rad, calc}$, and the radiative lifetimes τ_J^{rad} of level J are presented in Table 3-2(a). The reduced matrix elements were taken from Kaminskii [Kam96]. In this calculation the magnetic dipole contributions are included for completeness, although their influence is quite small, by using the line strengths S_{MD} from Nostrand [Nos00]. Results stated in this Table will be further used in the following sections e.g. in order to determine quantum efficiencies with the calculated radiative lifetimes.

Table 3-2(b). *Calculated line strengths S of induced electric dipole (ED) and of magnetic dipole (MD) transitions, spontaneous emission rates A^{ED} and A^{MD}, radiative branching ratios $\beta^{rad, calc}$ and radiative lifetimes τ^{rad} for relevant (laser) transitions in a Nd:RPB crystal. The electric dipole quantities were calculated with the following Judd-0felt intensity parameters Ω_2= 0.41, Ω_4= 9.32, Ω_6= 2.56 [x10^{-20} cm^2] and n=2.08.*

Transition (J→J')	**λ (μm)**	**S^{ED} (x10^{-20}cm^2)**	**S^{MD} (x10^{-20}cm^2)**	**A^{ED} (s^{-1})**	**A^{MD} (s^{-1})**	**$\beta^{rad, calc}$**	**τ^{rad} (ms)**
$^4F_{3/2}\rightarrow{}^4I_{15/2}$	1.85	0.07	0.00	19.4	0.0	0.002	0.115
$^4F_{3/2}\rightarrow{}^4I_{13/2}$	1.35	0.53	0.00	362.9	0.0	0.042	
$^4F_{3/2}\rightarrow{}^4I_{11/2}$	1.07	2.11	0.00	2881.2	0.0	0.332	
$^4F_{3/2}\rightarrow{}^4I_{9/2}$	0.89	2.28	0.00	5405.1	0.0	0.624	
$^4F_{5/2}\rightarrow{}^4F_{3/2}$	9.87	0.52	0.34	0.6	0.4	0.000	0.095
$^4F_{5/2}\rightarrow{}^4I_{15/2}$	1.56	0.59	0.00	172.8	0.0	0.016	
$^4F_{5/2}\rightarrow{}^4I_{13/2}$	1.19	2.71	0.00	1790.9	0.0	0.170	
$^4F_{5/2}\rightarrow{}^4I_{11/2}$	0.97	1.66	0.00	2054.0	0.0	0.195	
$^4F_{5/2}\rightarrow{}^4I_{9/2}$	0.82	3.23	0.00	6536.2	0.0	0.619	
$^2H_{9/2}\rightarrow{}^4F_{5/2}$	55.56	0.31	0.00	0.0	0.0	0.000	0.887
$^2H_{9/2}\rightarrow{}^4F_{3/2}$	8.38	0.19	0.00	0.2	0.0	0.000	
$^2H_{9/2}\rightarrow{}^4I_{15/2}$	1.52	2.17	0.00	414.1	0.0	0.367	
$^2H_{9/2}\rightarrow{}^4I_{13/2}$	1.17	0.37	0.00	155.5	0.0	0.138	
$^2H_{9/2}\rightarrow{}^4I_{11/2}$	0.95	0.07	0.01	53.1	5.1	0.052	
$^2H_{9/2}\rightarrow{}^4I_{9/2}$	0.81	0.37	0.02	474.9	24.8	0.443	

The Judd-Ofelt parameters of the Rb analog Nd:RPB were calculated by suitably averaging the polarized spectra in the spectral range 430 nm -1000 nm (see Fig. 3-4(b)) to be:

$$\begin{aligned} \Omega_2 &= 0.41 \times 10^{-20}\ \mathrm{cm}^2 \\ \Omega_4 &= 9.3 \times 10^{-20}\ \mathrm{cm}^2 \\ \Omega_6 &= 2.6 \times 10^{-20}\ \mathrm{cm}^2 \end{aligned} \qquad (3\text{-}2)$$

The transition probabilities are listed in Table 3-2(b). The significantly smaller Ω_2 value compared to that of Nd:KPB is a consequence of the different crystal structures of these two materials (see hypersensitivity in section 1.2.2.1). It might be that the site, where the neodymium ion is incorporated (assumed to be 8-fold coordinated) is of higher symmetry in RPB than the existing sites in KPB (section 2.1.2), and therefore, the dipolar component is in the case of KPB stronger.

3.2.1.2 Emission, Branching Ratios, and Quantum Efficiencies

The (blackbody corrected) emission spectra of a Nd:KPB crystal and a Nd:RPB crystal shown in Figure 3-5 were obtained as described in section 2.2.3. The high emission rate of transitions originating from the $^4F_{5/2}+^2H_{9/2}$ level relative to the $^4F_{3/2}$ level demonstrates the greatly reduced nonradiative multiphonon decay rate of the bromide crystals versus the chloride analog crystals [Nos01] arising from the lower phonon energies.[8] This made laser action at these new wavelengths promising. The emission cross sections σ_{em} (Fig. 3-5) and the radiative branching ratios $\beta^{rad,\ meas}$ (Tab. 3-3) have been determined as described in section 1.2.2.2.

The weak emission band around 1.56 μm (section 3.6, Fig. 3-28) was observed due to the $^4F_{5/2}\rightarrow{}^4I_{15/2}$ transition (Fig. 3-3), although the intensity was not absolutely calibrated to the other emission peaks. For comparison, the measured radiative branching ratios $\beta^{rad,\ meas}$ determined from the emission spectra of Nd:MPB (M=Rb,K) and the calculated radiative branching ratios $\beta^{rad,\ calc}$ are given in Table 3-3. Here, the calculated branching ratios $\beta^{rad,\ calc}$ are taken from the Judd-Ofelt calculations (Tab. 3-2) assuming statistically-distributed populations for the combined $^4F_{5/2}+^2H_{9/2}$ level. Magnetic dipole contributions are very small and do not play a role in the branching ratios. Differences in the measured and calculated branching ratios might be due to suspected anomalies in thermal occupation of strong versus weak Stark transitions causing a breakdown of the assumption of equally occupied levels in

[8] Emission from the $^4F_{5/2}+^2H_{9/2}$ was observed in other neodymium-doped low-phonon energy hosts (e.g. KPC, $LaCl_3$, La_2S_3 [Lei81]), but usually of lower efficiency.

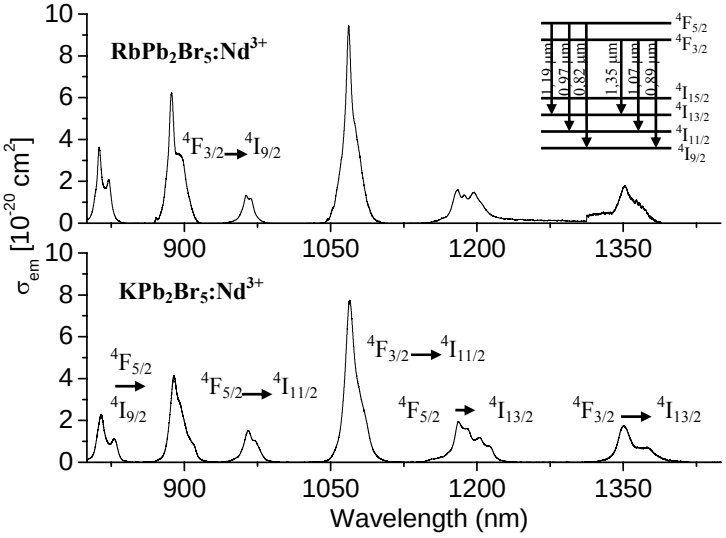

Fig. 3-5. *Blackbody corrected room temperature unpolarized emission spectra obtained by excitation of the $^4F_{7/2}$ level of Nd^{3+} doped MPb_2Br_5 (M=Rb, K) crystals. Compared to the $KPb_2Cl_5:Nd^{3+}$ [Nos01], the more intense fluorescence from the $^4F_{5/2}$ level (=$^4F_{5/2}$+ $^2H_{9/2}$ level) due to the low multiphonon decay rate is encouraging for achieving laser activity at new wavelengths.*

the JO calculation (section 1.2.2.1).

With the assumption that the radiative quantum efficiency for the $^4F_{3/2}$ level is ~ 1, and that the radiative rate between the $^4F_{5/2}$+ $^2H_{9/2}$ and $^4F_{3/2}$ levels is negligible, the radiative quantum efficiency of the $^4F_{5/2}$ level is given by [Nos01]:

$$\eta_{^4F_{5/2}} = \frac{1}{\phi_{^4F_{3/2}} / \phi_{^4F_{5/2}} + 1} \tag{3-3}$$

where $\phi_{^4F_{3/2}} / \phi_{^4F_{5/2}}$ is the ratio of the emission rates. The radiative emission rate ϕ_J of level J is calculated with the blackbody calibrated emission spectrum I(λ), with the assumption of rapid nonradiative decay to the $^4F_{5/2}$+ $^2H_{9/2}$ level from the pumped $^4F_{7/2}$ level:

$$\phi_J = \sum_{J'} \int_{J \to J'} \frac{I(\lambda)}{hc/\lambda} d\lambda \tag{3-4}$$

With an emission rate ratio of $\phi_{^4F_{3/2}} / \phi_{^4F_{5/2}}$ = 1.02 for Nd:KPB and $\phi_{^4F_{3/2}} / \phi_{^4F_{5/2}}$ = 0.42 for Nd:RPB the quantum efficiency $\eta_{^4F_{5/2}}$ is determined to be 0.49 and 0.71, respectively. These are considerably higher values compared to the value of 0.013 reported for Nd:KPC [Nos01], again due to the lower phonon energies of the bromides. Note, that the blackbody calibrated spectrum differs from that of Figure 3-5, where e.g. two different radiative lifetimes were used to calculate the cross sections.

Table 3-3. *Radiative branching ratios for the $F_{5/2}+^2H_{9/2}$ level and the $^4F_{3/2}$ level in Nd^{3+}-doped MPb_2Br_5 (M=Rb, K) crystals. The measured branching ratios $\beta^{rad,\ meas}$ were determined from the emission spectra of Nd:MPB (M=Rb, K). The calculated branching ratios $\beta^{rad,\ calc}$ were taken from the Judd-Ofelt calculations (Table 3-2) assuming statistically-distributed populations in the case of the combined $^4F_{5/2}+^2H_{9/2}$ levels, and are designated in parantheses.*

Transition J→J'	**λ (μm)**	**$\beta^{rad,\ meas}$, ($\beta^{rad,\ calc}$)**	
		$Nd:KPb_2Br_5$	**$Nd:RbPb_2Br_5$**
$^4F_{3/2}\rightarrow{}^4I_{15/2}$	1.85	N/A*, (0.003)	N/A*, (0.002)
$^4F_{3/2}\rightarrow{}^4I_{13/2}$	1.35	0.059, (0.061)	0.045, (0.042)
$^4F_{3/2}\rightarrow{}^4I_{11/2}$	1.07	0.453, (0.383)	0.404, (0.332)
$^4F_{3/2}\rightarrow{}^4I_{9/2}$	0.89	0.486, (0.552)	0.549, (0.624)
$(^4F_{5/2}+^2H_{9/2})\rightarrow{}^4I_{15/2}$	1.56	N/A*, (0.062)	N/A*, (0.069)
$(^4F_{5/2}+^2H_{9/2})\rightarrow{}^4I_{13/2}$	1.19	0.207, (0.200)	0.180, (0.165)
$(^4F_{5/2}+^2H_{9/2})\rightarrow{}^4I_{11/2}$	0.97	0.200, (0.144)	0.140, (0.173)
$(^4F_{5/2}+^2H_{9/2})\rightarrow{}^4I_{9/2}$	0.82	0.531, (0.593)	0.612, (0.593)

*N/A= not available, measured $\beta^{rad,\ meas}$ values are corrected by accounting for the calculated $^4F_{3/2}\rightarrow{}^4I_{15/2}$ and $(^4F_{5/2}+^2H_{9/2})\rightarrow{}^4I_{15/2}$ $\beta^{rad,\ calc}$ quantities.

3.2.1.3 Emission Lifetime and Quantum Efficiencies

It is expected that MPB (M= Rb, K) host crystals exhibit much longer lifetimes for the $^4F_{5/2}+^2H_{9/2}$ level of Nd^{3+}, compared to the lifetime of 3.4 μs [Nos01] reported for $Nd:KPb_2Cl_5$, since multiphonon decay competes less effectively with the radiative decay due to the lower phonon energies. Figure 3-6 shows the fluorescence decays from the combined $^4F_{5/2}+^2H_{9/2}$ level and from the $^4F_{3/2}$ level of Nd^{3+}-doped MPB (M=Rb, K), measured as decribed in section 2.2.5.

Exponential fits of the lifetimes are deduced, as listed in Table 3-4. For direct comparison the decay times of a Nd:KPC sample measured in the same experimetal setup are included. Indeed, as expected the lifetimes of the $^4F_{5/2}+^2H_{9/2}$ level of the bromide samples are much longer compared with the chloride sample. Despite the different site symmetry/crystal structure the lifetimes of the $^4F_{5/2}+^2H_{9/2}$ level in Nd:KPB and Nd:RPB are almost the same. The influence of the phonon energy on the multiphonon decay rate is due to similar maximum values approximately the same (section 3-1).

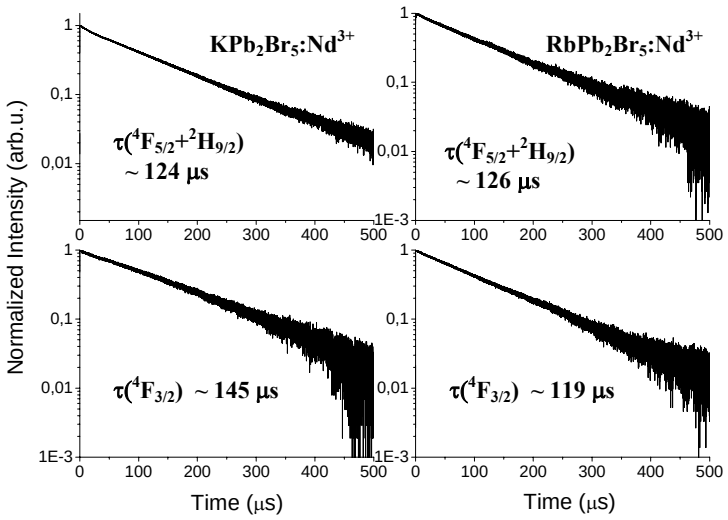

Fig. 3-6. *Fluorescence decay measurements from the combined $^4F_{5/2}+\ ^2H_{9/2}$ level and the $^4F_{3/2}$ level of $MPb_2Br_5:Nd^{3+}$ (M=Rb, K) by direct excitation of each investigated level yield an exponential decay lifetime of ~ 0.12 ms ($^4F_{5/2}+\ ^2H_{9/2}$).*

A comparison of the measured lifetimes τ^{meas} and the radiative lifetimes τ^{rad} of the Judd-Ofelt calculation is also given in Tab. 3-4. Here, the radiative lifetime τ^{rad} of the combined $^4F_{5/2}+\ ^2H_{9/2}$ level is determined from the Judd-Ofelt calculated radiative lifetimes of each level (Tab. 3-2), and assuming statistically-distributed populations. The Boltzmann population of individual crystal field levels was not considered since the state-to-state radiative rates are not known. The measured and calculated values for the $^4F_{3/2}$ level agree, while the difference between τ^{meas} and τ^{rad} for the $^4F_{5/2}+^2H_{9/2}$ combined emitting level is likely due to the partial influence of nonradiative decay or the simplification stated in the following. Note, that the radiative lifetimes were calculated assuming the high statistical limit for the $^4F_{5/2}+^2H_{9/2}$

Table 3-4*. Measured decay times τ^{meas} and calculated radiative lifetimes τ^{rad} of the $^4F_{5/2}+^2H_{9/2}$ level and the $^4F_{3/2}$ level of $MPb_2Br_5:Nd^{3+}$ (M=K, Rb). For comparison the decay times of $KPb_2Cl_5:Nd^{3+}$ measured in the same experimental setup are shown. The longer lifetimes of the $^4F_{5/2}+^2H_{9/2}$ level of the bromide samples compared to the chloride sample are due to the even lower multiphonon decay rate.*

Energy level	**τ^{meas} (μs), (τ^{rad} (μs))**		
	$Nd:KPb_2Br_5$	**$Nd:RbPb_2Br_5$**	**$Nd:KPb_2Cl_5$**
$^4F_{3/2}$	145 (126)	119 (115)	255
$^4F_{5/2}+^2H_{9/2}$	124 (208)	126 (214)	2

populations[9]. Taking account of the finite temperature yields a slightly shorter $^4F_{5/2}+^2H_{9/2}$ radiative lifetime of ~ 150 μs, based on the crystal field assignments for the individual levels (section 3.4) leading to even higher cross sections for these transitions. The high temperature limit for the $^4F_{5/2}+^2H_{9/2}$ populations was chosen since it reveals similar quantum efficiencies calculated from emission and absorption as shown in the following.

The radiative quantum efficiency for the combined $^4F_{5/2}+^2H_{9/2}$ level is determined by using:

$$\eta_{eff}^{rad} = \frac{\tau^{meas}}{\tau^{rad}}. \qquad (1\text{-}8)$$

From the data in Table 3-4 this gives 0.60 for Nd:KPB and 0.59 for Nd:RPB which are similar to the values of 0.49 and 0.71, respectively, determined from the emission spectra (eqn. 3-3 in section 3.2.1.2, together with Fig. 3-5).

3.2.2 Tb^{3+}-Doped KPb_2Br_5 Crystals

The Tb^{3+} ion was doped into the bromide host in order to explore the long wavelength region (Fig. 3-7) with this low-phonon energy crystal.

3.2.2.1 Absorption and Radiative Transition Probabilities

The absorption spectrum of Tb:KPB (Fig. 3-8) was measured with the Perkin Elmer Lambda 9 UV/VIS/NIR spectrophotometer and the Perkin Elmer 983 Infrared spectrophotometer (section 2.2.2). The spectrum evidences the possibility of direct pumping of long-wavelength transitions (Fig. 3-7) like the 8 μm transition with a 3 μm Er:YAG laser, or the 10 μm transition with a tunable Co:MgF_2 laser. The absorption bands around 3 μm and 4.5 μm are probably overlapped by CO_2 and water absorption features. The spectrum also shows the influence of e.g. NH_4^+, NH_3, and water peaks described in section 2.1.1 as well as the long tail originating from the band edge at the shorter wavelengths.

As for Nd:KPB in section 3.2.1.1 the Judd-Ofelt intensity parameters Ω_t are calculated for two different Tb:KPB samples using the measured absorption spectra after subtracting first the magnetic dipole contributions from the integrated absorption cross section (section 1.2.2.1).

[9] The fractional occupation number X of the electronic levels in the high temperature limit is defined in terms of the degeneracy g of the levels, e.g. for the $^4F_{5/2}$ level and $^2H_{9/2}$ level: $X(^4F_{5/2})= g(^4F_{5/2})/(g(^4F_{5/2})+g(^2H_{9/2}))$ and $X(^2H_{9/2})= g(^2H_{9/2})/(g(^4F_{5/2})+g(^2H_{9/2}))$, while in the case of the finite temperature the fractional thermal Boltzmann population needs to be included (Appendix B, eqn. B-1).

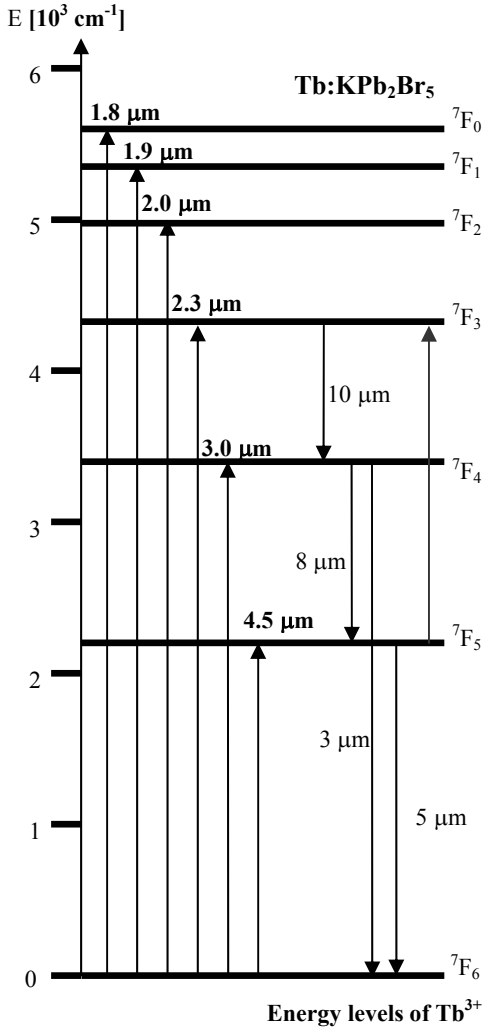

Fig. 3-7*. Energy level diagram of Tb:KPB displays the possibility of direct pumping of long-wavelength transitions.*

The averaged Ω_t values for Tb:KPB are given in the following:

$$\Omega_2 = 3.7 \times 10^{-20}\ cm^2\ (+/-\ 20\%)$$
$$\Omega_4 = 4.3 \times 10^{-20}\ cm^2\ (+/-\ 40\%) \qquad (3\text{-}5)$$
$$\Omega_6 = 0.72 \times 10^{-20}\ cm^2\ (+/-\ 10\%)$$

These Judd-Ofelt parameter values of Tb:KPB are smaller than the Ω_t values for Nd:KPB of 15.7 $x10^{-20}$ cm^2, 6.3 $x10^{-20}$ cm^2, and 3.0 $x10^{-20}$ cm^2, as it is the case for e.g. Nd- versus Tb-doped Y_2O_3 crystals [Kru66].

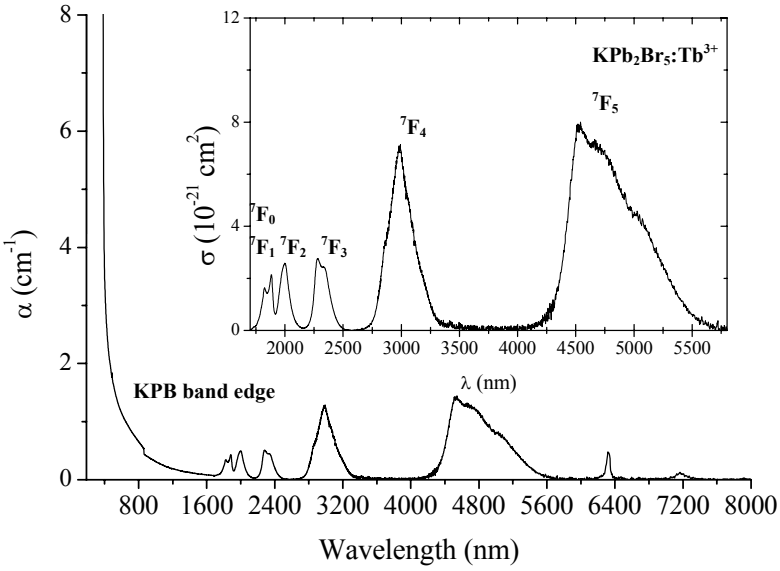

Fig. 3-8. *Unpolarized absorption spectrum of $KPb_2Br_5:Tb^{3+}$.*

Note, that the overlapping influence of CO_2 and water absorption features was not extracted. Previously reported JO intensity parameters for Tb:KPC in the literature are $\Omega_2 =$ 2.9-3.7 x10^{-20} cm^2, $\Omega_4 =$ 1.0-2.2 x10^{-20} cm^2, $\Omega_6 =$ 0.13-0.24 x10^{-20} cm^2 [But02].

The radiative transition probabilities for the MWIR and LWIR transitions shown in Table 3-5 were calculated using the squared reduced matrix elements from Kaminskii [Kam96]. The line strengths of magnetic dipole transitions were calculated by using the equations given in Carnall et al. [Car77]. A radiative lifetime of 12.5 ms for the $^7F_4$ level and 34.6 ms for the $^7F_5$ level was determined.

Table 3-5. *Calculated line strengths S of induced electric dipole (ED) transitions and of magnetic dipole (MD) transitions, spontaneous emission rates A^{ED} and A^{MD}, radiative branching ratios $\beta^{rad,\ calc}$ and radiative lifetimes τ^{rad} for relevant (laser) transitions in a Tb:KPB crystal. These results were calculated with the following Judd-Ofelt intensity parameters: Ω_2= 3.67, Ω_4= 4.29, Ω_6= 0.72 [x10^{-20} cm^2] and n=2.10.*

Transition (J→J')	**λ (μm)**	**S^{ED} (x10^{-20}cm^2)**	**S^{MD} (x10^{-20}cm^2)**	**A^{ED} (s^{-1})**	**A^{MD} (s^{-1})**	**$\beta^{rad,\ calc}$**	**τ^{rad} (ms)**
$^7F_5\rightarrow{}^7F_6$	4.9	4.72	0.73	25.2	3.7	1	34.6
$^7F_4\rightarrow{}^7F_5$	7.9	2.35	1.12	3.6	1.7	0.066	12.5
$^7F_4\rightarrow{}^7F_6$	3.0	2.72	0.00	74.9	0.0	0.934	
$^7F_3\rightarrow{}^7F_4$	10.3	1.93	1.23	1.8	1.1	0.025	
$^7F_3\rightarrow{}^7F_5$	4.5	1.86	0.00	20.5	0.0	0.178	8.7
$^7F_3\rightarrow{}^7F_6$	2.3	1.19	0.00	92.0	0.0	0.797	

3.2.2.2 Emission

The (blackbody corrected) room temperature emission spectra (Fig. 3-9) of Tb:KPB were measured by pumping into the $^7F_2$ level using the setup described in section 2.2.3. The emission cross section was determined with the Fuechtbauer Ladenburg equation given in section 1.2.2.1 (Eqn. 1-9), using the branching ratios and radiative lifetimes calculated from the Ω_t values (Tab. 3-5).

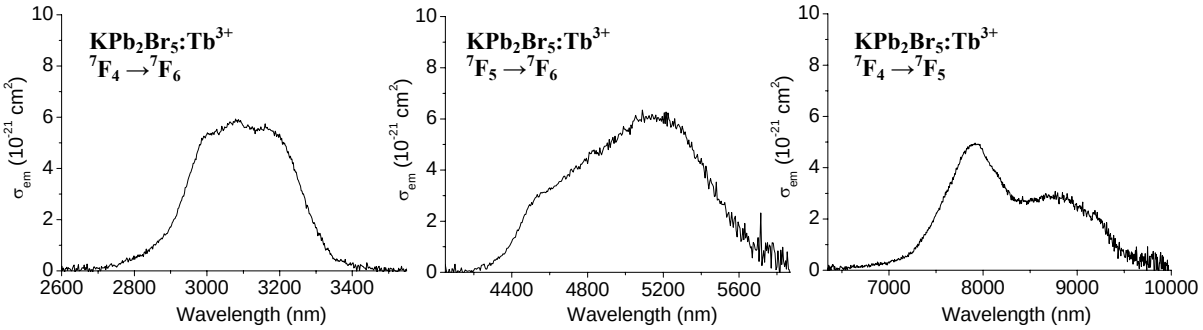

Fig. 3-9. *Room temperature LWIR emission spectra at ~ 3 μm, 5 μm, and 8 μm resulting from the $^7F_5$ and $^7F_4$ level in Tb^{3+}-doped KPb_2Br_5 crystals.*

The maximum peak intensity emission wavelength of 7.9 μm for the $^7F_4 \rightarrow {}^7F_5$ transition is longer than in Tb^{3+}-doped chalcogenide glass fibers with a maximum at 7.5 μm [Sha01]. The peak emission cross sections for the 3 μm, 5 μm, and 8 μm emission in this crystal are $6 \cdot 10^{-21} cm^2$, $6 \cdot 10^{-21} cm^2$ and $5 \cdot 10^{-21} cm^2$, respectively. For comparison the cross sections for a chalcogenide fiber, consisting of germanium arsenic gallium selenide glass (GAGSe), are: $1.37 \cdot 10^{-20} cm^2$ (3 μm), $1.05 \cdot 10^{-20} cm^2$ (5 μm) and $0.83 \cdot 10^{-20} cm^2$ (8 μm), respectively [Sha01]. In Tb^{3+}-doped gallium lanthanum sulfide glass a value of $9 \cdot 10^{-21} cm^2$ (5 μm) has been determined [Sch99]. The observation of a broadband 8 μm emission spectrum – which was for the first time to the author`s knowledge measured in low-phonon energy, moisture-resistant host crystals - is encouraging for the goal of a tunable LWIR-laser for remote sensing in the vibrational fingerprint region. The double peak structure for the 8 μm transition could possibly be due to different state-to-state radiative rates.

The $^7F_5 \rightarrow {}^7F_3$ transition in Tb:KPB (Fig. 3-7) could be advantageous for the 8 μm emission because of repopulation of the upper laser level (and depopulation of the lower laser level) via an Auger upconversion process [Pay92]. Although 10 μm emission from the $^7F_3 \rightarrow {}^7F_4$ transition was expected in this crystal, since at least 4-5 phonons span the energy difference between the two levels, luminescence has not been detected thus far by exciting at 2 μm. This fact might be due to a low signal/noise ratio of the measurements. Measurements at low

temperatures (as partly presented in section 3.3) give further information about the potential 10 µm emitting level and will help to determine the band structure of the measured emission bands as well as their linewidths.

3.2.2.3 Emission Lifetime and Quantum Efficiencies

The decay times (Figure 3-10) were measured as described in section 2.2.5 by pumping into the $^7F_2$ level. Here, the resulting fluorescence was captured by a liquid nitrogen cooled HgCdTe-detector (and pre-amplifier). It was assumed that fast non-radiative decay connect the upper levels e.g. the $^7F_2$ and $^7F_3$ level. The emission lifetimes for the $^7F_4$- and $^7F_5$- level were taken for six different Tb^{3+}-doped KPB samples of different concentrations and grown under different conditions (Tab. 3-6). Samples 3 and 4 were grown and synthesized under a Br_2 overpressure to prevent out-diffusion of Br_2, while for the other samples an argon over-atmospheric pressure of ~ 310 mbar was used to prevent the out-diffusion of bromine during synthesis. Also, the purity of the starting material varied: at Fisk University the purity of the

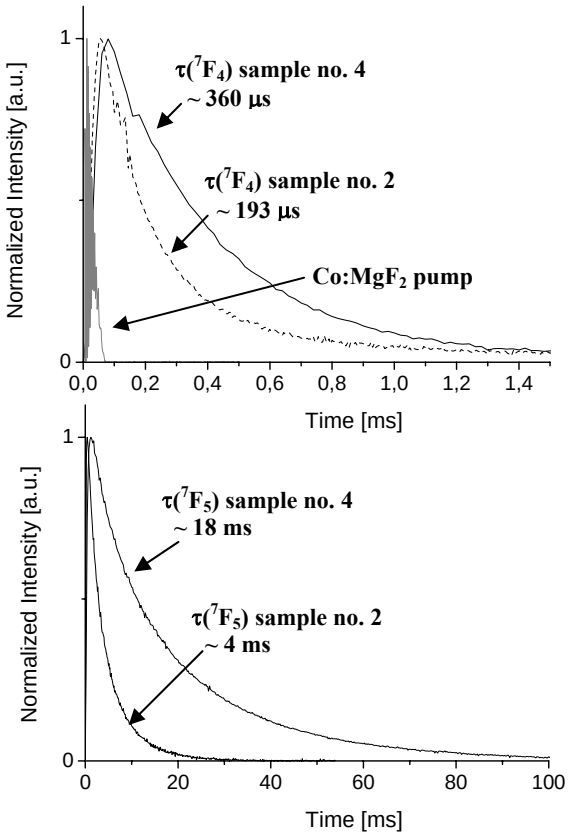

Fig. 3-10. *Long lifetimes of the $^7F_5$ level and the $^7F_4$ level were measured for different samples of $KPb_2Br_5:Tb^{3+}$ which is encouraging for proving laser activity in these crystals in the LWIR region.*

$PbBr_2$ used was 5N while KBr was used in two different purity grades, 99.98% and 5N for different runs. At EIC the purity used was 99.99% for $TbBr_3$ and 5N for initial KBr and $PbBr_2$ (>7N after zone refining process).[10]

The lifetimes for the different samples vary from 3 ms to 22 ms for the $^7F_5$ level and from 0.19 ms to 0.42 ms for the $^7F_4$ level which is likely due to concentration dependent effects and/or impurities in the crystals. The emission lifetime of the $^7F_4$ level is shorter than the lifetime of the $^7F_5$ level because of the smaller energy gap. It is believed that the measured 8 μm emission is not of thermal origin; note that the 3 μm and 8 μm emissions, both originating from the $^7F_4$ level, have the same lifetime. For comparison lifetime values of 12 μs for a Tb^{3+}:GAGSe Glass fiber [Sha02], 900 μs for a Tb^{3+}:$CsCdBr_3$ crystal [But02], and 2.3 ms for a Tb^{3+}:AgBr/I fiber [But02] for the $^7F_4$ level have been reported. The lifetime of the $^7F_5$ level in a Tb:KPC sample was measured to be 1.4 ms in the same experimental setup while similar values in the range of 3-4 ms for this Tb^{3+}-doped chloride host were found in the literature ([But02], [Nos00]).

With the ratio of the measured lifetimes and the radiative lifetimes quantum efficiencies for the different Tb:KPB samples were determined. They range from 0.02 to 0.03 for the $^7F_4$ level and 0.08 to 0.64 for the $^7F_5$ level due to the difference in the measured lifetimes (Tab. 3-6). These quantum efficiencies are higher than the values reported for a Tb^{3+}-doped KPC crystal (0.04 for the $^7F_5$ level [But02]). The long emission lifetimes of the $^7F_5$ level (several ms) and the $^7F_4$ level (several 100 μs range) is encouraging for realizing laser action in these crystals in the LWIR region.

Table 3-6. *Decay times of the $^7F_4$ level and the $^7F_5$ level of $KPb_2Br_5:Tb^{3+}$ for six different samples of different Tb^{3+} concentration.*

	τ^{meas} [ms]					
Tb^{3+}:KPb_2Br_5 sample number	**no. 1**	**no. 2**	**no. 3**	**no. 4**	**no. 5**	**no. 6**
Tb^{3+} dopant concentration [x10^{20} cm^{-3}]	~2.20*	1.80	0.98	0.98	0.68	~0.35*
Energy level						
$^7F_5$ (5 μm)	2.8	4.2	13	18	22	22
$^7F_4$ (3 μm)	0.21	0.19	0.32	0.36	0.38	0.38
$^7F_4$ (8 μm)	0.21	0.19	0.33	0.36	0.42	0.41

*The Tb^{3+} dopant concentration for sample no. 1 and no. 6 is determined by comparative absorption while the other samples are measured directly by the inductively coupled plasma-mass spectrometry technique.

[10] It is not exactly clear which purity grade is related to which sample.

The variation in lifetime among the samples is likely due to energy transfer e.g. to defects and impurities – this possibility is supported by the correlation between the magnitude of the $^7F_4$ and $^7F_5$ lifetimes. Moreover, it appears as if the defect/impurity quenching is partly mediated by the Tb concentration (via the migration-enhanced energy-transfer mechanism). It is believed that the lower doped samples were probably also the samples of higher purity.

3.2.3 Eu^{3+}-Doped KPb_2Br_5 Crystals: Absorption and Radiative Transition Probabilities

This crystal system was investigated since it has potential (laser) transitions in the LWIR e.g. the $^7F_6 \rightarrow {}^7F_5$ transition (Fig. 3-11) which can be pumped directly with a Co:MgF_2 laser at 2.1 μm. As will be shown below calculations indicate high line strenghts for the LWIR transitions. Europium is similar to Terbium (no disturbing energy levels above, section 1.1, Fig. 1-2), but with the difference that the energy gap becomes smaller towards the ground state which could in principle lead to better depopulation of lower (laser) levels due to the higher nonradiative rates. The energy gaps are roughly estimated to be quite similar.

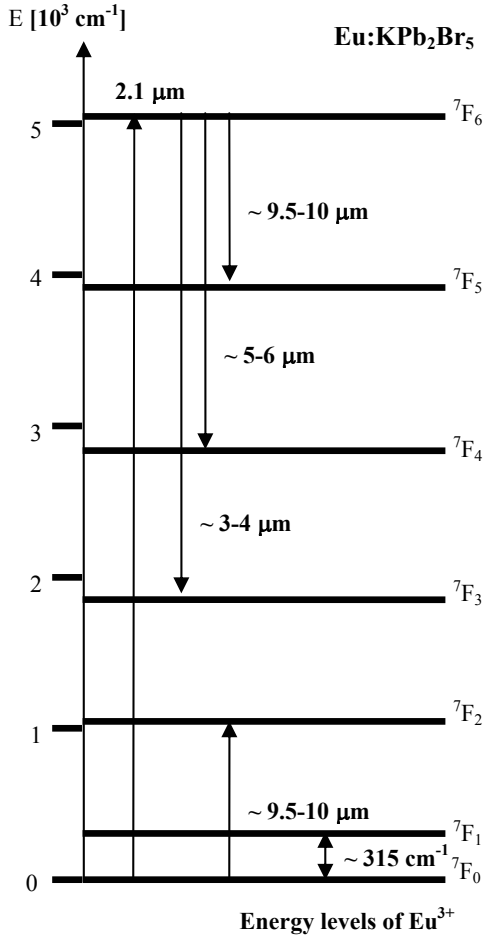

Fig. 3-11. *Energy level diagram of Eu^{3+} shows potential laser transitions in the LWIR region e.g. resulting from the $^7F_6$ level which can be directly pumped with a Co:MgF_2 laser. Similar energy gaps can lead to emission quenching.*

The room temperature absorption spectrum (Fig. 3-12) of Eu:KPb_2Br_5 was measured with a FTIR spectrophotometer (section 2.2.2). It shows transitions resulting from the $^7F_0$ and the thermally populated $^7F_1$ level into higher lying energy levels. The cross section is calculated by taking into account an Eu wt% measured to be 0.85% which gives a concentration of $1.895 \cdot 10^{20}$ cm^{-3}. As mentioned in section 2.1 the valency of incorporated ions is not distinguishable and so this concentration could be due to the presence of Eu^{3+} and Eu^{2+}.

The absorption spectrum (Fig. 3-12) shows reasonable absorption strength from the ground

state into the $^7F_6$ level for pumping the $^7F_6 \rightarrow {}^7F_5$ transition. Transitions like e.g. $^7F_0 \rightarrow {}^7F_3$ are clearly observed even though they are theoretically forbidden (see selection rules in section 1.2.2.1, Tab. 1-1). Indeed, Ofelt has calculated [Ofe62] that transitions from J=0 to J=odd should be - if present - weak. These transitions were previously observed in other materials such as Eu^{3+}:$LaCl_3$ ($^7F_0 \rightarrow {}^7F_5$) [Sha63] and EuF_3 ($^7F_0 \rightarrow {}^7F_3$, $^7F_5$) [Cas67]. Their presence is probably due to crystal field mixing. The sharp feature at ~ 6.3 μm is probably due to NH_3 or water. Not shown in the spectrum is the $^7F_0 \rightarrow {}^7F_1$ transition which is most probably overlapped by the IR cut-off and also forbidden by the selection rules.

The following host-dependent Judd-Ofelt intensity parameters Ω_t (t= 2, 4, 6) (section 1.2.2.1) of Eu:KPB were determined by using the absorption bands (Fig. 3-12) in the spectral range ~ 2-12 μm resulting from the $^7F_0$ as well as the thermally populated $^7F_1$ level by taking the averaged Boltzmann population into account (section 1.2.2.1 and Appendix B, eqn. B-1):

$$\begin{aligned} \Omega_2 &= 14.8 \times 10^{-20}\ \mathrm{cm}^2 \\ \Omega_4 &= 8.5 \times 10^{-20}\ \mathrm{cm}^2 \\ \Omega_6 &= 2.9 \times 10^{-20}\ \mathrm{cm}^2 \end{aligned} \qquad (3\text{-}7)$$

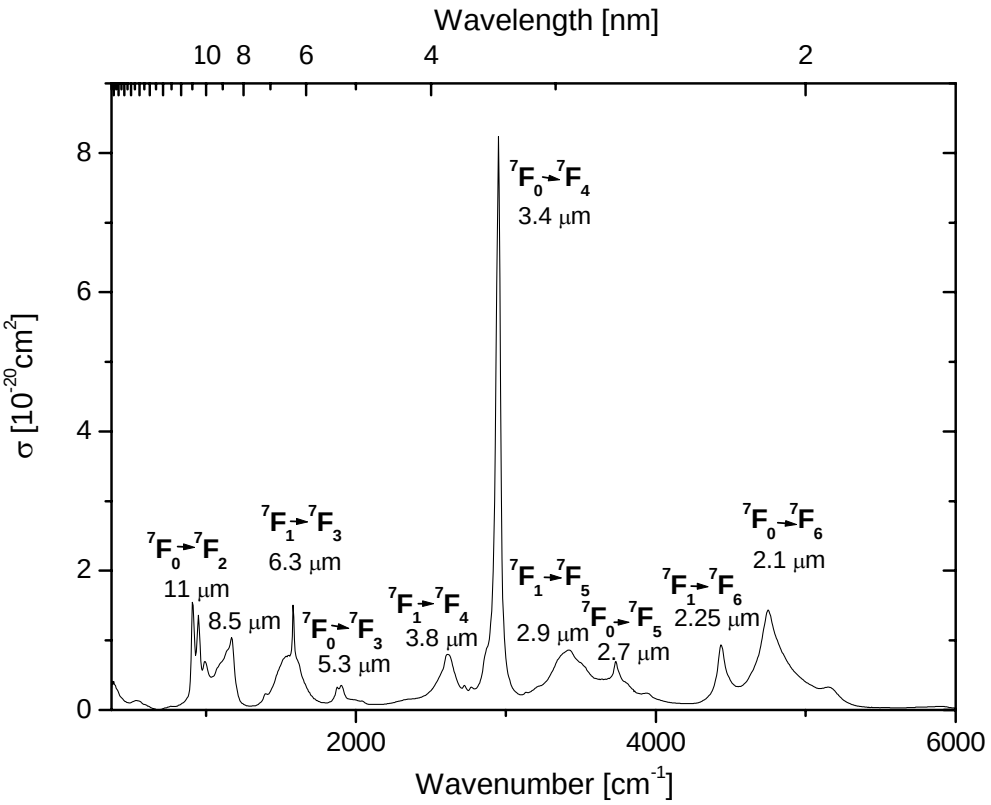

Fig. 3-12. *Absorption spectrum of Eu:KPb_2Br_5 shows transitions resulting from the $^7F_0$ and the thermally populated $^7F_1$ level into higher lying levels. There might be a band missing at ~ 700 cm^{-1} ($^7F_1$-$^7F_2$) due to a grating change during the measurement or this band is overlapped by lattice vibrations.*

The Judd-Ofelt root mean square error (Appendix B) is estimated to be 16 %. This error is mainly due to the influence of the observed but theoretically forbidden transitions leading to differences in the measured and calculated signal strengths. Also, the use of Gaussian curve approximations (as used for Tb^{3+} in the previous section) to separate the overlapped bands resulting from the $^7F_0$ and $^7F_1$ level can improve the results.

Table 3-7. *Judd-Ofelt intensity parameters for different rare earth ions in KPB*

RE^{3+} (in KPB)	**Ω_2**	**Ω_4**	**Ω_6**
	[10^{-20} cm^2]		
Nd^{3+}	15.7	6.3	3.0
Eu^{3+}	14.8	8.5	2.9
Tb^{3+}	3.7	4.3	0.7

The calculated Judd Ofelt intensity parameters are quite high if compared with Nd^{3+} and Tb^{3+} in KPB (section 3.2.1 and 3.2.2). Table 3-7 summarizes the different Judd-Ofelt parameter for Nd^{3+}, Eu^{3+}, and Tb^{3+} in KPB. The Eu^{3+} values are in the range of Nd^{3+} in KPB. Low temperature absorption measurements are suggested in order to eliminate the thermal population of the $^7F_1$ level and to be able to focus on absorption bands due to $^7F_0$-^7F_J (J=1,...,6) transitions. This could lead to lower intensity parameters than in Nd^{3+}, which is expected if one assumes the same tendency like in oxides such as Y_2O_3 [Kru66] or $YAlO_3$ [Kam96].

The radiative transition probabilities for the LWIR emission transitions were calculated using the reduced matrix elements from Kaminskii [Kam96]. The transition probabilities are illustrated in Table 3-8 for transitions mainly resulting from the $^7F_6$ level. The line strengths of magnetic dipole transitions were calculated by using the equations given in Carnall et al. [Car77]. Radiative lifetimes calculated for the ^7F_J levels (J=1,...,6) to be several ms increase with smaller J (e.g. $^7F_6$: 4 ms, $^7F_5$: 8 ms, $^7F_4$: 16 ms, $^7F_3$: 55 ms). So does the nonradiative decay rate due to the smaller energy spacing to lower J numbers. Self-termination could still be present.

No emission from the $^7F_6$ level has been observed which is most likely due to the similar energy spacing of the $^7F_6$-$^7F_5$ and $^7F_0$-$^7F_2$ transition (Fig. 3-11, Tab. 3-8) leading to quenching by cross relaxation. Also, multiphonon decay might be quite influencial since possible strong Stark level splitting could lead to a small energy gap (<< 900 cm^{-1} gap for $^7F_6$-$^7F_5$ in Eu^{3+} in $LaCl_3$ [Sha63]). The lack of fluorescence even at low temperature might also indicate the influence of quenching processes enhanced by the high concentration of the samples. From the study of the Tb-doped samples it is known that the lower doped samples have the longest lifetimes and that it appears as if the defect/impurity quenching is partly mediated by the RE concentration via the migration-enhanced energy-transfer mechanism. Thus, it is believed that

a high purity, lower doped sample might be the better choice for future growth runs. In addition to that the lower doped samples show less scattering (section 2.1.1).

Table 3-8. *Calculated line strengths S of induced electric dipole (ED) transitions and of magnetic dipole (MD) transitions, spontaneous emission rates A^{ED} and A^{MD}, radiative branching ratios $\beta^{rad,\ calc}$ and radiative lifetimes τ^{rad} for relevant (laser) transitions in an Eu:KPB crystal. These results are calculated with the following Judd-0felt intensity parameters: Ω_2=14.84, Ω_4= 8.52, Ω_6=2.92 [x10^{-20} cm^2] and n=2.10.*

Transition (J→J')	λ* (μm)	S^{ED} (x10^{-20}cm^2)	S^{MD} (x10^{-20}cm^2)	A^{ED} (s^{-1})	A^{MD} (s^{-1})	$\beta^{rad, calc}$	τ^{rad} (ms)
$^7F_6 \rightarrow {}^7F_5$	9.1	13.59	0.73	9.7	0.5	0.043	
$^7F_6 \rightarrow {}^7F_4$	4.8	6.44	0	31.8	0	0.134	
$^7F_6 \rightarrow {}^7F_3$	3.2	3.17	0	50.4	0	0.211	4.2
$^7F_6 \rightarrow {}^7F_2$	2.5	1.78	0	60.7	0	0.255	
$^7F_6 \rightarrow {}^7F_1$	2.2	1.10	0	57.1	0	0.240	
$^7F_6 \rightarrow {}^7F_0$	2.0	0.42	0	28.1	0	0.118	
$^7F_2 \rightarrow {}^7F_0$	10.0	2.04	0	2.8	0	0.857	303

*Note that the transition wavelengths are for the present time taken from the literature [Kam96] until Stark levels of Eu^{3+} in this particular crystal host are determined. They do not necessarily match the wavlength of this particular crystal system (e.g. the $^7F_6 \rightarrow {}^7F_0$ transition is ~ 2.1 μm and the $^7F_6 \rightarrow {}^7F_5$ transition is expected to be closer to 10 μm).

3.2.4 Low Multiphonon Decay Rates for Bromide Crystals

The multiphonon decay rate W^{MP} of KPB was estimated by use of the "energy gap law" (Eqn. 1-13, section 1.2.3) where the host dependent phenomenological constants C and χ for KPB are assumed to be χ_{KPB} = 1.70·10^{-2} cm and C= 3.47·10^8 s^{-1}. The value of χ is approximately proportional to the reciprocal phonon energy $\hbar\omega_{eff}$ ([Lay77], section 1.2.3) and so the value of KPB was determined by estimating the ratio of the phonon energies of KPC and KPB (Section 3.1) with the χ-value of KPC (χ_{KPC} = 1.156·10^{-2} cm [Nos01]) as follows:

$$\chi_{KPB} \approx \frac{\hbar\omega_{eff,KPC}}{\hbar\omega_{eff,KPB}} \cdot \chi_{KPC} = \frac{203cm^{-1}}{138cm^{-1}} \cdot 1.156 \cdot 10^{-2} cm \qquad (3\text{-}6)$$

This impact of the maximum phonon energy on the χ_{KPC} and χ_{KPB} values is consistent with the relationship observed for the $LaBr_3$, $LaCl_3$ pair as well (by using χ values from [Kam96]). The C value was determined by a best fit to the measured values of the nonradiative rate which is described later in this section. With an energy gap ΔE of 974 cm^{-1} between the $^4F_{3/2}$ and the $^4F_{5/2}$ level in Nd:KPB and an effective phonon energy $\hbar\omega_{eff}$ =138 cm^{-1} the number of phonons p= ΔE/ $\hbar\omega_{eff}$ ≅ 7 and thus a multiphonon decay rate of ~ 3.7·10^3 s^{-1} is obtained. As expected this is a lower value than in the KPb_2Cl_5 host (10^5 s^{-1} [Tka02b], [Nos01]).

Figure 3-13 shows the multiphonon decay rate versus the energy gap for different host lattices determined by the energy gap law. The fitting parameters C and χ as well as the phonon energies (in the following in brackets) for $LaBr_3$ (175 cm^{-1}), KPC (203 cm^{-1}), $LaCl_3$ (260 cm^{-1}), and $LiYF_4$ (560 cm^{-1}) are taken from Nostrand et al. [Nos01] and Kaminskii [Kam96] in order to produce the plotted lines. While the solid line for KPb_2Br_5 is calculated by using the phonon energy and fitting parameters as mentioned above, the dashed line is calculated by using a different phonon energy (160 cm^{-1}) and fitting parameter C ($3.27 \cdot 10^9$ s^{-1}) which will be explained in section 3.3. Note, that the difference in W^{MP} of e.g. LaX_3 versus KPX (X= Br, Cl) reflects also differences in the host dependent multiphonon fit parameters including different electron-phonon coupling in addition to the different phonon energies.[11]
The measured values of the nonradiative rate in rare earth-doped KPB are indicated with triangles in Fig. 3-13.

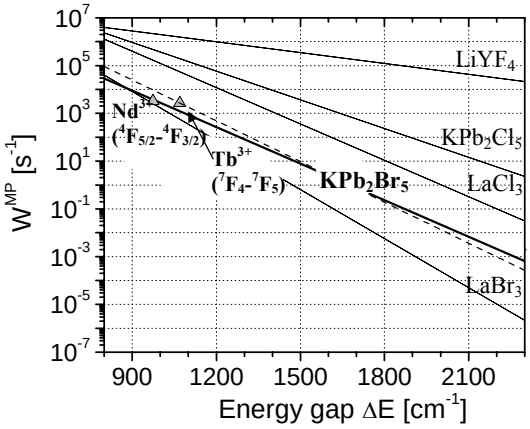

Fig. 3-13. *Multiphonon decay rate versus energy gap between two levels for different host lattices at room temperature (after energy gap law). The measured value of the nonradiative rate in rare earth-doped KPB is calculated by subtracting the radiative rate $1/\tau^{rad}$ from the measured rate $1/\tau^{meas}$. The values are indicated with triangles. While the solid line for KPb_2Br_5 is calculated by using the phonon energy and fitting parameters as described in this section, the dashed line is calculated by using different values determined from temperature dependent lifetime fits (section 3.3). Parameters for the other host matrices are taken from the literature [Kam96], [Nos01].*

[11] If the nonradiative rate is displayed versus the "effective order" $p=\Delta E/\hbar\omega_{eff}$ at low temperature and, thus, is quasi normalized in order to account for the spread in the phonon density of states, the influence of different electron-phonon coupling becomes more obvious. In addition, lines of crystals with the same structure and nearly identical crystal fields overlap as can be seen for $LaBr_3$ and $LaCl_3$ in the literature ([Ris67], [Ris68]).

They are calculated by subtracting the radiative rate $1/\tau^{rad}$ from the measured rate $1/\tau^{meas}$ and neglecting the concentration dependent component of the decay. Here, the radiative lifetimes of 208 µs for Nd^{3+} (Section 3.2.1.3) and 12.5 ms for Tb^{3+} (Section 3.2.2.1), and the measured lifetimes of 124 µs for Nd^{3+} (Section 3.2.1.3) and 360 µs for Tb^{3+} (Section 3.2.2.3), were used. The smallest energy spacing of the $^4F_{5/2}$+$^2H_{9/2}$ - $^4F_{3/2}$ transition in Nd^{3+}-doped KPB was measured to be 974 cm^{-1} due to low temperature Stark level measurements of these levels (section 3.4). The energy gap of the $^7F_4$- $^7F_5$ transition in Tb^{3+}-doped KPB was determined to be 1070 cm^{-1} by taking the maximum emission wavelength of the 8 µm emission spectrum (Fig. 3-9, section 3.2.2.2). Eu^{3+}-doped MPB was not included due to the lack of measured lifetimes.

The results presented in this section 3.2 show that the nonradiative decay competes less effectively compared with the radiative rate in these rare earth-doped bromide host crystals. Higher quantum yields have been achieved in the bromide host crystals compared to the KPC crystals for transitions from the $^4F_{5/2}$ level into the ^4I_J levels in Nd:KPB and Nd:RPB as well as for the LWIR emission from the ^7F levels in Tb:KPB, which demonstrates the greatly reduced nonradiative multiphonon decay rate of the bromide versus the chloride [Nos01] (arising from the lower phonon energies). Thus, laser action for transitions from the $^4F_{5/2}$ level into the ^4I_J levels in Nd:KPB is achieved (section 3.5) and is promising for LWIR transitions like e.g. in Tb:KPB.

3.3 Temperature Dependent Quenching in Tb^{3+}-Doped KPb_2Br_5 Crystals

The temperature dependency of emission lifetimes of many excited states can result from different sources. It can arise from a changing population distribution among Stark levels having different radiative and nonradiative decay probabilities, multiphonon emission, or (phonon assisted) vibronic transitions. Energy migration and energy transfer arising from ion-ion interactions can play a role in the case of higher dopant concentrations.

Variations in the total radiative decay rate due to changing level populations tend to be small [Web73]. Vibronic transitions are generally most intense for ions near the beginning or end of the $4f^n$ series [Web72]. In the following study of Tb^{3+} in KPB it is considered that both effects have a negligible small effect to the lifetimes studied. This study was mainly performed in order to determine the temperature dependent effect of multiphonon quenching and its important parameters as well as to identify if there are other possible quenching mechanisms involved. Note, that only rough estimates on the influence of the concentration dependent quenching mechanisms were made, since necessary parameters to calculate the rates were not

known (section 1.2.3). In the context of this study e.g. emission resulting from the $^7F_3$ level, the potential initial level of 10 μm emission, will also be presented.

3.3.1 Emission Lifetimes of the $^7F_4$ and $^7F_5$ Level Versus Temperature

Temperature dependent lifetime measurements of Tb^{3+}-doped KPb_2Br_5 were performed for two samples of different concentration and purity (Nc ~ $2.2x10^{20}$ cm^{-3} (sample no.1) and ~ $0.35x10^{20}$ cm^{-3} (sample no.6), Table 3-6, section 3.2.2.3). The emission liftimes of the $^7F_4$ level and $^7F_5$ level were determined in the temperature range ~ 30 K – 300 K as described in section 2.2.5 by exciting the $^7F_2$ level with a Co:MgF_2 laser tuned to 2.0 μm (Fig. 3-14).

Measured lifetimes and rates for sample no. 1 and sample no. 6 were detected at ~ 3 μm and ~ 5 μm (Fig. 3-14, 3-15 and 3-17; Measurements at 8 μm give similar results to the 3 μm emission lifetimes since they both originate from the same level). In addition calculated lifetime/rate fits are displayed. They are obtained by assuming that the total decay rate W_J of level J (J = $^7F_4$, $^7F_5$) obeys the relation (section 1.2.3):

$$W_J = A_J^{rad} + W_J^{MP}(T) + W_J^{c,imp} \qquad (3\text{-}7)$$

The $W_J^{c,imp}$ term stands here mainly for quenching caused by energy transfer to impurities and defects which is partly mediated by the Tb concentration. Remember, that in section 3.2.2.3 a variation in lifetime among six studied samples was found which is assumed to be likely due to this component. At this point this component is assumed to be temperature independent.

The multiphonon decay rate W^{MP} of KPB was estimated by use of the "energy gap law" (Eqn. 1-13, section 1.2.3), where ΔE= 1070 cm^{-1} (section 3.2.4), $h\nu_{eff} = \hbar\omega_{eff}$ = 160 cm^{-1} (best fit value), p = $\Delta E/\hbar\omega_{eff}$ = 6.7 for the $^7F_4$-$^7F_5$ gap was used. Here, the constants C and χ for this bromide host crystal were fitted to be χ_{KPB} = $1.70\cdot10^{-2}$ cm (section 3.2.4) and C= $3.27\cdot10^9$ s^{-1}. The estimated phonon energy of 160 cm^{-1} is consistent with the measured maximum phonon energy in the wing of the Raman spectrum (Fig. 3-16).

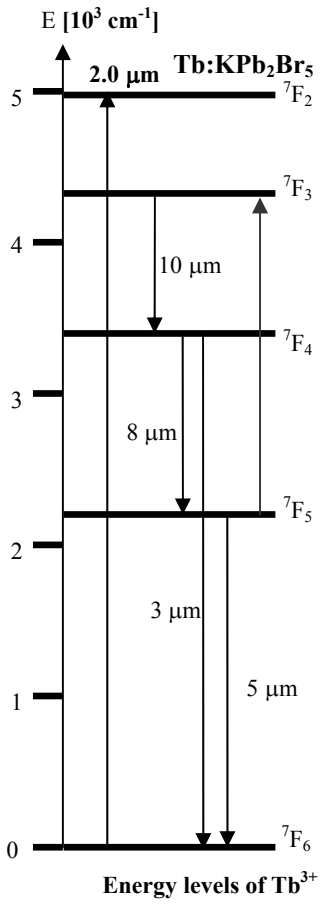

***Fig. 3-14**. Energy level diagram of Tb:KPB.*

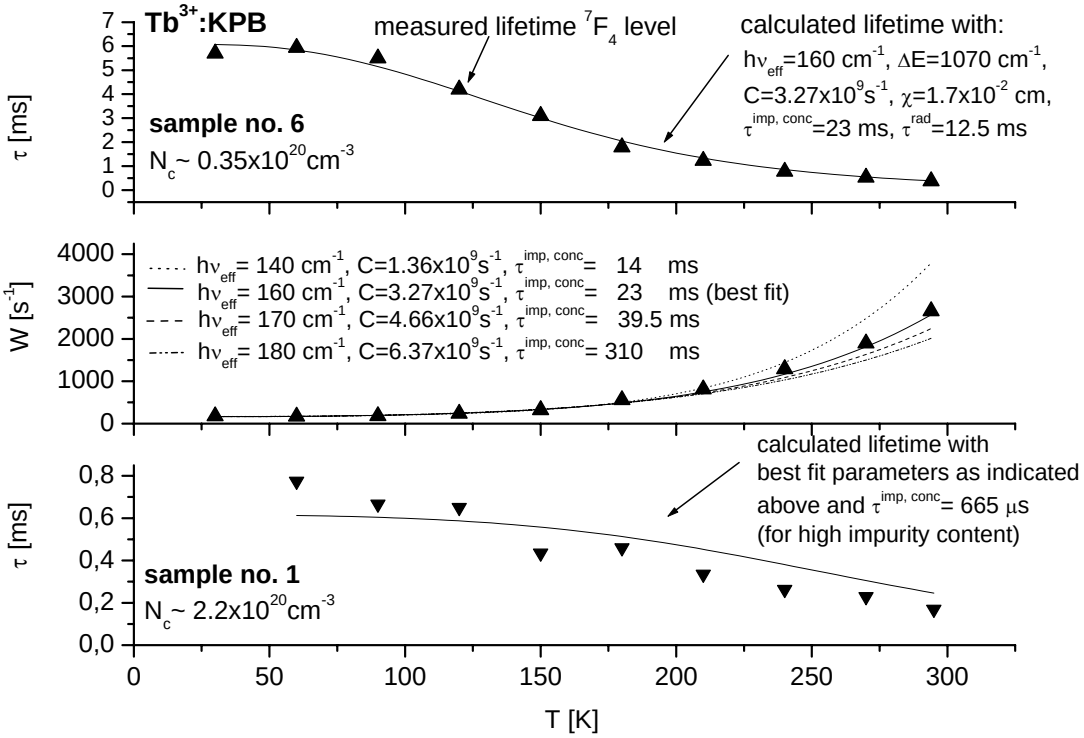

Fig. 3-15. *Measured (triangles) and calculated (lines) lifetimes versus temperature for the $^7F_4$ level in Tb:KPB for two different samples of different purity and concentration. The fit parameters were optimized by taking parameters (in the energy gap law) which compromise between a best fit of the lifetime as well as the rate of the $^7F_4$ level (top and middle graph) for the lower concentrated sample (no.6).*

Note, that the C value is determined by a best fit to the temperature dependent data of the lower concentrated, higher purity sample no. 6 (Figure 3-15). In order to find the best fit parameters for the $^7F_4$-$^7F_5$ gap it was compromised between a best fit of the lifetime as well as the rate. The measured and calculated emission lifetimes of the $^7F_4$ level seem to agree especially for the sample with higher purity and lower concentration (no. 6): 0.39 ms versus 0.38 ms at room temperature. Note, that the results of the fitting parameters C and $\hbar\omega_{eff}$ are different if compared with the values of the previous section. The multiphonon decay rate versus energy gap calculated with these parameters is displayed by the dashed line in Fig. 3-13 of section 3.2.4. This indicates that the assumption of fitting the data to a single value of the phonon energy can be a valid approximation for calculating the nonradiative rate as shown in previous studies ([Lay77], [Par67], [Lay75]). It also shows that taking the maximum peak value of the highest Raman energy phonon band (138 cm^{-1}) can be a first approximation for calculating the number of phonons 'p' involved in the process in order to determine the

nonradiative rates. However, if it is concluded from the best fit of the measured rate as well as the lifetime data, a maximum phonon energy value taken from the wing of the Raman spectrum is representation of the $\hbar\omega_{eff}$ (Fig. 3-16). The highest-energy phonons are usually considered to make the dominant contribution to multiphonon relaxation since they conserve energy in the lowest-order process ([Web73], [Ris68]).[12] From Fig. 3-15 $h\nu_{eff}$ =160 cm^{-1} has approximately an uncertainty of +/- 20 cm^{-1}. A comparison with other hosts shows that differences in the measured and theoretical values of the phonon energies are not unusal. In $LaBr_3$ vibronic sidebands were observed indicating a cutoff in the phonon spectrum at ~ 175 cm^{-1} [Ric63], while a theoretical fit done by Riseberg *et al.* ([Ris68], [Ris67]) for RE^{3+}:$LaBr_3$ corresponds to an emission of 155 cm^{-1} phonons.

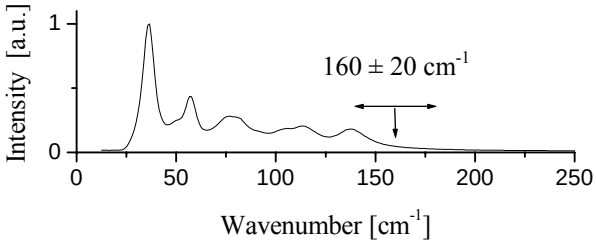

Fig. 3-16. *Raman scattering spectrum of a KPb_2Br_5 crystal (section 3.1).*

Table 3-9. *Radiative rate A^{rad}, concentration dependent rate $W_J^{c,imp}$, and multiphonon decay rate W^{MP} for the $^7F_4$ and $^7F_5$ level.*

Energy level	A^{rad} [s^{-1}] (Judd-Ofelt)	$W_J^{c,imp}$ [s^{-1}]	W^{MP} [s^{-1}] (@ 294 K)
$^7F_4$	80.0	1250 (no.1), 43.5 (no. 6)*	2445
$^7F_5$	28.9	167 (no.1), 5.6 (no.6)*,**	0.124

*accuracy depends also on A^{rad} and ΔE uncertainty
**determined by fitting to the values of the measured lifetimes at lower temperature

A comparison of the radiative rate, the concentration dependent rate, and the multiphonon decay rate is shown in Table 3-9. It can be seen, that the multiphonon decay rate from the $^7F_4$ level is still quite influencial compared with the radiative decay rate determined from Judd-Ofelt calculation. Furthermore, the concentration dependent rate $W_J^{c,imp}$ - fitted to the measured curve - is quite different for sample no. 1 and sample no. 6. As mentioned above this difference is due to different concentrations of the Tb^{3+} ion as well as the energy transfer to impurities e.g. NH_4^+ (NH_4Br absorption at 3 μm, 5.8 μm and 7.2 μm [Poh32], [Rei21]), water (~ 3 μm and ~ 6 μm [Mcc78]), and NH_3 (e.g. 6.1 μm [Pug76]). The height of these impurity absorption peaks relative to the absorption peaks of the rare earth ion varied from

[12] Weber noticed in his oxide studies that equal or even better fits can also be obtained using larger numbers of lower energy phonons (although they necessitate higher order process), and concluded that their "rate is probably larger because they tend to be more numerous and/or more strongly coupled to rare earth "impurities"" [Web73]. So, other pathways are possible.

crystal to crystal. The ratio of e.g. 7.2 μm impurity absorption coefficients to the Tb peak absorption at ~4.5 μm ranges from 1:2 to 1:14 depending on the sample. The actual 7.2 μm absorption coefficient is in the range of ~ 0.1-0.2 cm^{-1} for both of the Tb^{3+}-doped samples.
The NH_3 concentration was estimated from the integrated absorption coefficient s= 5.6*10^{-18} cm/molecule for NH_3 near 6.1 μm [Pug76] by using:

$$N_c = \alpha \cdot \Delta\nu / s\,, \tag{3-8}$$

where α is the absorption coefficient and Δν the bandwidth (~16 cm^{-1}) of the impurity. The concentration is determined for sample no. 1 and sample no. 6 to be ~ 3x10^{18} cm^{-3} and ~1x10^{18} cm^{-3}, respectively. The cross section is in the order of 3.5x10^{-19} cm^2. For comparison the 4.5 μm Tb^{3+} absorption peak cross section is in the order of 6-9x10^{-21} cm^2. Note, that the peak wavelength in the absorption spectra is actually closer to 6.2-6.3 μm instead of 6.1 μm [Pug76], but for now it is assumed that this peak is due to NH_3 and not water.
The measured lifetimes of the $^7F_5$ level are displayed in Fig. 3-17. For the data of sample no. 1 appropriate filters were used to block unwanted wavelengths, while for sample no. 6 a monochromator tuned to 5 μm was used. For the fit to the measured lifetimes of the $^7F_5$ level the author used the best fit parameters as described above by changing the energy gap to ΔE= 1820 cm^{-1} which is deduced from the emission spectrum of the $^7F_5 \rightarrow {}^7F_6$ transition (section 3.2.2.2) and the number of phonons involved p= 11.4. For the emission resulting from the $^7F_5$ level the influence of multiphonon decay should be small even at room temperature since 11 phonons are involved in the $^7F_5 \rightarrow {}^7F_6$ transition (see calculated small W^{MP} in Table 3-9). With the approximations made above a fairly constant lifetime over temperature is expected for both samples. However, this is not the case especially for the higher concentrated, lower purity sample no. 1 (Figure 3-17(top)) where the measured lifetime varies a factor of ~ 2 in the temperature range 30-300 K.
For a detailed study of this behavior the simplification of the concentration dependent component not to be a function of T needs to be adjusted so that e.g. temperature dependent energy transfer mechanisms such as (phonon assisted) energy transfer ([Gan02], [Auz76], [Miy70]), energy migration etc. will be taken into account . Energy transfer from $^7F_5$-$^7F_6$ to $^7F_5$-$^7F_3$ could increase with higher temperature (Fig. 3-14). Also, energy transfer to impurities could increase with higher temperature due to better overlap of the Tb^{3+} and impurity bands. Studies of Quimby *et al.* [Qui03] support this aspect. They revealed a systematic difference in determining the radiative rate by subtracting the measured from the calculated lifetime and by measuring the temperature dependence of the lifetimes, and concluded that there are other

more dominant nonradiative processes involved for energy gaps > 2500 cm^{-1} (in this case) in rare earth-doped chalcogenide glass such as energy transfer to vibrational impurities OH and SH.

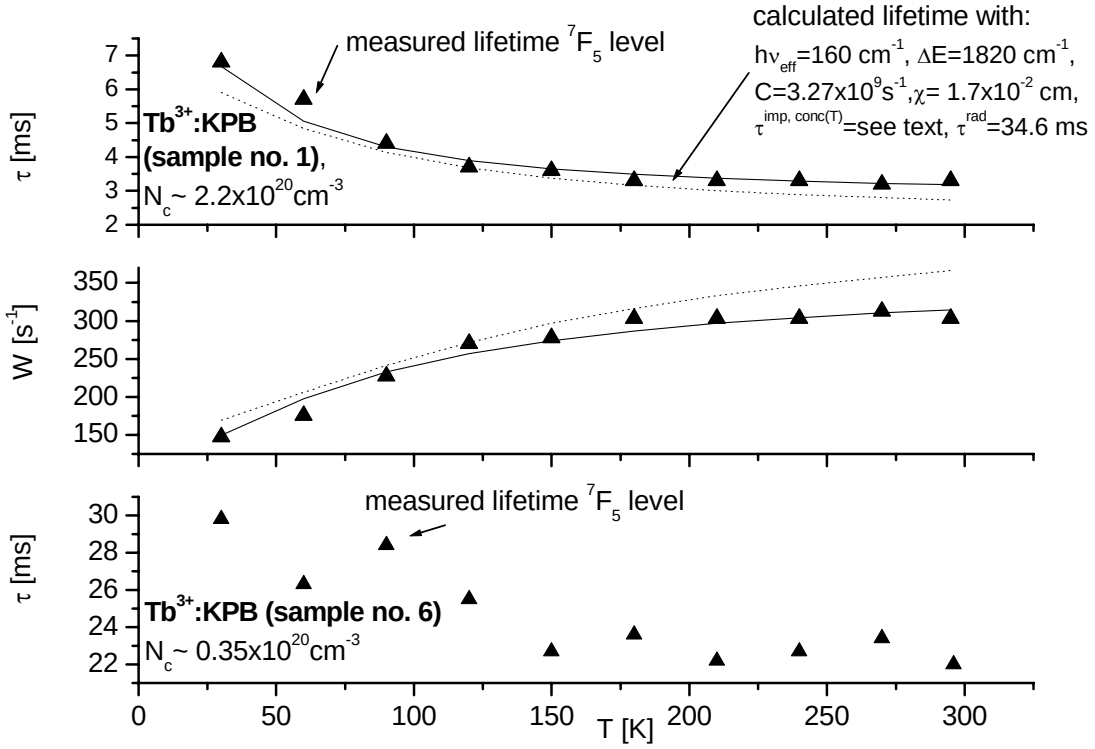

Fig. 3-17. *Measured (triangles) and calculated (lines) lifetimes (and rate) versus temperature for the $^7F_5$ level in Tb:KPB for two samples of different purity and concentration. Especially, the higher doped sample no. 6 (top and middle graph) shows a temperature dependency which is probably due to energy transfer to e.g. impurities as further described in the text. The influence of multiphonon decay is small, because ~ 11 phonons bridge the energy gap to the next lowest level. Here, the temperature dependency of the concentration dependent component was included in the fit (eqn. 3-9 and 3-10), where the dashed and solid line are calculated by assuming different concentration dependent rates.*

Figure 3-17 shows at this point a rough approach to fit the temperature dependent decay for the $^7F_5$ level. Here, the $W_J^{c,imp}$ term is assumed to be temperature dependent by simply assuming an exponential dependency as shown by the following equation:

$$W_J^{c,imp}(T) = (\tau_J^{LT})^{-1} + (\tau_J^{HT})^{-1} \cdot \exp(-E^{act}/kT) \tag{3-9}$$

where τ_J^{LT} and τ_J^{HT} are the low temperature and high temperature lifetimes, and E^{act} is the activation energy of the energy migration. The solid and the dotted line through the data of sample no. 1 in Figure 3-17 shows the fit determined by the following equation:

$$W_J = A_J^{rad} + W_J^{MP}(T) + W_J^{c,imp}(T) \tag{3-10}$$

The dotted line shows the fit assuming the measured lifetimes as the high and low temperature limit: τ_J^{LT} (6.8 ms), τ_J^{HT} (3.3 ms) and E^{act} (11.9 meV or rather ~ 96 cm^{-1}). A better fit was obtained by using the following values: τ_J^{LT} (9.8 ms), τ_J^{HT} (4.2 ms) and E^{act} (6.6 meV or rather ~ 53 cm^{-1}) displayed by the solid line.

Note, that this approach of the temperature dependent $W^{c,imp}$ term was not applied for the $^7F_4$ level. In this case, the multiphonon decay fit (Fig. 3-15) looks reasonable by taking a constant value for the concentration/impurity dependent rate for sample no. 6 where the influence of the term $W^{c,imp}$ is quite small if compared with the multiphonon decay rate (Table 3-9). For sample no. 1 this might need to be adjusted. Also, temperature dependency due to e.g. a changing population distribution among Stark levels might play a role.

3.3.2 Emission Intensities and Rise Time Versus Temperature

In addition to the emission lifetimes the intensities and the times where the fluorescence has its maximum peak intensity (in the following this time is called rise time) were measured versus temperature at 3 µm and at 5 µm. The intensity is expected to increase for transitions from the $^7F_4$ level with lower temperature due to less multiphonon decay, but in contrary the intensity decreases e.g. for sample no. 6 a factor of four. This could be due to narrower absorption lines with the consequence that the pump line absorption at 2 µm decreases.

Another possibility is that the $^7F_3$ level lifetime increases at lower temperatures and therefore,

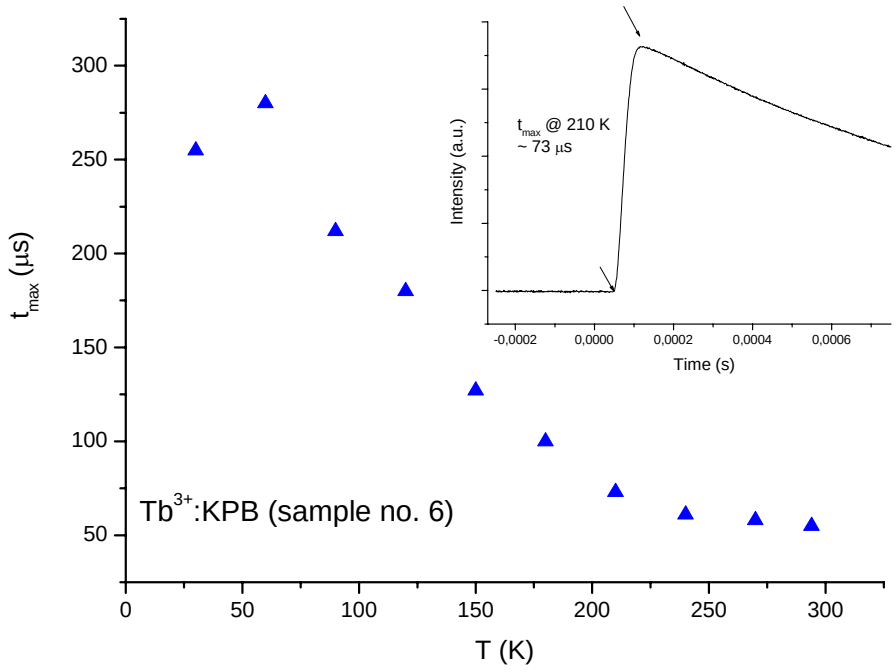

Fig. 3-18. *Measured rise times t_{max} versus temperature for the $^7F_4$ level in Tb:KPB sample no. 6.*

emission from the $^7F_3$ level is more feasible to occur. This would decrease the population of the $^7F_4$ level. This possibility is inconsistent with the fact that at higher temperature the energetic ovelap is better and energy transfer ($^7F_3$-$^7F_5$, $^7F_6$-$^7F_5$) is more likely to happen. The rise time measured for the $^7F_4$ level shows for sample no. 6 an increase to lower temperatures (Fig. 3-18) which is most probably due to an increase in the decay times of the $^7F_4$ level as well as the $^7F_3$ level filling the $^7F_4$ level. Here, the pumping level $^7F_2$ was assumed to rapidly decay into the $^7F_3$ level due to the smaller energy gap. An example for the rise time is shown for T= 210 K in the inset of Figure 3-18.

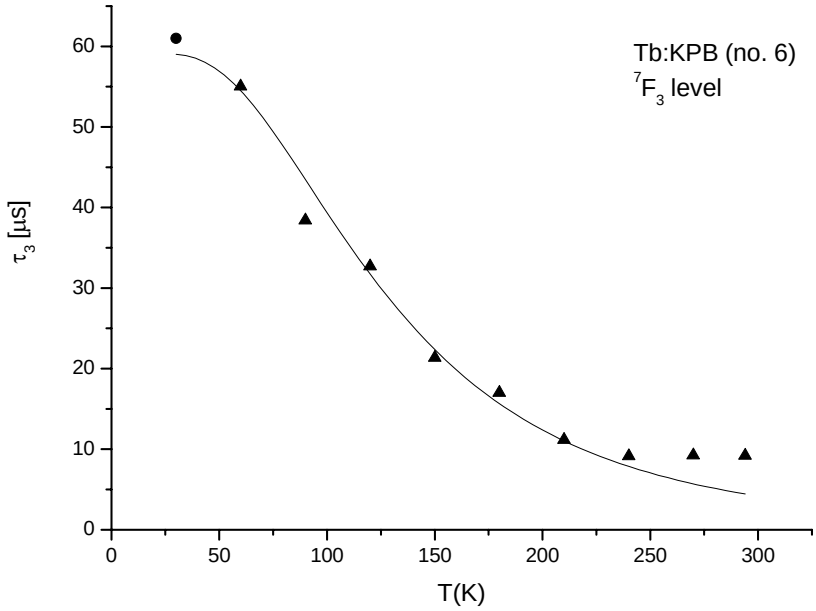

Fig. 3-19. *Calulated (triangles) and measured (circle) lifetime of the $^7F_3$ level. The calculated values were determined from the t^{max} values and the $^7F_4$ level lifetimes (Eqn. 3-11). The fit to these lifetime data (after Eqn. 1-13) gives an energy gap of ~730 cm^{-1} indicating a 4-5 phonon transition if $\hbar\omega_{eff}$ = 160 cm^{-1} is assumed.*

From the temperature dependent data measured for the $^7F_4$ level the lifetime of the $^7F_3$ level can be estimated for different temperatures. For the simplified case where the level $^7F_3$ decays directly to the fluorescing level $^7F_4$, the fluorescence will exhibit a maximum intensity at time t_{max} [Web73]:

$$t_{\max} = \frac{\ln(\tau_3 / \tau_4)}{1/\tau_4 - 1/\tau_3}, \tag{3-11}$$

where τ_3 and τ_4 are the lifetime decays of the $^7F_3$ and $^7F_4$ level. This transcendental equation assumes that the excitation pulse is much shorter than the τ_3 and τ_4 lifetimes, which was not the case (the excitation pulse was ~ 50 µs in length). Thus, 20 µs were subtracted from the

measured t_{max} values in Figure 3-18 to correct for this effect. In addition, it is assumed that there is no other process involved causing the change of the t_{max} values over temperature other than nonradiative decay. The decay times of the $^7F_3$ level values were determined to be in the range 55 µs (at ~ 60 K) and 9 µs (at ~300 K) as shown in Figure 3-19 (triangles). Emission lifetime measurements at 4.4 µm revealed an emission lifetime of 60 µs at low temperatures deduced by an exponential fit. In Figure 3-19 the calulated lifetime value at 30 K was exchanged by the measured 60 µs lifetime of the $^7F_3$ level (circle). The fit to these lifetime data (after eqn. 1-13) gives an energy gap of ~ 730 cm^{-1} indicating a 4-5 phonon transition if $\hbar\omega_{eff}$ = 160 cm^{-1}, χ_{KPB} = 1.70·10^{-2} cm and C= 3.27 ·10^9 s^{-1} is assumed. The gap is estimated to be in between 700 and 1000 cm^{-1} from measured absorption and emission spectra (section 3.2.2) at this point of this study. Room temperature absorption spectra give 670 cm^{-1} for the smallest gap, emission spectra reveal ~1000 cm^{-1}. In the literature 900 cm^{-1} was found for the smallest $^7F_3$-$^7F_4$ gap in Tb^{3+}:$LaBr_3$ and Tb^{3+}:$LaCl_3$ ([Jos72], [Wyb65]) and ~ 740 cm^{-1} in Tb^{3+}:YGAG [Jos77] determined from the Stark level splitting.

The rise time of the $^7F_5$ level also increases to lower temperatures, but will not be further discussed in this study. Temperature dependent measurements in other rare earth ions such as Nd^{3+} could be very useful since it offers different energy gaps (e.g. the $^4F_{7/2}$-$^4F_{5/2,}$ $^4F_{5/2}$-$^4F_{3/2}$ and $^4F_{3/2}$-$^4I_{11/2}$ gap). By measuring temperature dependent emission lifetimes for further transitions of different energy gap spacing in Nd^{3+} and other rare earth-doped KPB it could be exactly determined which portion of the measured non-radiative relaxation is truely due to multiphonon decay.

3.3.3 Emission from the $^7F_3$ Level

In order to determine if there is emission resulting from the $^7F_3$ level into the $^7F_5$ level (influencing the $^7F_5$-$^7F_6$ transition as mentioned above and revealing the possibility for 10 µm emission) emission spectra were measured (section 2.2.3) with two different box car time gate settings at low temperatures (Fig. 3-20) and room temperature. The 15 µs long time gate was set to ~ 75-90 µs and 2.8 ms after the trigger pulse in order to distinguish between the emissions resulting from the $^7F_3$ and $^7F_5$ level since the $^7F_5$ level emission lifetime is with several ms much longer than the lifetime expected for the $^7F_3$ level. The dashed line in Figure 3-20 shows emission from the $^7F_5$ level (2.8 ms delay) while the solid line displays a mixture of $^7F_3$ level and $^7F_5$ level emission (75 µs delay). The emission at the shorter wavelengths indicate emission resulting from the $^7F_3$ level. In the spectra taken it looks like there is emission even at room temperature (not shown) resulting from the $^7F_3$ level which is

encouraging in order to observe 10 μm emission resulting from this level ($^7F_3 \rightarrow {}^7F_4$ transition). So far, 10 μm emission was not observed by using a 9.8 μm LP Filter together with a HgCdTe Detector as a detection system which is probably due to a low signal-to-noise ratio since the emission at 4.4 μm was already very weak.

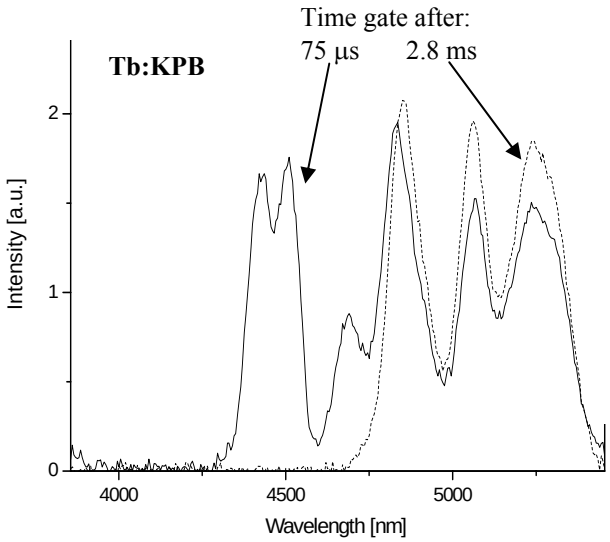

Fig. 3-20. *Uncorrected emission spectrum of Tb:KPB (sample no. 6) at T= 30K with two different time gate settings enables to distinguish between emissions from the $^7F_3$ and $^7F_5$ level. The dashed line shows the $^7F_5$ level emission while the solid line displays a mixture of $^7F_4$ and $^7F_5$ level emission. Please note that this spectrum is taken with an InSb detector and thus, the shape of the curve at the longer wavelength could very well be influenced by the detector cut-off.*

For further characterization low temperature spectroscopy is planned e.g. to determine the Stark levels in these crystals.

3.4 Low Temperature Spectroscopy of Nd^{3+}-Doped KPb_2Br_5 Crystals

This section discusses results mainly observed by low temperature spectroscopy. One main purpose of this study was the determination of Stark levels for Nd^{3+} in KPB (Fig. 3-3). These Stark levels were in particular used in following sections about optical pump-probe processes and upconversion e.g. to determine the transition wavelengths and transition probabilities of section 3.6 (Tab. 3-10). Note, that unpolarized spectra were taken due to the lack of orientated samples.

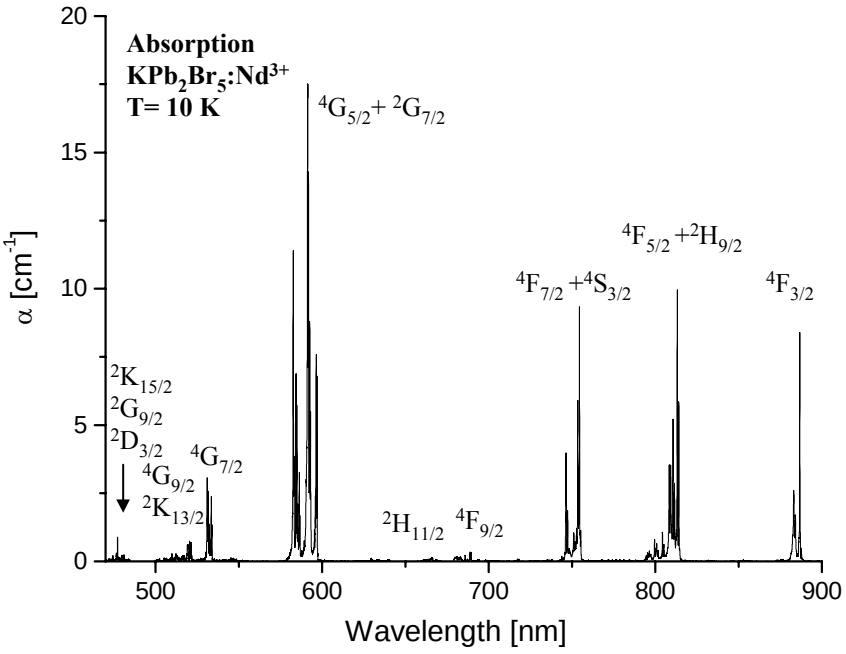

Fig. 3-21. *Absorption peaks of $KPb_2Br_5:Nd^{3+}$ in the wavelength region 470-900 nm at 10 K.*

Transmission measurements (section 2.2.2) were performed in the wavelength region 350-2700 nm at 10 K, 70 K and 300 K. An example is shown for the wavelength region 470-900 nm (Fig. 3-21) at 10 K. Emission measurements were performed in the region 400 nm – 2800 nm. Emission in the wavelength range 800 nm – 2800 nm was measured as described in section 2.2.3 by excitation with a Ti:Sapphire laser at 753 nm and 813 nm.

Using these spectra Stark level energies were determined (Appendix D). A comparison of 10 K and 70 K measurements were useful to identify additional peaks such as the so called hot bands. Excitation spectra were also taken in the wavelength region 250-850 nm for different emission wavelengths (422 nm, 465 nm, 591 nm, 601 nm and 813 nm) in order to identify Stark levels, but also to study the structure at the band edge (section 2.1.2) further. In the following, some observations made during these measurements are shortly described.

Exemplary, Figure 3-22 shows a more detailed view of the Stark level splitting of the $^4F_{5/2}$ and $^2H_{9/2}$ multiplet. The arrow marked Stark levels appear together with in a distance of 13 cm^{-1} laying second peaks. This double peak structure was observed for almost every multiplet in the absorption spectrum (taken with a spectral resolution of 0.08 nm). This could lead to the following assumptions:

One assumption was that the double peak structure is caused by the first two levels of the ground state multiplet being occupied, but emission measurements revealed that the first two Stark levels are actually 25 cm^{-1} apart (Appendix D). Also, the double peak structure was observed for some peaks in emission as well.

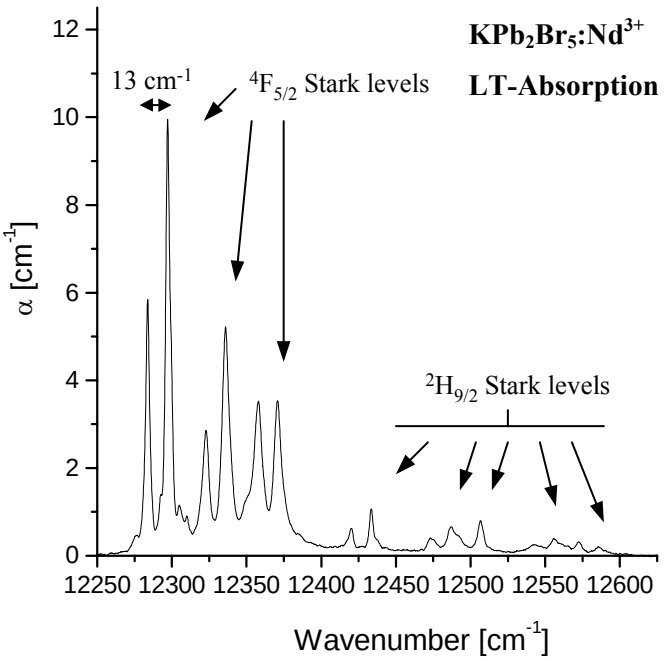

Fig. 3-22. *Stark level splitting of the $^4F_{5/2}$ multiplet and $^2H_{9/2}$ multiplet determined by low temperature transmission measurements.*

One reason could be that the double peak structure is related to two different lead sites in the host KPB where the Nd is incorporated. It was proposed for KPB that RE^{3+} ions substitute Pb^{2+} at two sites (section 2.1.2). The emission spectrum was measured by excitation in each peak of one double peak structure but the emission spectrum did not change. This could mean that there is energy transfer between ions of the two sites. This needs to be further investigated for more peaks. Furthermore, there might be different sites due to charge compensation and structural imperfections.

Further investigations are needed, also for a few peaks appearing in a distance of ~ 8 cm^{-1} from the Stark levels which are observed in emission and absorption as well. Also, phonons or pairs causing further peaks in the spectrum can not be excluded.

During the low temperature measurements emission originating from the $^4F_{7/2}$ + $^4S_{3/2}$ level by pumping at 753 nm was evident. Exemplary, emission at 890 nm for two excitation wavelengths is shown (Fig. 3-23). As can be seen the transition originating from the $^4F_{3/2}$ level into the $^4I_{9/2}$ level is overlapped by the transition from the $^4F_{7/2}$ + $^4S_{3/2}$ level into the $^4I_{11/2}$ level. Likewise, emission from the $^4F_{7/2}$ + $^4S_{3/2}$ level into the $^4I_{13/2}$ level at 1052 nm was observed. Upconversion spectra (section 3.7) possibly indicate emission from the $^4F_{7/2}$ + $^4S_{3/2}$ level even at room temperature.

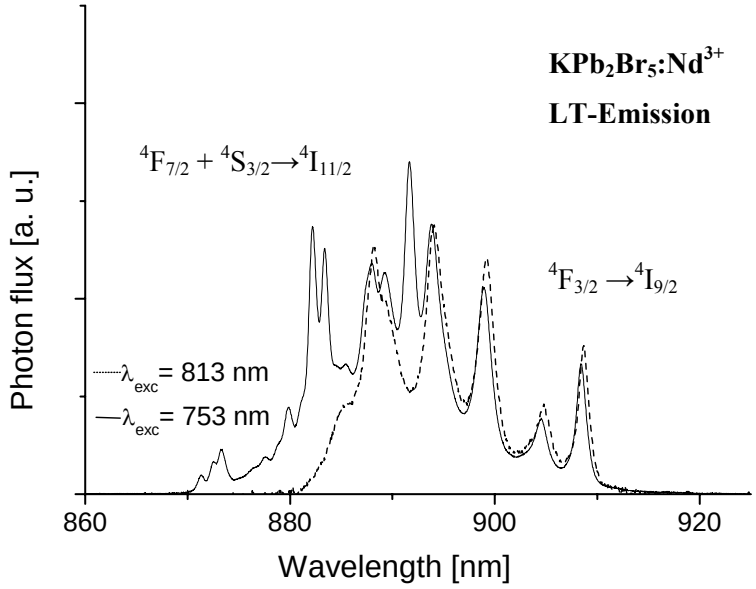

Fig. 3-23. *Low temperature emission measurement of $KPb_2Br_5:Nd^{3+}$ for different excitation wavelengths. By pumping at 753 nm the transition originating from the $^4F_{3/2}$ level into the $^4I_{9/2}$ level is overlapped by the transition from the $^4F_{7/2}$ + $^4S_{3/2}$ level into the $^4I_{11/2}$ level.*

In general, the emission at 0.89 μm (and at 0.82 μm) appears to be strong in the investigated crystals (section 3.2.1.2 and the following section) which make laser activity at these wavelengths promising. On the other hand, this section reveals a fairly small Stark level splitting of 254 cm^{-1} (Appendix D) if compared with crystals such as Nd:YAG with a splitting of 857 cm^{-1} (0.7% population at room temperature [Cze02]). So, the use of appropriate laser mirrors as well as the thermal population of the lower laser level at room temperature are factors to consider. Measurements on Nd:RPB would be useful in order to determine possible differences in the Stark level energies e.g. regarding the ground state level splitting in the two hosts of different crystal structure.

Figure 3-24 shows excitation peaks of Nd^{3+} in KPB at 10 K. Peaks around 350 nm are overlapped by a structure which is believed to originate from lead ions, the conduction band of the host lattice and maybe an exciton [Mya99]. Excitation in this absorption edge gives additional emission of Pb^{2+} disturbed sites in the red region like Nitsch observed in KPC [Nit95].

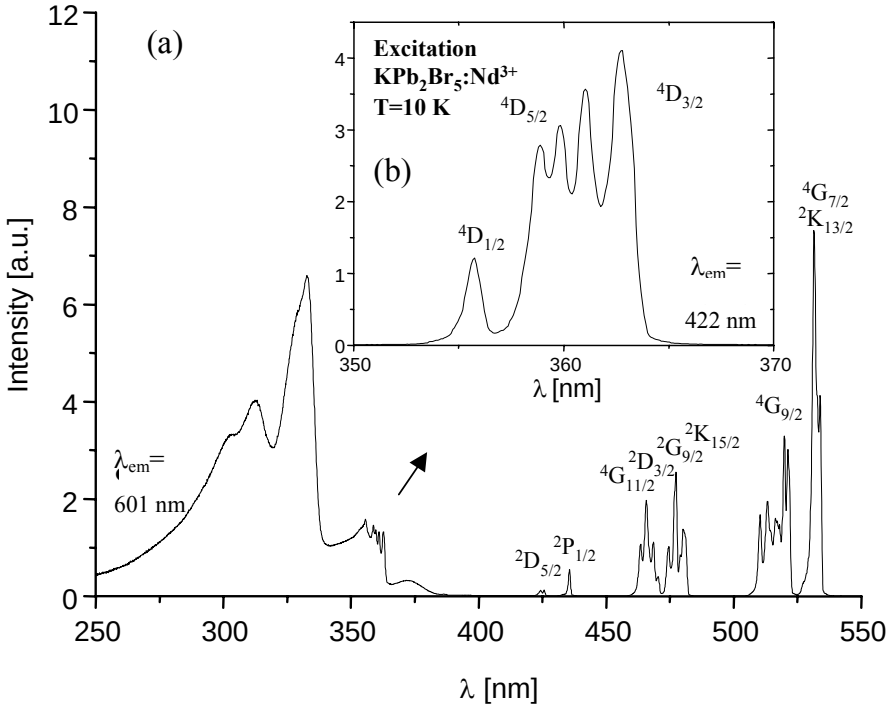

Fig. 3-24. *Excitation spectrum of $KPb_2Br_5:Nd^{3+}$ at 10 K: (a) peaks related to transitions of the Nd^{3+}-ion impacted by a structure originating from the band edge and lead ions (emission wavelength: 601 nm) (b) excitation peaks in the range 350 - 370 nm (emission wavelength: 422 nm).*

3.5 Laser Activity in Nd^{3+}-Doped KPb_2Br_5 and $RbPb_2Br_5$ Crystals

Achieving laser operation at new wavelengths in e.g. Nd^{3+} (such as 1.2 μm) was always anticipated, but several attempts - using the experimental setups and different pump sources as described in section 2.2.7 - of lasing these materials were not successful. The main factor which inhibited lasing for a long time is believed to be due to crystal quality issues (such as growth striae described in section 2.1.1). Furthermore, self-termination due to the long-lived lower laser levels has to be taken into account in the laser experiment as mentioned further below. In the following, successful laser experiments in KPB and RPB - achieved for the first time in a low-phonon energy, moisture-resistant bromide host crystal to the author`s knowledge - are reported. Laser operation in bromide crystals was previously demonstrated in Pr^{3+}:$LaBr_3$ and $PrBr_3$ which are known to be highly hygroscopic [Kam90]. In this section room temperature laser operation at 1.07 μm by direct pumping into the $^4F_{3/2}$ level of neodymium-doped MPB (M=Rb, K) crystals is reported. Laser activity at the new wavelength of 1.18 μm that resulted from the $^4F_{5/2}+^2H_{9/2}\rightarrow{}^4I_{13/2}$ transition in Nd:RPB was achieved for the first time in a solid state material. In the same crystal laser activity at a wavelength of 0.97 μm

resulting from the $^4F_{5/2}+^2H_{9/2}\rightarrow{}^4I_{11/2}$ transition was also shown for the first reported time. In both cases the upper laser level was pumped directly at 0.81 μm with an OPO system. Laser activity at these new wavelength should also be possible for Nd:KPB samples of suitable crystal quality.

The strong dependence of absorption on polarization as shown in the absorption spectrum for a Nd:RPB crystal (Fig. 3-4, section 3.2.1.1) was taken into account during the laser experiments. The absorption is due predominantly to the π- polarized component. This strong polarization dependency was not observed for the monoclinic Nd:KPB samples.

The high emission rate of transitions originating from the $^4F_{5/2}+{}^2H_{9/2}$ level relative to the $^4F_{3/2}$ level demonstrating the greatly reduced nonradiative multiphonon decay rate of the bromide versus the chloride [Nos01] was discussed in section 3.2.1.2.

Laser activity for an uncoated, flat Nd:KPB sample (length= 4.85 mm) and a Nd:RPB sample (length= 7 mm) was achieved at 1.07 μm in both host materials as described (section 2.2.7) in a nearly concentric cavity with two concave laser mirrors (high reflector transmission for the pump wavelength of ~ 0.89 μm, output coupling of ~ 3% in KPB and 7.8% in RPB for the laser wavelength). While the Nd:KPC crystal showed laser activity for the $^4F_{3/2}$ – $^4I_{11/2}$ transition with the pump wavelengths 0.76 μm ($^4F_{7/2}$), 0.81 μm ($^4F_{5/2}$), and 0.89 μm ($^4F_{3/2}$) in the cavity described, the Nd:MPB (M=K, Rb) showed in the experiments lasing exclusively by pumping the $^4F_{3/2}$ level directly (Fig. 3-3, section 3.2.1.1). This could be explained by the difference in the measured lifetimes of the $^4F_{5/2}$ pumped levels of the chloride compared with those of the bromide crystal: 2 μs (Nd:KPC) versus 124 μs (Nd:KPB) and 126 μs (Nd:RPB) (section 3.2.1.3). Remember, the quantum efficiency $\eta_{^4F_{5/2}}$ was determined to be 0.60 (Nd:KPB) and 0.59 (Nd:RPB) by taking the ratio of the measured lifetime and the calculated radiative lifetime (208 μs and 214 μs) for the $^4F_{5/2}+^2H_{9/2}$ level (section 3.2.1.3). The laser threshold with the setup described above was reached at 4 mJ (Nd:RPB) and 1.6 mJ (Nd:KPB) incident pump energy for the 1.07 μm laser wavelength. For comparison a threshold of 0.9 mJ/pulse for Nd:KPB was calculated by assuming 40% losses per roundtrip (including Fresnel losses and losses that are due to scattering and output coupling) and by neglecting the possible influence of ESA.

The pump energy absorbed is ~ 31 % in Nd:KPB and 56% for Nd:RPB by pumping with E parallel to the c-axis and lasing with E || c. 111 μJ (Nd:KPB) and 476 μJ (Nd:RPB) output was achieved with an incident pump energy of 9 mJ/pulse (maxium intensity of pump source) and the output coupling described above.

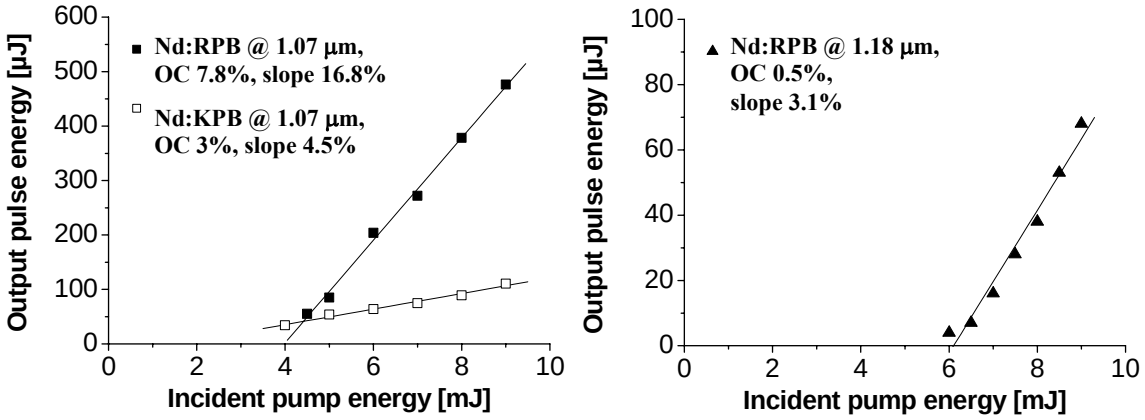

Fig. 3-25. *Input-output characteristic for an OPO pumped Nd:KPB crystal lasing at 1.07 µm (left) and a Nd:RPB crystal lasing at 1.07 µm (left) and 1.18 µm (right). The slope efficiency is given for output pulse energy with respect to absorbed pump energy. In order to achieve lasing at 1.07 µm the $^4F_{3/2}$ level was pumped directly, whereas for the 1.18 µm and 0.97 µm laser wavelengths the $^4F_{5/2}$ level was pumped.*

The slope efficiency for Nd:KPB was determined from the data in Figure 3-25 to be 1.4 % which gives 4.5% for the output energy with respect to absorbed pump energy. The slope efficiency for Nd:RPB was determined from the data in Figure 3-25 to be 9.4 % which gives 16.8 % for the output energy with respect to absorbed pump energy.

In addition to a laser wavelength of 1.07 µm, the Nd:RPB crystal ($N_c \sim 10^{19}$ cm^{-3}) revealed laser activity at 0.97 µm and at 1.18 µm in the same cavity as described above by also pumping the upper laser level directly at 0.81 µm (Fig. 3-3). Here, an output coupling of 0.2% for 0.97 µm and of 0.5% for 1.18 µm was used. The laser threshold was reached at ~ 6.5 mJ incident pump energy for 0.97 µm, and at 6.1 mJ for 1.18 µm. 68 µJ output was achieved with an incident pump energy of 9 mJ/pulse at 1.18 µm, whereas approximately one third the output was achieved at 0.97 µm (not shown in the figure). The pump energy absorbed was 72% for Nd:RPB for pumping with E parallel to the c-axis. The slope efficiency for Nd:RPB was determined from the data in Figure 3-25 to be 2.2 % which gives 3.1 % for the output energy with respect to absorbed pump energy. Tunability may well be possible at these new wavelengths that result from the $^4F_{5/2}+^2H_{9/2}$ level in the bromide crystals (Fig. 3-5). Laser experiments are intended to be continued by using a pump source with longer pulse length. However, the accumulation of population in the lower long lived laser level ^4I_J (J= 11/2, 13/2) favors pulsed operation rather than the cw mode in these rare earth-doped bromide materials ($\tau_{lower\ level} > \tau_{upper\ level}$, self-termination) if there are no processes involved which could depopulate the lower laser level (see 3 µm Er-doped Garnet laser [Hub88]). Depopulation of the lower laser levels by e.g. cross relaxation may permit cw operation at high Nd

concentration. Processes such as reabsorption and possible depopulation mechanisms will be further discussed in section 3.6. Bright upconversion fluorescence was observed in the bromide crystals during the laser experiments and could possibly enable short-wavelength lasing in these crystals (section 3.7).

Laser experiments as described in section 2.7 for the Tb^{3+}-doped KPB crystals in the long wavelength region were not successful so far, but further attempts are planned as soon as the exact factors which inhibited lasing during these first experiments are identified.

3.6 Optical Pump-Probe Processes and Depopulation Mechanisms of the Lower Laser Levels in Nd^{3+}-Doped KPb_2Br_5, $RbPb_2Br_5$, and KPb_2Cl_5

The main purpose of the present study is to gain further insights into the lasing potential of Nd^{3+} in RPB and KPB, especially for the new laser wavelengths (previous section) resulting from the $^4F_{5/2}+^2H_{9/2}$ level such as 1.18 μm. In the following cw pump-probe spectra are presented in order to discuss excited state absorption (ESA) and reabsorption processes (RA) due to the lower long lived laser levels, as well as possible depopulation mechanisms feasible for more efficient laser operation in these bromide crystals. Signal strengths and effective cross sections of ESA and RA transitions competing with the (laser) emission transitions, as well as cross relaxation (CR) processes among the lower laser levels, will be given. Figure 3-26 depicts the transitions responsible for the ESA, RA, CR, pump, and gain. For comparison pump-probe spectra will also be presented for the potassium-lead-chloride host (Nd^{3+}:KPb_2Cl_5). Cw pump-probe spectra were determined as described in section 2.2.6 for Nd:KPB, Nd:RPB and Nd:KPC ranging from 780 – 1550 nm by pumping into the $^4F_{3/2}$, $^4F_{5/2}+^2H_{9/2}$ and $^4F_{7/2}+^4S_{3/2}$ levels, respectively.

Note, that emission (thick line) and pump-probe spectra (thin line) in Figure 3-27 and 3-29 - displayed on different scales - can not be compared quantitatively. In order to simplify this discussion, potential transitions resulting from the $^4F_{7/2}+^4S_{3/2}$ level have been neglected in this study.

Figure 3-27 shows the measured spectra of a Nd:KPB crystal in the wavelength region 780-1500 nm. The spectra were determined by pumping into the $^4F_{3/2}$ (a) and $^4F_{7/2}+^4S_{3/2}$ (b) levels, shown in the upper and lower frames, respectively. The inset in (b) displays a magnification for the peaks in the wavelength range 1135 – 1500 nm. Spectra measured by pumping into the $^4F_{5/2}+^2H_{9/2}$ level showed in principle similar features to the spectrum shown in Figure 3-27(b). Reabsorption and excited state absorption compete with gain as indicated.

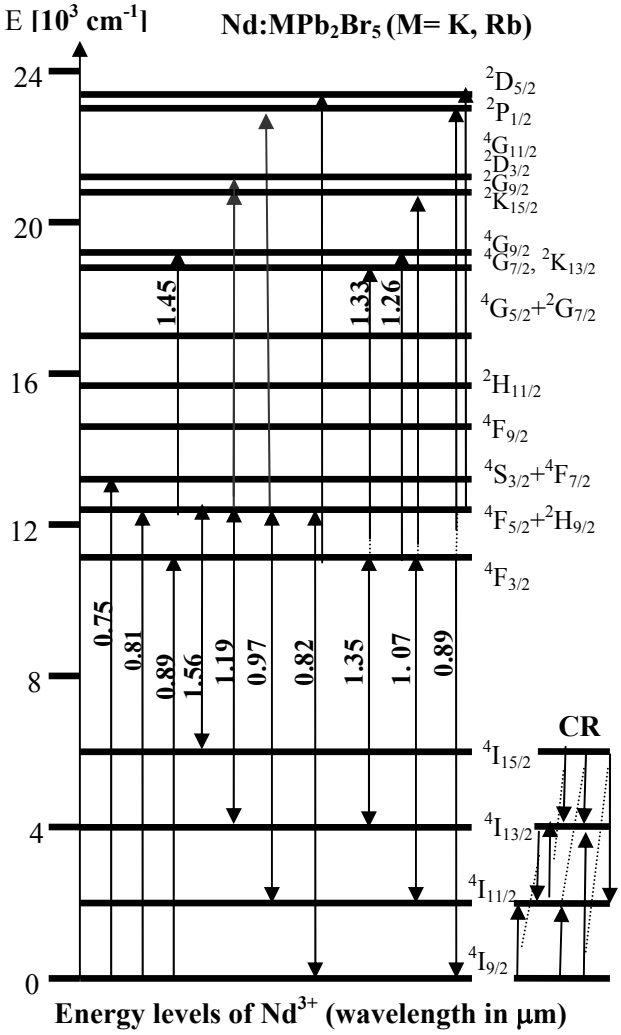

Fig. 3-26. *Energy level diagram of Nd:MPB (M= K, Rb) displays new transitions from the $^4F_{5/2}$+ $^2H_{9/2}$ level, in addition to the conventional laser transitions from the $^4F_{3/2}$ level. Excited state absorption transitions resulting from the $^4F_{5/2}$+ $^2H_{9/2}$ and $^4F_{3/2}$ levels as well as depopulation mechansims for the long lived lower laser levels ^4I_J (J=13/2, 15/2) via cross relaxation (CR) are indicated. Reabsorption can occur from the lower long lived laser levels. The pump transitions at 0.75, 0.81, and 0.89 μm are indicated. (Transitions originating from the $^4F_{7/2}$+ $^4S_{3/2}$ level have been neglected in order to simplify the discussion.).*

The cw pump-probe spectra in Figure 3-27 show reabsorption features resulting from the $^4I_{11/2}$ and $^4I_{13/2}$ levels as indicated. The peak RA wavelength matches the peak wavelength in emission as expected. The ratio of reabsorption transitions emanating from the $^4I_{13/2}$ and $^4I_{11/2}$ levels proves that the $^4I_{13/2}$ population is reduced compared to the $^4I_{11/2}$ level population, which is likely due to cross relaxation (CR, see Fig. 3-26) and/or radiative processes. The influence of multiphonon decay is small because of the large energy gap to the next lowest level ~2000 cm^{-1} involving more than 12 phonons ($\hbar\omega_{eff}$ = 160 cm^{-1} assumed).

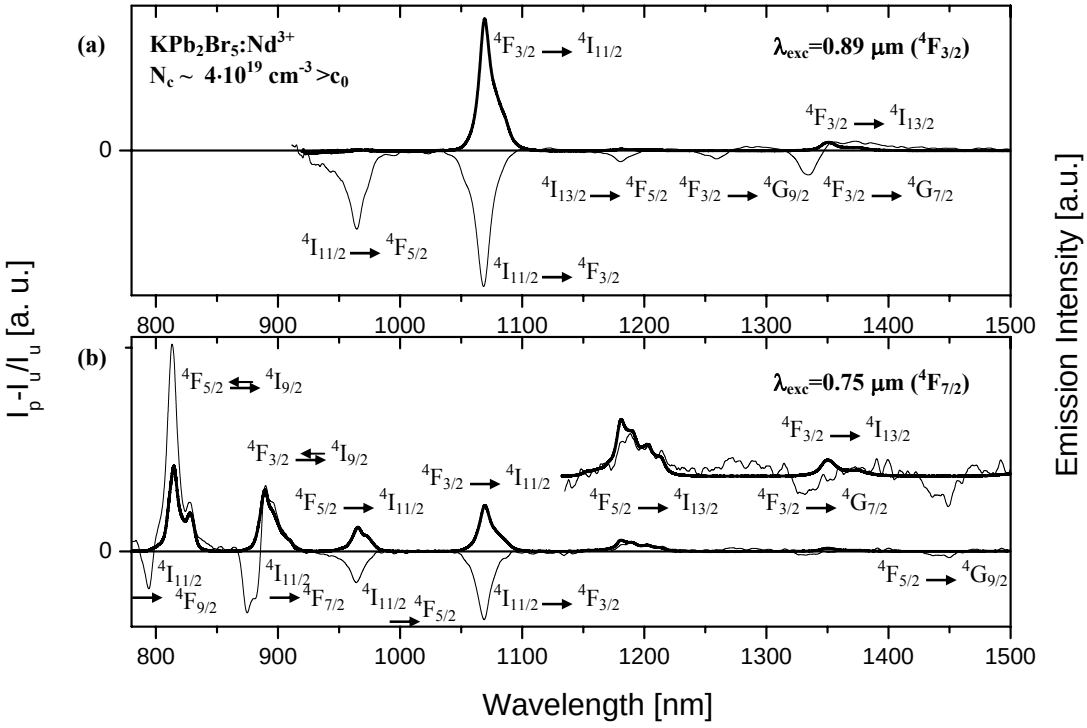

Fig. 3-27. *Emission spectra (thick line) and pump-probe spectra (thin line) of Nd^{3+}:KPb_2Br_5 determined by pumping into either the $^4F_{3/2}$ (a) or $^4F_{7/2}$+$^4S_{3/2}$ (b) level, respectively (using same crystal for both spectra). The inset in (b) displays a ~ 5x magnification for the wavelength range 1135 – 1500 nm. Reabsorption and excited state absorption compete with gain as indicated. Depopulation via cross relaxation leads to less reabsorption of transitions from the $^4I_{13/2}$ level compared to the $^4I_{11/2}$. Note, that only the main transitions are indicated (Table 3-10(a) shows others) and that the $^4F_{5/2}$+$^2H_{9/2}$ and $^4F_{7/2}$+$^4S_{3/2}$ levels are abbreviated by $^4F_{5/2}$ and $^4F_{7/2}$, respectively.*

The calculated transitions, their signal strengths, and their effective cross sections are listed in Table 3-10(a). The Nd:KPB transitions of Table 3-10(a) thought to be observed as the main transitions in the spectra of Figure 3-28 are denoted with an asterisk. Table 3-10(b) contains the results for Nd:RPB, to be discussed below. Note, that the same energies in the Stark level splitting (section 3.4) were assumed for Nd^{3+} in KPB and RPB, although it might be different for Nd:RPB due to the different crystal structure (section 2.1.2).

The line strengths S of induced electric dipole (ED) transitions are calculated for Nd:KPB by using the Judd-Ofelt intensity parameters Ω_2= 15.70 x10^{-20} cm^2, Ω_4= 6.25 x10^{-20} cm^2, Ω_6= 2.96 x10^{-20} cm^2 of Nd:KPB (section 3.2.1.1) and the reduced matrix elements given in Kaminskii [Kam96]. The line strengths S of magnetic dipole (MD) transitions (section 1.2.2.1) were calculated in the intermediate coupling scheme by using the formulas given in Weber [Web67] for calculating S^{MD} in the LS coupling scheme and by using the energy eigenvectors of intermediate coupled states for Nd^{3+} from Wybourne [Wyb61]. The effective cross sections are calculated by using the following formula [Kam90]:

$$\Sigma^{eff} = \frac{\int \sigma d\lambda}{\bar{\lambda}^2} = \frac{4\pi^2 e^2}{3\hbar c} \cdot \frac{1}{\bar{\lambda} \cdot (2J+1)} \left[\frac{(n^2+2)^2}{9n} S^{ED} + nS^{MD} \right] = \frac{A_{JJ'} \cdot \bar{\lambda}^2}{8\pi c n^2}, \qquad (3\text{-}12)$$

where J is the initial level, n the (averaged) refractive index (here, 2.16 for KPB and 2.08 for RPB was taken), S^{MD} and S^{ED} the calculated signal strengths of magnetic dipole and induced electric dipole, $A_{JJ'}$ the transition rate (section 1.2.2.1), and $\bar{\lambda}$ is the averaged wavelength of the transition (calculated by taking the difference of the centroids of the crystal field levels of Nd:KPB, Appendix D).

Table 3-10(a). *Calculated line strengths S of induced electric dipole (ED) and of magnetic dipole (MD) transitions for relevant emission (EM), reabsorption (RA), bleaching and excited state absorption (ESA) transitions for Nd:KPB. The electric dipole quantities are calculated with the following Judd-Ofelt parameters: Ω_2= 15.70, Ω_4= 6.25, Ω_6= 2.96 [x10^{-20} cm^2]. The magnetic dipole quantities are determined in the intermediate coupling scheme (values < 0.01 are not listed). The effective cross section Σ^{eff} is calculated by using eqn. 3-12 in this section.*

λ (μm)	**Emission Transition (J→J')**	**$S^{ED}+S^{MD}$ [x10^{-20}cm^2]**	**Σ^{eff} [x10^{-18}cm]**	**ESA/ Bleaching / Reabsorption Transitions (J→J')**	**$S^{ED}+S^{MD}$ [x10^{-20}cm^2]**	**Σ^{eff} [x10^{-18}cm]**
1.44				$^4F_{5/2}\rightarrow{}^4G_{9/2}$*	3.79	9.61
1.48				$^2H_{9/2}\rightarrow{}^4G_{9/2}$*	1.17+0.01	1.74
1.36	$^4F_{3/2}\rightarrow{}^4I_{13/2}$*	0.62	2.49	$^4I_{13/2}\rightarrow{}^4F_{3/2}$*	0.62	0.71
1.37				$^4I_{15/2}\rightarrow{}^4F_{7/2}$	2.80	2.80
1.35				$^4I_{15/2}\rightarrow{}^4S_{3/2}$	0.98	0.99
1.34				$^4F_{3/2}\rightarrow{}^2K_{13/2}$	0.02	0.09
1.335				$^4F_{3/2}\rightarrow{}^4G_{7/2}$*	1.91	7.85
1.255				$^4F_{3/2}\rightarrow{}^4G_{9/2}$*	0.82	3.60
1.19	$^4F_{5/2}\rightarrow{}^4I_{13/2}$*	2.32	7.11	$^4I_{13/2}\rightarrow{}^4F_{5/2}$*	2.32	3.05
1.17	$^2H_{9/2}\rightarrow{}^4I_{13/2}$*	0.99	1.86	$^4I_{13/2}\rightarrow{}^2H_{9/2}$*	0.99	1.33
1.21				$^2H_{9/2}\rightarrow{}^2K_{15/2}$ [(a)]	4.21	7.65
1.18				$^4F_{5/2}\rightarrow{}^2K_{15/2}$	0.02	0.05
1.20				$^2H_{9/2}\rightarrow{}^2G_{9/2}$	0.46+0.04	0.92
1.17				$^4F_{5/2}\rightarrow{}^2G_{9/2}$	0.89	2.78
1.17				$^2H_{9/2}\rightarrow{}^2D_{3/2}$	0.44	0.83
1.15				$^4F_{5/2}\rightarrow{}^2D_{3/2}$	0.06+0.01	0.23
1.14				$^2H_{9/2}\rightarrow{}^4G_{11/2}$ [(a)]	2.75+0.01	5.31
1.12				$^4F_{5/2}\rightarrow{}^4G_{11/2}$ [(a)]	0.97	3.16
1.07	$^4F_{3/2}\rightarrow{}^4I_{11/2}$*	1.93	9.84	$^4I_{11/2}\rightarrow{}^4F_{3/2}$*	1.93	3.28
1.07				$^4I_{13/2}\rightarrow{}^4F_{7/2}$	2.05	3.00

1.06				$^4I_{13/2}\rightarrow{}^4S_{3/2}$	0.98	1.45
1.02				$^4I_{15/2}\rightarrow{}^2H_{11/2}$	2.49	3.36
1.05				$^4F_{3/2}\rightarrow{}^2K_{15/2}$	0.03	0.15
1.045				$^4F_{3/2}\rightarrow{}^2G_{9/2}$	0.20	1.04
1.00				$^4F_{3/2}\rightarrow{}^4G_{11/2}$	0.30	1.66
0.97	$^4F_{5/2}\rightarrow{}^4I_{11/2}$*	1.16	4.39	$^4I_{11/2}\rightarrow{}^4F_{5/2}$*	1.16	2.20
0.95	$^2H_{9/2}\rightarrow{}^4I_{11/2}$*	0.12	0.29	$^4I_{11/2}\rightarrow{}^2H_{9/2}$*	0.12	0.24
0.94				$^4I_{13/2}\rightarrow{}^4F_{9/2}$*	2.95	4.92
0.96				$^2H_{9/2}\rightarrow{}^2P_{1/2}$	0.55	1.26
0.94				$^4F_{5/2}\rightarrow{}^2P_{1/2}$	0.15	0.57
0.89	$^4F_{3/2}\rightarrow{}^4I_{9/2}$*	1.60	9.81	$^4I_{9/2}\rightarrow{}^4F_{3/2}$*	1.60	3.92
0.885				$^4I_{11/2}\rightarrow{}^4F_{7/2}$*	2.41	4.98
0.88				$^4I_{11/2}\rightarrow{}^4S_{3/2}$*	0.62	1.29
0.84				$^4I_{13/2}\rightarrow{}^2H_{11/2}$	0.19	0.36
0.91				$^2H_{9/2}\rightarrow{}^2D_{5/2}$	0.55	1.32
0.89				$^4F_{5/2}\rightarrow{}^2D_{5/2}$	0.15	0.60
0.86				$^4F_{3/2}\rightarrow{}^2P_{1/2}$	0.20	1.29
0.82	$^4F_{5/2}\rightarrow{}^4I_{9/2}$*	2.67	11.97	$^4I_{9/2}\rightarrow{}^4F_{5/2}$*	2.67	7.18
0.805	$^2H_{9/2}\rightarrow{}^4I_{9/2}$*	0.54+0.02	1.51	$^4I_{9/2}\rightarrow{}^2H_{9/2}$*	0.54+0.02	1.51
0.79				$^4I_{11/2}\rightarrow{}^4F_{9/2}$*	1.31	3.01
0.78				$^4I_{15/2}\rightarrow{}^2K_{13/2}$	0.03	0.05
0.81				$^4F_{3/2}\rightarrow{}^2D_{5/2}$	0.20	1.35

[(a)]Not clear why these transitions are not observed.
*Indicated as the main observed transitions for Nd:KPB in Figure 3-27.

Table 3-10(b). *Calculated line strengths S of induced electric dipole (ED) and of magnetic dipole (MD) transitions for relevant emission (EM), reabsorption (RA), bleaching and excited state absorption (ESA) transitions for Nd:RPB. The electric dipole quantities are calculated with the following Judd-Ofelt parameters: Ω_2= 0.41, Ω_4= 9.32, Ω_6= 2.56 [x10^{-20} cm^2]. The magnetic dipole quantities are determined in the intermediate coupling scheme (values < 0.01 are not listed). The effective cross section Σ^{eff} is calculated by using eqn. 3-12 in this section.*

λ (μm)	**Emission Transition (J→J')**	**$S^{ED}+S^{MD}$ [x$10^{-20}$$cm^2$]**	**Σ^{eff} [x10^{-18}cm]**	**ESA/ Bleaching / Reabsorption Transitions (J→J')**	**$S^{ED}+S^{MD}$ [x$10^{-20}$$cm^2$]**	**Σ^{eff} [x10^{-18}cm]**
1.44				$^4F_{5/2}\rightarrow{}^4G_{9/2}$	1.07	2.55
1.48				$^2H_{9/2}\rightarrow{}^4G_{9/2}$	0.70+0.01	0.98
1.36	$^4F_{3/2}\rightarrow{}^4I_{13/2}$*	0.53	2.01	$^4I_{13/2}\rightarrow{}^4F_{3/2}$*	0.53	0.58
1.37				$^4I_{15/2}\rightarrow{}^4F_{7/2}$	3.03	2.83
1.35				$^4I_{15/2}\rightarrow{}^4S_{3/2}$	0.85	0.80
1.34				$^4F_{3/2}\rightarrow{}^2K_{13/2}$	0.02	0.07
1.335				$^4F_{3/2}\rightarrow{}^4G_{7/2}$*	0.59	2.25

1.255				$^4F_{3/2}\rightarrow{}^4G_{9/2}$*	0.82	3.89
1.19	$^4F_{5/2}\rightarrow{}^4I_{13/2}$*	2.71	7.78	$^4I_{13/2}\rightarrow{}^4F_{5/2}$*	2.71	3.34
1.17	$^2H_{9/2}\rightarrow{}^4I_{13/2}$*	0.37	0.65	$^4I_{13/2}\rightarrow{}^2H_{9/2}$*	0.37	0.46
1.21				$^2H_{9/2}\rightarrow{}^2K_{15/2}$[(a)]	5.49	9.33
1.18				$^4F_{5/2}\rightarrow{}^2K_{15/2}$	0.01	0.04
1.20				$^2H_{9/2}\rightarrow{}^2G_{9/2}$	0.38+0.04	0.73
1.17				$^4F_{5/2}\rightarrow{}^2G_{9/2}$	0.36	1.05
1.17				$^2H_{9/2}\rightarrow{}^2D_{3/2}$	0.48	0.85
1.15				$^4F_{5/2}\rightarrow{}^2D_{3/2}$	0.00+0.01	0.03
1.14				$^2H_{9/2}\rightarrow{}^4G_{11/2}$	0.08+0.01	0.17
1.12				$^4F_{5/2}\rightarrow{}^4G_{11/2}$[(a)]	1.08	3.30
1.07	$^4F_{3/2}\rightarrow{}^4I_{11/2}$*	2.11	10.09	$^4I_{11/2}\rightarrow{}^4F_{3/2}$*	2.11	3.37
1.07				$^4I_{13/2}\rightarrow{}^4F_{7/2}$	3.06	4.19
1.06				$^4I_{13/2}\rightarrow{}^4S_{3/2}$	0.85	1.17
1.02				$^4I_{15/2}\rightarrow{}^2H_{11/2}$	0.70	0.89
1.05				$^4F_{3/2}\rightarrow{}^2K_{15/2}$	0.03	0.12
1.045				$^4F_{3/2}\rightarrow{}^2G_{9/2}$	0.25	1.20
1.00				$^4F_{3/2}\rightarrow{}^4G_{11/2}$	0.27	1.38
0.97	$^4F_{5/2}\rightarrow{}^4I_{11/2}$*	1.66	5.88	$^4I_{11/2}\rightarrow{}^4F_{5/2}$*	1.66	2.94
0.95	$^2H_{9/2}\rightarrow{}^4I_{11/2}$*	0.07	0.16	$^4I_{11/2}\rightarrow{}^2H_{9/2}$*	0.07	0.13
0.94				$^4I_{13/2}\rightarrow{}^4F_{9/2}$	3.36	5.25
0.96				$^2H_{9/2}\rightarrow{}^2P_{1/2}$	0.82	1.75
0.94				$^4F_{5/2}\rightarrow{}^2P_{1/2}$	0.00	0.01
0.89	$^4F_{3/2}\rightarrow{}^4I_{9/2}$*	2.28	13.10	$^4I_{9/2}\rightarrow{}^4F_{3/2}$*	2.28	5.24
0.885				$^4I_{11/2}\rightarrow{}^4F_{7/2}$*	3.00	5.81
0.88				$^4I_{11/2}\rightarrow{}^4S_{3/2}$*	0.53	1.04
0.84				$^4I_{13/2}\rightarrow{}^2H_{11/2}$	0.17+0.01	0.31
0.91				$^2H_{9/2}\rightarrow{}^2D_{5/2}$	0.82	1.84
0.89				$^4F_{5/2}\rightarrow{}^2D_{5/2}$	0.00	0.02
0.86				$^4F_{3/2}\rightarrow{}^2P_{1/2}$	0.00	0.04
0.82	$^4F_{5/2}\rightarrow{}^4I_{9/2}$*	3.23	13.51	$^4I_{9/2}\rightarrow{}^4F_{5/2}$*	3.23	8.11
0.805	$^2H_{9/2}\rightarrow{}^4I_{9/2}$*	0.37+0.02	1.00	$^4I_{9/2}\rightarrow{}^2H_{9/2}$*	0.37+0.02	1.00
0.79				$^4I_{11/2}\rightarrow{}^4F_{9/2}$	1.26	2.73
0.78				$^4I_{15/2}\rightarrow{}^2K_{13/2}$	0.03	0.04
0.81				$^4F_{3/2}\rightarrow{}^2D_{5/2}$	0.01	0.03

[(a)]Not clear why these transitions are not observed.
*Indicated as the main observed transitions for Nd:RPB in Figure 3-29.

Table 3-11 shows the calculated radiative lifetimes and measured lifetimes for relevant initial levels in neodymium-doped KPB, RPB and KPC discussed in this study. The radiative

lifetime of the $^4I_{11/2}$ level in Nd:KPB is calculated to be about 3-4 times longer than for the other ^4I_J levels (J=13/2, 15/2). Differences in the measured and calculated lifetimes for the ^4I_J level are due to concentration quenching such as cross relaxation and/or energy transfer to impurities and possibly an error in the Judd-Ofelt calculation. The branching ratio of the $^4F_{5/2}+{}^2H_{9/2} \rightarrow {}^4I_{13/2}$ transition is calculated to be similar as revealed by emission spectrum and higher as revealed from Judd-Ofelt theory calculations (section 3.2.1.2) in comparison with the branching ratio of the $^4F_{5/2}+{}^2H_{9/2} \rightarrow {}^4I_{11/2}$ transition in Nd:KPB.

Table 3-11. *Calculated radiative τ^{rad} and measured τ^{meas} lifetimes for the initial level J of the relevant emission, reabsorption, cross relaxation, and excited state absorption processes for Nd:KPB and Nd:RPB. For comparison lifetimes of Nd:KPC are given.*

Energy level	Nd:KPB		Nd:RPB		Nd:KPC	
	τ^{rad} [ms]	(τ^{meas}) [ms]	τ^{rad} [ms]	τ^{meas} [ms]	τ^{rad} [ms]	τ^{meas} [ms]
$^4I_{11/2}$	45.8	5.0[e]	57.5	-	44.1[a]	2.0-2.3[d]
$^4I_{13/2}$	14.3	1.1[e]	18.2	-	12.9[a]	6-0.3[d]
$^4I_{15/2}$	12.6	0.7[e], 1.2[f]	16.2	-	11.1[a]	8-0.2[d]
$^4F_{3/2}$	0.128	0.145	0.116	0.119	0.148[a]	0.255
$^4F_{5/2}+{}^2H_{9/2}$	0.208[b], 0.153[c]	0.124	0.214[b], 0.150[c]	0.126	0.233 [a,b], 0.173 [a,c]	0.002

[a] determined by using Judd-Ofelt intensity parameters of Nd:KPC [Nos02] Ω_2= 13.26, Ω_4= 5.63, Ω_6= 4.71 [x10^{-20} cm^2].
[b] τ^{rad} determined by assuming statistically distributed populations using the high temperature limit E_i<<kT.
[c] τ^{rad} determined by assuming statistically distributed populations using crystal field level energies of Nd:KPB.
[d] after Jenkins *et al.* [Jen02]; variation of Nd concentration 0.88-7.4·10^{19} cm^{-3}.
[e] after Hoemmerich *et al.* [Hoe04], Nd concentration ~ 4.7·10^{19} cm^{-3}.
[f] measured by exciting the $^4I_{15/2}$ level and detecting at 2.5 μm; Nd concentration ~ 1.7-2.35·10^{19} cm^{-3}.

Interestingly, with respect to the following discussion of the cw pump-probe spectra from the crystals Nd:KPB, Nd:RPB and Nd:KPC with different Nd dopant concentrations, it is suggested that the $^4I_{13/2}$ level depopulation occurs via cross relaxation (Fig. 3-26, Tab. 3-12) leading mainly to less reabsorption of transitions from the $^4I_{13/2}$ level compared to the $^4I_{11/2}$ level; as a result, the $^4F_{5/2}+{}^2H_{9/2} \rightarrow {}^4I_{13/2}$ transition around 1.2 μm should be more favorable for efficient laser operation under longer pulses or maybe even cw pumping. Refering to Figure 3-27, net gain is observed for this transition of high cross section at 1.18 μm in contrast to reabsorption at 1.07 μm and at 0.97 μm due to the shorter level lifetime of the $^4I_{13/2}$ versus $^4I_{11/2}$. Of course, laser operation was observed for all of these transitions (1.18 μm, 0.97 μm and 1.07 μm) as shown in section 3.5 due to the short pump pulse length (~10 ns). Following a study in Nd:KPC [Jen02], cross relaxation becomes significant for Nd

concentrations ≥ $2(\pm1)\cdot10^{19}$ cm^{-3}. This is revealed by fitting the lifetime data of Nd:KPC in Jenkins *et al.* [Jen02] to $\tau=\tau_0/(1+(c/c_0)^2)$ where c stands for the concentration and c_0, and τ_0 ($\tau(c\rightarrow0)$) are (fitting) parameters. In Nd:KPC the lifetime of the $^4I_{13/2}$ level is reported to drop from 6 ms to 0.3 ms if the concentration is increased from $0.88\cdot10^{19}$ cm^{-3} to $7.4\cdot10^{19}$ cm^{-3} (Tab. 3-11, [Jen02]). The Nd:KPB sample used in the pump and probe measurements presented has a Nd concentration N_c of $\sim 4\cdot10^{19}$ cm^{-3}, suggesting that fast cross relaxation occurs. As shown later in this section no net gain is observed at 1.18 μm for either the Nd:KPC crystal due to fast relaxation out of the $^4F_{5/2}+^2H_{9/2}$ level (2 μs, Tab. 3-11), nor for the Nd:RPB crystal due to low Nd concentration and absence of significant cross relaxation; compare Figures 3-27 and 3-29.

Table 3-12. *Calculated line strengths S of induced electric dipole (ED) and of magnetic dipole (MD) transitions for Nd:KPB (a) and Nd:RPB (b). Cross relaxation (CR) depopulates the lower long lived laser levels ^4I_J (J=13/2 and 15/2). The integrated cross sections Σ^{eff} of Nd:KPB are slightly higher than for Nd:RPB.*

	λ (μm)	Transition (J→J')	$S^{ED}+S^{MD}$ ($x10^{-20}cm^2$)	Σ^{eff} [$x10^{-18}cm$]
(a)				
CR1	5.07	$^4I_{13/2}\rightarrow{}^4I_{11/2}$	4.91+0.93	1.79
	5.31	$^4I_{9/2}\rightarrow{}^4I_{11/2}$	4.43+0.70	2.10
CR2	2.49	$^4I_{15/2}\rightarrow{}^4I_{11/2}$	1.31	0.72
	2.59	$^4I_{9/2}\rightarrow{}^4I_{13/2}$	1.44	1.22
CR3	4.88	$^4I_{15/2}\rightarrow{}^4I_{13/2}$	5.35+0.71	1.69
	5.07	$^4I_{11/2}\rightarrow{}^4I_{13/2}$	4.91+0.93	2.09
CR4	4.88	$^4I_{15/2}\rightarrow{}^4I_{13/2}$	5.35+0.71	1.69
	5.31	$^4I_{9/2}\rightarrow{}^4I_{11/2}$	4.43+0.70	2.10
(b)				
CR1	5.07	$^4I_{13/2}\rightarrow{}^4I_{11/2}$	4.44+0.93	1.55
	5.31	$^4I_{9/2}\rightarrow{}^4I_{11/2}$	3.99+0.70	1.80
CR2	2.49	$^4I_{15/2}\rightarrow{}^4I_{11/2}$	1.17	0.61
	2.59	$^4I_{9/2}\rightarrow{}^4I_{13/2}$	1.29	1.02
CR3	4.88	$^4I_{15/2}\rightarrow{}^4I_{13/2}$	4.83+0.71	1.45
	5.07	$^4I_{11/2}\rightarrow{}^4I_{13/2}$	4.44+0.93	1.80
CR4	4.88	$^4I_{15/2}\rightarrow{}^4I_{13/2}$	4.83+0.71	1.45
	5.31	$^4I_{9/2}\rightarrow{}^4I_{11/2}$	3.99+0.70	1.80

Reabsorptions resulting from the $^4I_{15/2}$ level are also weak e.g. due to cross relaxation processes as indicated in Figure 3-26 and Table 3-12. This could be useful for other (laser) transitions. For example, the $^4F_{5/2}+^2H_{9/2}\rightarrow{}^4I_{15/2}$ transition at 1.56 µm as displayed in Figure 3-28(a). Measurements show e.g. that the $^4I_{15/2}\rightarrow{}^4I_{11/2}$ emission overlaps the $^4I_{9/2}\rightarrow{}^4I_{13/2}$ absorption transition (Fig. 3-28(b)). Moreover, alternative depopulation mechanisms for the long-lived lower ^4I_J laser levels could involve the use of codopants with appropriate absorption lines such as Tb^{3+}, which has an absorption feature in the region ~ 4.2-5.6 µm (section 3.2.2.1, Fig. 3-8).

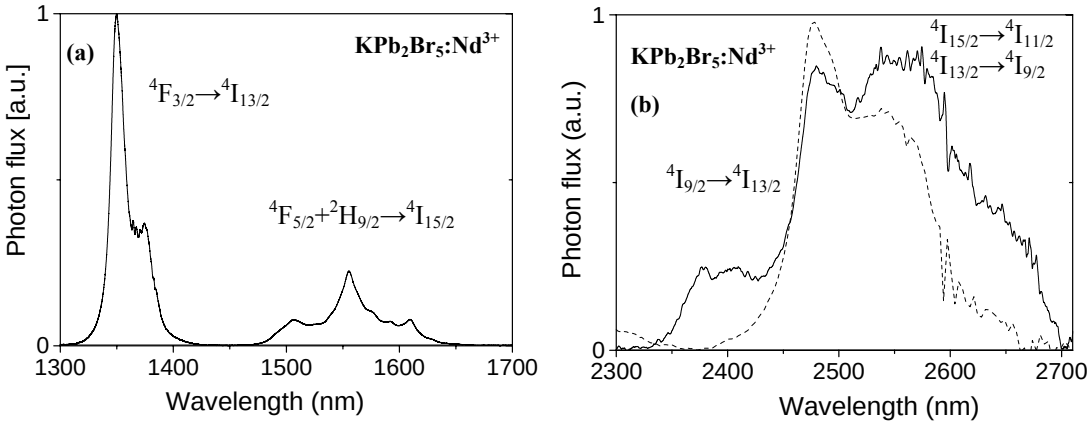

Fig. 3-28. *Emission and absorption spectra resulting from or into the ^4I_J (J=15/2, 13/2, 11/2, 9/2) level. The emission from the $^4F_{5/2}$ + $^2H_{9/2}$ into the $^4I_{15/2}$ level is observed due to the low-phonon energy of the bromides (a). Cross relaxation processes can depopulate e.g. the $^4I_{15/2}$ level (b).*

As noted, the use of different pump wavelengths have a significant impact on the spectra. While pumping into the $^4F_{3/2}$ level (Fig. 3-27(a)) shows reabsorption e.g. at 1.18 µm, gain is observed at 1.18 µm by pumping into the $^4F_{7/2}+{}^4S_{3/2}$ level (Fig. 3-27(b)). In addition, excited state absorption at ~1.45 µm resulting from the $^4F_{5/2}+{}^2H_{9/2}$ level into the $^4G_{9/2}$ is observed only if the $^4F_{5/2}+{}^2H_{9/2}$ level is populated, Fig. 3-27(b)). In contrast, excited state absorption from the $^4F_{3/2}$ level into the $^4G_{9/2}$ is observed at ~1.26 µm only by pumping the $^4F_{3/2}$ level directly (Fig. 3-27(b)). Excited state absorption from the $^4F_{3/2}$ level into the $^4G_{7/2}$ at ~1.33 µm as well as gain resulting from the $^4F_{3/2}\rightarrow{}^4I_{13/2}$ transition at ~1.35 µm is observed if the $^4I_{13/2}$ level is rapidly depopulated e.g. by cross relaxation and the $^4F_{3/2}$ level is directly pumped (Fig. 3-27(a)). Note, that the gain of the $^4F_{5/2}+^2H_{9/2}\rightarrow{}^4I_{13/2}$ transition is bigger than for $^4F_{3/2}\rightarrow{}^4I_{13/2}$ transition (Fig. 3-27(b)) since the $^4F_{7/2}+{}^4S_{3/2}$ level is pumped, and the cross section of the transition resulting from the combined $^4F_{5/2}+^2H_{9/2}$ level into the $^4I_{13/2}$ level is slightly higher than for the $^4F_{3/2}\rightarrow{}^4I_{13/2}$ transition (section 3.2.1.2). Also, the above mentioned influence of ESA observed for the $^4F_{3/2}\rightarrow{}^4I_{13/2}$ transition defeats gain. ESA influencing the

$^4F_{5/2}+^2H_{9/2}\rightarrow{}^4I_{13/2}$ is not observed even though it is predicted (e.g. $^2H_{9/2}\rightarrow{}^2K_{15/2}$, Tab. 3-10). The negative features around 0.79 and 0.88 μm are mainly due to reabsorption from the $^4I_{11/2}\rightarrow{}^4F_{9/2}$ and $^4I_{11/2}\rightarrow{}^4F_{7/2}+{}^4S_{3/2}$ transitions, respectively. The nearby positive features arise from bleaching of the ground state absorption and emission.

The cw pump-probe and the emission spectra of a Nd:RPB crystal displayed in Figure 3-29 (b) are induced by pumping into the $^4F_{7/2}+^4S_{3/2}$ level. The transitions and their signal strengths are listed in Table 3-10(b). The line strengths S of induced electric dipole (ED) are calculated by using the Judd-Ofelt intensity parameters for Nd:RPB (section 3.2.1.1) Ω_2= 0.41 x10^{-20} cm^2, Ω_4= 9.32 x10^{-20} cm^2, Ω_6= 2.56 10^{-20} cm^2. The Nd:RPB crystal reveals similar features to Nd:KPB (Fig. 3-27(b)).

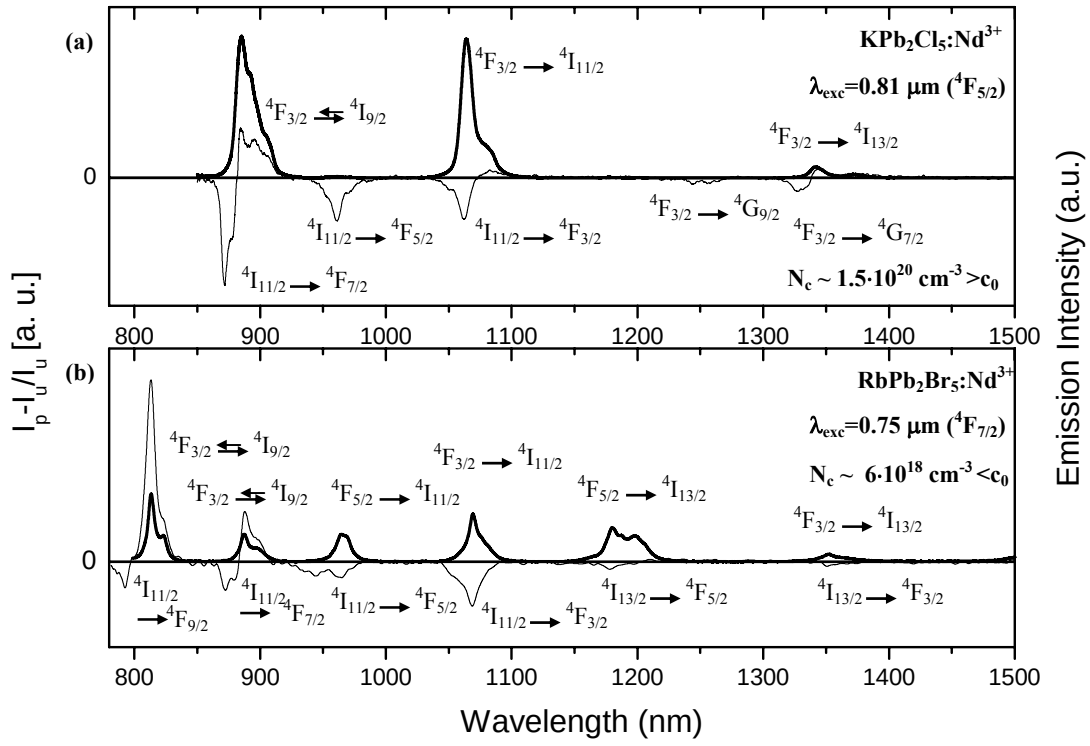

Fig. 3-29. *Emission spectra (thick line) and pump-probe spectra (thin line) of Nd^{3+}:KPb_2Cl_5 determined by pumping into the $^4F_{5/2}+^2H_{9/2}$ level (a) and Nd^{3+}:$RbPb_2Br_5$ determined by pumping into the $^4F_{7/2}+^4S_{3/2}$ level (b). Reabsorption and excited state absorption compete with gain as indicated. Depopulation via cross relaxation leads to less reabsorption of transitions from the $^4I_{13/2}$ level compared to the $^4I_{11/2}$ level in the case of Nd:KPC compared to Nd:RPB, due to the higher Nd concentration. (Note that the emission of Nd:RPB is not blackbody corrected.) The feature near 0.94 μm (b) could be due to the $^4I_{13/2}\rightarrow{}^4F_{9/2}$ transition. Note that only the main transitions are indicated (Table 3-10(b) shows others) and that the $^4F_{5/2}+^2H_{9/2}$ and $^4F_{7/2}+^4S_{3/2}$ levels are abbreviated by $^4F_{5/2}$ and $^4F_{7/2}$, respectively.*

The difference in the peak relation around 0.81 μm and 0.89 μm of Nd:KPB and Nd:RPB reflects e.g. higher absorption of the $^4I_{9/2}\rightarrow{}^4F_{5/2}+{}^2H_{9/2}$ versus the $^4I_{9/2}\rightarrow{}^4F_{3/2}$ transition in

Nd:RPB (section 3.2.1.1). The differences in the wavelength region 1150-1500 could possibly be explained by lower concentrations of Nd^{3+} in the sample used ($N_c \sim 6.3 \cdot 10^{18}$ $cm^{-3} << c_0$) leading to minimal cross relaxation and higher reabsorption from the $^4I_{13/2}$ level. Moreover, the line strengths for the cross relaxation processes in Nd:RPB are calculated to be slightly weaker than in Nd:KPB (Tab. 3-12). The line strenghts for the ESA transitions at ~ 1.45 μm ($^4F_{5/2}+ {}^2H_{9/2} \rightarrow {}^4G_{9/2}$) and 1.3 μm ($^4F_{3/2} \rightarrow {}^4G_{7/2}$) are weaker in Nd:RPB (Tab. 3-10(b)) than in Nd:KPB (Tab. 3-10(a)) while the line strengths for reabsorption are similar.

The spectra of a Nd:KPC crystal displayed in Figure 3-29(a) for the wavelength region 850-1500 nm are measured by pumping into the $^4F_{5/2}+{}^2H_{9/2}$ level. The Nd:KPC spectrum is comparable with the pump-probe spectrum of Nd:KPB in Figure 3-27(a), where the $^4F_{3/2}$ level is directly pumped. This is the case because the $^4F_{3/2}$ level is rapidly populated following 0.81 μm pumping for Nd:KPC. The missing ESA transition at ~ 1.45 μm ($^4F_{5/2}+{}^2H_{9/2} \rightarrow {}^4G_{9/2}$) in the chloride (in contrast to the bromide) can be explained by fast nonradiative decay from the $^4F_{5/2}+{}^2H_{9/2}$ level into the $^4F_{3/2}$ level (quantum efficiency ~ 0.013 for Nd:KPC [Nos01] due to the higher multiphonon decay rate). The missing reabsorption features from the $^4I_{13/2}$ is probably due to the high concentration of Nd^{3+} in the sample used in the experiments ($N_c \sim 1.5 \cdot 10^{20}$ $cm^{-3} > c_0$) leading to enhanced cross relaxation and depopulation of this level. The ratio of the negative feature and positive feature around 0.89 μm seem to be different if compared with Nd:KPB and Nd:RPB indicating probably higher reabsorption from the $^4I_{11/2}$ level. Also, the ratio of the reabsorption from the $^4I_{11/2} \rightarrow {}^4F_{3/2}$ transition versus the $^4I_{11/2} \rightarrow {}^4F_J$ transition (J=5/2 and 7/2) is reduced which could indicate that gain is competing more effectively against reabsorption at 1.07 μm in Nd:KPC. The positive signal at ~ 1.1 μm was not reproducible and it is not certain that it is actually due to gain. The positive pump-probe feature at 1.35 μm is likely due to net $^4F_{3/2} \rightarrow {}^4I_{13/2}$ gain, while the nearby negative band at 1.33 μm is the well-known $^4F_{3/2} \rightarrow {}^4G_{7/2}$ ESA. Finally, the 1.26 μm $^4F_{3/2} \rightarrow {}^4G_{9/2}$ band is observed, as was the case for direct pumping of the $^4F_{3/2}$ level for Nd:KPB.

Time resolved gain measurements were attempted with a pulsed pump source as described in section 2.2.6. Gain at 1.06 μm was observed for Nd^{3+}-doped hosts such as YAG due to the shorter lower laser level lifetime, while for chloride and bromide samples gain was expected over a short time period followed by a loss signal resulting from self-termination, which is also revealed by population dynamic studies from rate equation modelling of the levels discussed. At this point it is not clear which part of the observed signals are actually due to the expected behavior described above or due to effects such as thermal lensing and that is why it will not be further discussed in this study. In general, these time resolved

measurements would be very useful in order to explain the population dynamics and to study the influence of different rare earth ion concentrations on laser oscillation (regarding self-termination).

3.7 Upconversion Processes in Nd^{3+}-Doped KPb_2Br_5 Crystals

Bright upconversion fluorescence was observed in the bromide and chloride crystals which could also make short-wavelength lasing in these low-phonon energy materials possible. Previous upconversion studies on low-phonon energy materials doped with RE^{3+} ions such as Nd^{3+} can be found e.g. in Guedel *et al.* [Gue00], Balda *et al.* ([Bal01a], [Bal01b]), and Mendioroz *et al.* [Men04]. In this section first results on mainly infrared-to-visible upconversion spectroscopy of Nd^{3+} in the host crystal KPB by excitation into the $^4F_{3/2}$ level is briefly presented. Spectra determined by exciting the $^4F_{5/2}+^2H_{9/2}$ level revealing similar peaks in emission in the Nd:KPB crystal, has been measured by Prof. Alexandra Tkachuk and colleagues at the SI Vavilov State Optical Institute, St. Petersburg, Russia during collaborative upconversion studies on Nd:MPX (M= K, Rb; X= Cl, Br). The results are compared in publications no. 7 and no. 8.

By exciting the $^4F_{3/2}$ level with a Ti:Sapphire at 0.89 μm emission bands at ~ 0.44 μm, 0.48 μm, 0.54 μm, 0.60 μm, 0.64 μm, 0.67 μm, 0.69 μm, 0.72 μm, 0.76 μm, (0.79 μm), and 0.82 μm were detected (Fig. 3-30).

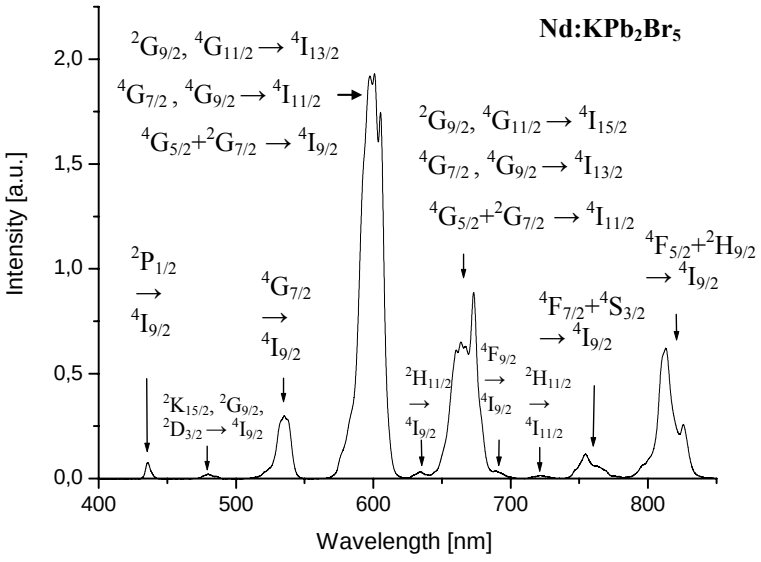

Fig. 3-30. *Uncorrected emission spectrum of a Nd^{3+}:KPb_2Br_5 crystal determined at room temperature by exciting the $^4F_{3/2}$ level at 0.89 μm. Note, that the emission of the displayed (possible) transitions can overlap with further bands resulting from transitions as shown in Fig. 3-31.*

The fluorescence bands result from transitions as indicated in the energy level diagram (Fig. 3-31). In this low-phonon energy host most of the levels are expected to show luminescence and therefore, some emissions result most probably from two or more transitions. Double exponential decays observed in emission lifetime measurements (section 2.2.5) at e.g. 0.75 µm under excitation of the $^4G_{5/2}+^2G_{7/2}$ level also lead to the assumption that some of them probably consist of more than one transition. Note, that transitions with small values for the calculated line strength of magnetic and induced electric dipole transitions and branching ratios smaller than 3% are not included (determined by Judd-Ofelt theory, section 1.2.2.1).

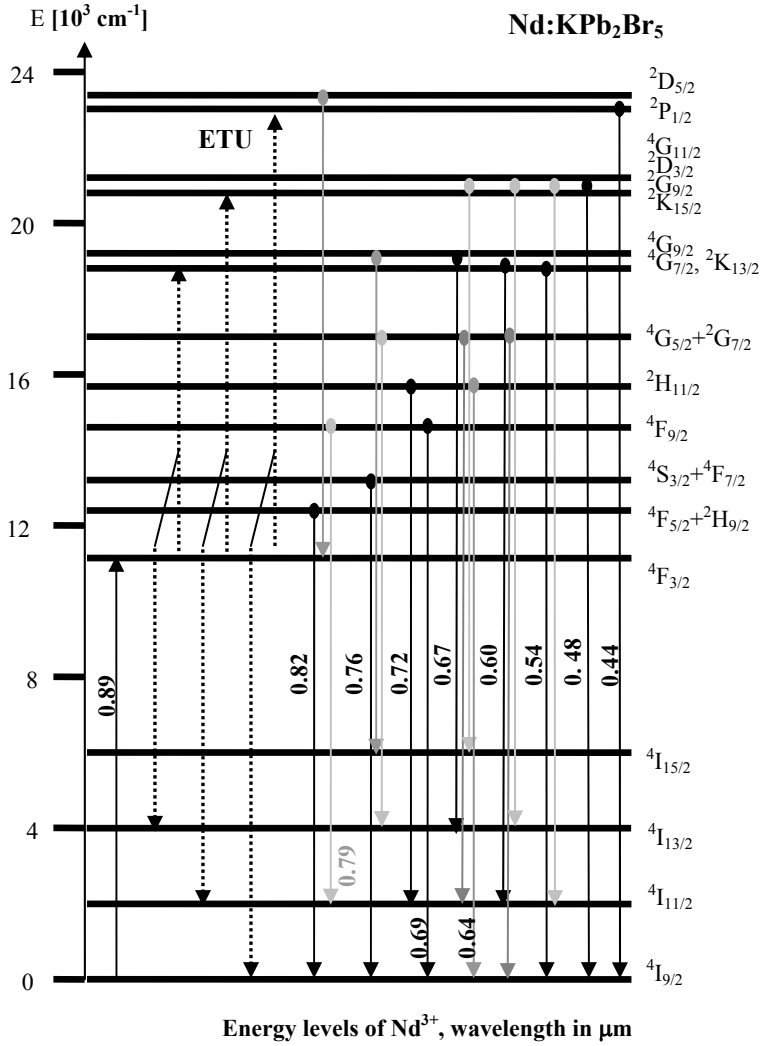

Fig. 3-31. *Energy level diagram of Nd:KPB displays the pumping and emitting levels of this study. Some possible energy transfer upconversion population mechansims after IR excitation are also indicated (dashed lines). For the upconverted emissions the $^4F_{3/2}$ level was pumped. The pumping levels under direct excitation are described in the text.*

The main (possible) transitions are indicated in Figure 3-30. For these transitions the strongest line strengths of induced electric and magnetic dipole transitions and branching ratios have been calculated. Note, that emission from the $^4F_{7/2}$+$^4S_{3/2}$ level was observed and therefore, the assumption of rapid nonradiative decay to the $^4F_{5/2}$+$^2H_{9/2}$ level in section 3.2.1.2 is not fully correct. A comparison with emission spectra under direct excitation identified the transition mainly responsible for the band 0.82 μm, and is further anticipated for other transitions. Absorption spectra (section 3.2.1.1, Fig. 3-4) were used to distinguish some bands. In Nd:KPC [Men04] and different Nd-doped glassy low-phonon host materials ([Bal01a], [Bal01b]) doped with Nd^{3+} the peaks at ~ 0.54 μm, 0.60 μm and 0.67 μm were ascribed to mainly result from emission of the $^4G_{7/2}$ level.

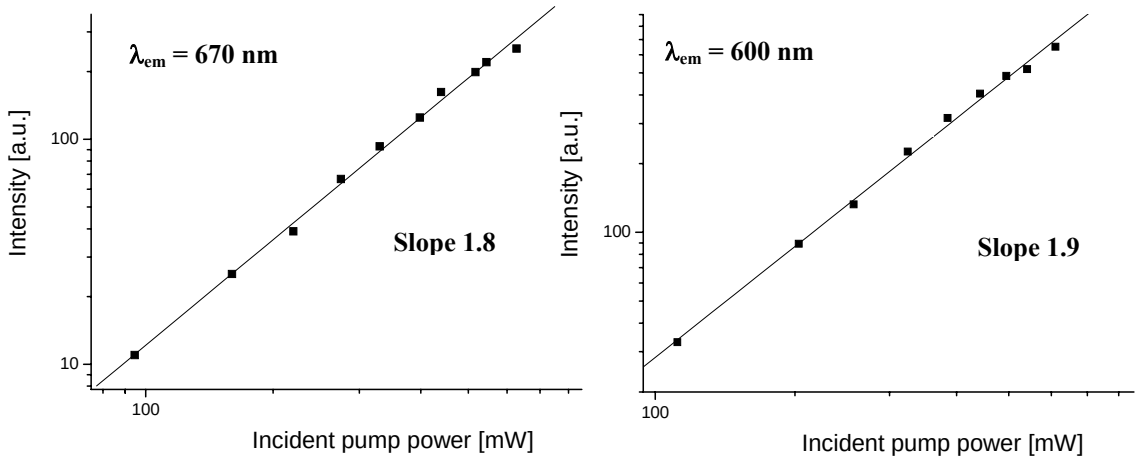

Fig. 3-32. *Emission intensity versus pump power for two emission wavelengths in Nd^{3+}:KPB: A nearly quadratic slope indicates a two step upconversion process.*

The emission intensity was measured versus incident pump power for the emission wavelengths 600 nm, 670 nm and 813 nm. A nearly quadratic slope indicates a two step upconversion process for the emission bands at ~ 600 nm and ~ 670 nm (Fig. 3-32). The slope measured at 813 nm (not shown) is with ~ 1.5 not quadratic which could be due to competing upconversion depopulation of the $^4F_{5/2}$+$^2H_{9/2}$ level (e.g. $^4G_{7/2}$←$^4F_{5/2}$+$^2H_{9/2}$, $^4F_{5/2}$+$^2H_{9/2}$→$^4I_{15/2}$). Excitation spectra (section 2.2.4) of the upconverted emissions at e.g. 600 nm were performed in spectral ranges which correspond to e.g. the $^4I_{9/2}$→$^4F_{3/2}$ transition. Similar peaks to the (one photon) absorption spectrum were revealed. Emission lifetimes under direct and upconverted (infrared excitation of the $^4F_{3/2}$ level) excitation of the emitting levels with an OPO as a pump source were obtained for Nd:KPB samples. This can help to reveal the mechanism responsible for the upconverted emission.

Disregarding the presence of photon avalanche [Cas90], there could be two mechanisms responsible for the population of the higher states: a) sequential absorption of photons in one ion involving excited state absorption (ESA, section 2.2.6 and 3.6) and/or b) energy transfer upconversion (ETU) (section 1.2.3). Some two step ETU processes with two Nd^{3+} ions in the $^4F_{3/2}$ level involved were suggested in the literature ([Bal01a], [Bal01b]) and are displayed in Figure 3-31. In the case of ESA, there should be an immediate decay after the infrared excitation since the ESA upconversion process should happen within the pump pulse width. Here, the decay time under upconversion excitation is expected to be similar to the emission lifetime under direct excitation. In the case of an ETU process, where two nearby ions interact a rise time and a decay time longer than under direct excitation is expected which depends both on the lifetime of the intermediate and upper level. By rate equation modelling ([Red83], [Chu96]), short lived upper levels are expected to decay approximately within half of the lifetime of the $^4F_{3/2}$ level. Here, the condition of a short pump pulse was fulfilled with a 10 ns pulse length of an OPO system.

For illustration, the emission lifetime detected at 535 nm shows under upconverted excitation a rise time of a few microseconds. Additionally, a decay time was observed which is with values up to ~ 50 µs closer to half of the lifetime of the $^4F_{3/2}$ level measured to be ~ 0.13-0.14 ms for the investigated samples in the same experimental setup. This is presumably longer than the lifetimes measured for the Nd:KPB samples under nearly direct excitation (into the $^4G_{9/2}$ level). They range from 9-12 µs for samples with concentrations of ~ 0.7-3.5 $x10^{19}$ cm^{-3}, which is much longer if compared with oxides and fluorides (70 ps in $Nd:Ca_5(PO_4)_3F$ - 41 ns in LaF_3 [Pay98]). For comparison a radiative lifetime of 16 µs was calulated for the $^4G_{7/2}$ level. This suggests an ETU mechanism such as $^4G_{7/2} \leftarrow {}^4F_{3/2}$, $^4F_{3/2} \rightarrow {}^4I_{13/2}$. A similar prolonged lifetime under upconverted excitation was observed at the emission wavelengths 0.60 µm and 0.67 µm. A two step ETU process for emission from the $^4G_{7/2}$ level was suggested for Nd-doped KPC crystals [Men04] as well as chalcohalide- and fluorarsenate glasses ([Bal01a], [Bal01b]). As shown further below the lifetime of the $^2P_{1/2}$ level is also close to half of the lifetime of the $^4F_{3/2}$ level and therefore, one could also assume that there are processes such as a two step process with GSA into the $^4F_{3/2}$ and ESA into the $^2P_{1/2}$ level involved which would decay within a similar time frame. However, the rise time of a few microseconds speaks against it. By excitation into the $^4G_{5/2}+{}^2G_{7/2}$ level the emission lifetimes at 0.60 µm and 0.67 µm were measured to be ~ 9 µs, which is close to the radiative lifetime of ~ 14 µs for the combined level calculated in the high temperature limit. Since the lifetimes of the upper levels are calculated (and measured) to be in most cases very similar it

is difficult to determine at this point of this study from which levels the upconverted emission at 0.60 μm and 0.67 μm mainly occurs.

(Phonon-assisted) ETU and/or ESA processes are suggested to populate the $^2P_{1/2}$ level for different low-phonon energy host materials such as KPC [Men04] and chalcohalide glasses [Bal01a]. The emission lifetime measured at 435 nm under direct excitation matches with 53 μs the calculated radiative lifetime of 52 μs for the $^2P_{1/2}$ level. Under upconverted excitation the emission lifetime seems to have a rise time. However, further spectroscopic investigations are needed to determine the process. Also, the measurement of the pump power dependence could reveal if there are two-step processes or even a process of higher step order present.

In general, it should also be noted, that the energy mismatch for an ESA and/or ETU two step upconversion process is quite high. For illustration, approximately ~ 400 cm^{-1} were calculated between the $^4F_{3/2}$-$^2P_{1/2}$ gap (Appendix D) and the pump wavelength of 0.89 μm, which would involve ~ 2-3 phonons to bridge this difference in these low-phonon energy hosts.

Gain could be observed in first upconversion laser experiments at 0.67 μm and 0.60 μm by pumping into the $^4F_{3/2}$ level at 0.89 μm with an OPO system as a pump source. These experiments will be continued as soon as further Nd-doped samples of suitable crystal quality become available. Higher dopant concentration would be useful to increase possible ETU processes. However, if the $^4I_{11/2}$ level is considered as the lower laser level it should also be noted that higher dopant concentration could increase the population of the $^4I_{11/2}$ level due to depopulation of the $4I_J$ levels (J=13/2, 15/2) by cross-relaxation (section 3.6).

4. Summary and Outlook

In the course of this study the first two existing moisture-resistant bromide laser host crystals of low-phonon energy doped with the rare earth ions Nd^{3+}, Eu^{3+} and Tb^{3+}, respectively, were identified, grown, and studied: potassium-lead-bromide (KPb_2Br_5, KPB) and rubidium-lead-bromide ($RbPb_2Br_5$, RPB). Here, the main focus was on the spectroscopic investigation and laser experiments with respect to determining their laser potential. Preparational aspects including crystal growth by the Bridgman technique and physical properties of these single crystalline materials were carried out under collaborative efforts and also herein presented.

Low-Phonon Energies

Raman scattering spectra (and IR-cutoff measurements) of the KPB and RPB crystals revealed very low-phonon energies with maximum peak values of ~ 140 cm^{-1} compared to e.g. their chloride analogs with values of ~ 200 cm^{-1}. This change is predicted based on the reduced masses of bromide and chloride ions. The similar maximum phonon energies of KPC and RPC as well as of KPB and RPB confirm that the different halogen anions mainly cause the change in the maximum phonon energies. As a result, the nonradiative decay due to multiphonon relaxation is reduced in the bromides if compared with the chloride analogs which is reflected by the spectroscopic results and a condition for the (achieved) laser operation at new wavelengths herein.

Slow Nonradiative Decay

This study included absorption spectra, emission spectra, emission lifetimes recorded for Nd^{3+}-, Tb^{3+}- and partly Eu^{3+}-doped MPB (M=Rb, K) samples at room temperature as well as calculations of cross sections, Judd-Ofelt parameters, radiative transition probabilities for relevant (laser) transitions, and multiphonon decay rates. The calculated radiative lifetimes and branching ratios were compared with experimentally determined values. As expected higher quantum yields have been observed in the bromide host crystals compared to the KPC host crystal for transitions from the $^4F_{5/2}+^2H_{9/2}$ level into the ^4I levels in Nd:MPB (M= K, Rb) with values of ~ 50-70 %, as well as for LWIR emission amongst the ^7F levels in Tb:KPB (Fig. 4-1) with values as noted below. The higher emission rates emanating e.g. from the $^4F_{5/2}+^2H_{9/2}$ level (Fig. 4-2) in Nd:MPB (M= K, Rb) are encouraging for possible laser activity at new wavelengths especially in the LWIR region. The significantly higher Ω_2 value in Nd:KPB compared to Nd:RPB is caused by the different crystal structures of these two materials and reflects the hypersensitive nature of the $^4G_{5/2}+^2G_{7/2}$ band in Nd:KPB, which could be advantageous for certain laser transitions. Directly pumpable, broadband 8 μm

emission due to the $^7F_4 \rightarrow {}^7F_5$ transition was observed for the first time in a crystal in addition to broadband 3 μm and 5 μm emission in Tb:KPB samples with quantum efficiencies up to 3 % for emission resulting from the $^7F_4$ level and up to 64 % for emission resulting from the $^7F_5$ level (Fig. 4-1). The $^7F_5 \rightarrow {}^7F_3$ transition could be advantageous for the 8 μm emission because of repopulation of the upper laser level (and depopulation of the lower laser level) via an Auger upconversion process. Low multiphonon decay rates were determined for different energy gaps in the rare earth-doped bromides after the energy gap law and compared with other host crystals. Future detailed work on emission from energy levels of rare earth ions with even smaller gaps to the next lower level like $^4F_{7/2}+{}^4S_{3/2}$ in Nd^{3+} (Fig. 4-2) can be feasible, also to determine which portion of the measured nonradiative relaxation is truely due to multiphonon decay.

Temperature Dependent Quenching

It was shown, that taking the maximum peak value of the highest Raman energy phonon band can be a first approximation for calculating the number of phonons involved in the process in order to determine the nonradiative rates in these materials. However, as evidenced from temperature dependent lifetime measurements of the long wavelength emitting levels in Tb^{3+}-doped KPB samples, a maximum phonon energy value of 160 cm^{-1} taken from the wing of the Raman spectrum is the best fit representation of the effective phonon energy. In this context multiphonon fitting parameters characteristic for the host material were obtained to be χ_{KPB} = $1.70 \cdot 10^{-2}$ cm and $C = 3.27 \cdot 10^9$ s^{-1}. Emission resulting from the $^7F_3$ level in Tb:KPB was detected, which makes 10 μm emission promising (Fig. 4-1). In addition approximate values for emission lifetimes of the $^7F_3$ level, the $^7F_3$-$^7F_4$ energy gap, and number of phonons involved in the transition were predicted. Emission lifetime studies of Tb:KPB samples of different concentration and purity revealed also that there are other quenching mechanisms beside multiphonon

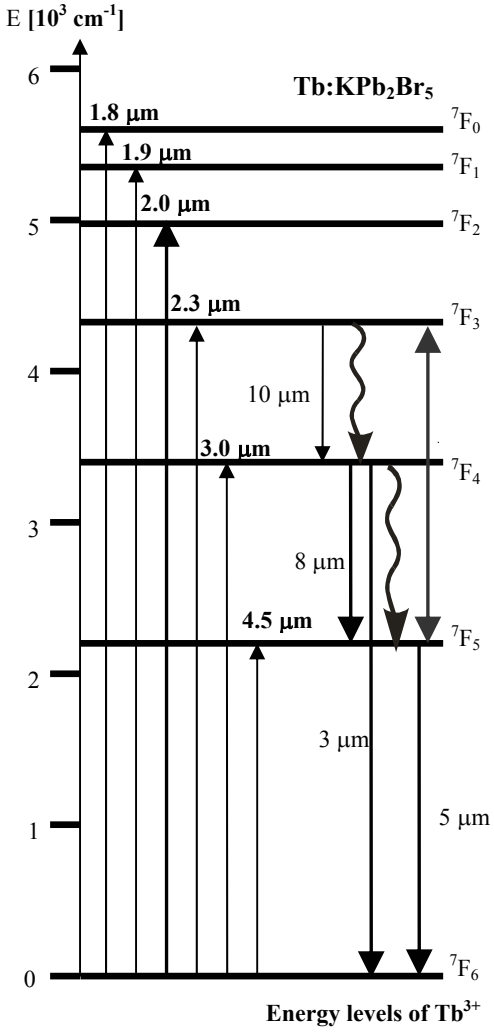

***Fig. 4-1**. Energy level diagram of Tb:KPB displays the possibility of direct pumping of long-wavelength transitions.*

decay involved. The variation in lifetime among the samples is likely due to energy transfer e.g. to neighboring Tb^{3+} ions, defects and/or impurities such as NH_4^+. It appears as if this quenching is partly mediated by the rare earth ion concentration via the migration-enhanced energy-transfer mechanism.

Low Temperature Spectroscopy for Nd^{3+}-doped KPB

This study included transmission, excitation and emission measurements. A main result was the determination of Stark levels in between ~ 0-28100 cm^{-1}. Measurements on Nd:RPB as well as for the Tb^{3+}- and Eu^{3+}-doped crystals would be useful.

Laser Activity in Nd:MPB (M= K, Rb) Crystals at Room Temperature

For the first time laser operation has been achieved in moisture-resistant bromide host crystals of low-phonon energy, also emitting at new wavelengths. Conventional laser activity at 1.07 μm was achieved in Nd^{3+}-doped KPB and RPB by directly pumping into the $^4F_{3/2}$ level with slope efficiencies of up to 17%. Laser operation at the new wavelengths 1.18 μm and 0.97 μm resulting from the $^4F_{5/2}+^2H_{9/2}\rightarrow{}^4I_J$ transition (J=13/2 and 11/2) was achieved in Nd:RPB for the first time in any solid state laser material (Fig. 4-2). An OPO system was used to directly pump the upper laser level by taking into account the strong dependence of absorption on polarization observed for the Nd:RPB crystal. The slope efficiency at 1.18 μm was determined to be 3.1 %. However, the accumulation of population in the lower long lived laser level favors pulsed operation over the cw mode in these crystals, if there are no processes involved which could depopulate the lower laser levels.

Optical Pump-Probe Processes and Depopulation Mechanisms of the Lower Laser Levels in Nd^{3+}-Doped KPB, RPB, and KPC

Cw pump-probe spectra and emission spectra were determined for Nd:KPB, Nd:RPB and Nd:KPC ranging from 780 – 1550 nm by pumping into the $^4F_{3/2}$, $^4F_{5/2}+^2H_{9/2}$ and $^4F_{7/2}+^4S_{3/2}$ levels (Fig. 4-2), respectively in order to gain further insights into the lasing potential of Nd^{3+} in these crystals. Cw pump-probe spectra were presented in order to discuss excited state absorption (ESA) and reabsorption processes (RA) due to the long lived lower laser levels, as well as e.g. $^4I_{13/2}$ depopulation mechanisms feasible for more efficient laser operation. Some of the transitions are indicated in Figure 4-2. Calculated and measured lifetimes were reported for the most important initial levels discussed in this study. Line strengths and effective cross sections of ESA and RA transitions competing with the (laser) emission transitions, as well as of cross relaxation (CR) processes among the lower laser levels, were given. ESA transitions were identified and their occurrence only under certain pump wavelengths was noted. ESA influencing the $^4F_{5/2}+^2H_{9/2}\rightarrow{}^4I_{13/2}$ was not directly observed even though it is predicted.

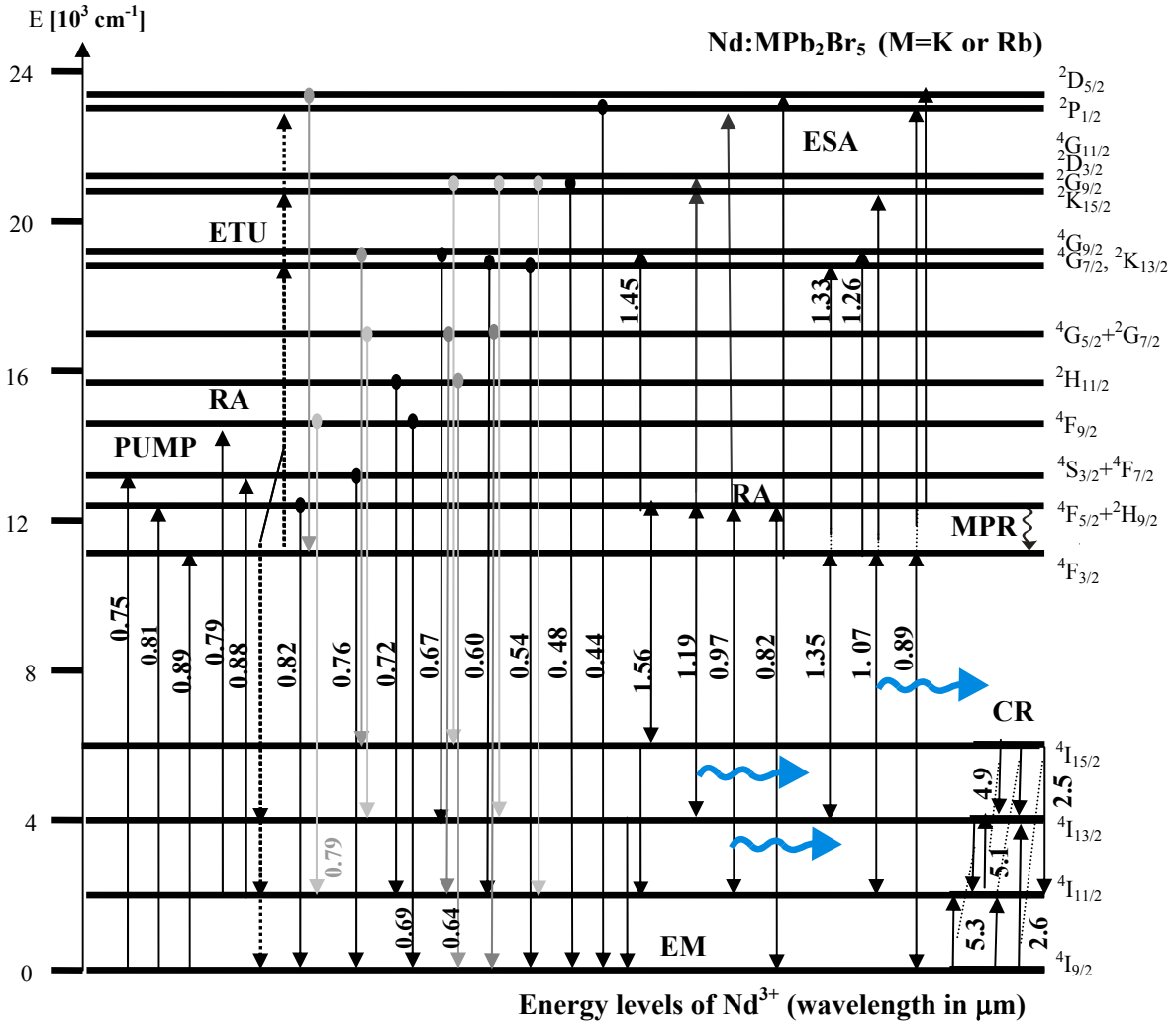

Fig. 4-2. *For illustration, the energy level diagram of Nd:MPB (M= K or Rb) displays some pumping and emitting (EM) levels of this study. Laser activity (⇝) was shown for the first time in moisture-resistant, bromide host crystals of low-phonon energy, also at new wavelengths (in Nd:RPB) for the first time in any crystal. Some of the discussed transitions based on processes such as excited state absorption (ESA), energy transfer upconversion (ETU), cross relaxation (CR), reabsorption (RA), and multiphonon relaxation (MPR) are also indicated.*

Net cw gain was observed at the laser wavelength 1.18 µm for Nd:KPB in contrast to the reabsorption features at the laser wavelengths 1.07 µm and at 0.97 µm. In contrast, no gain was observed at 1.18 µm for Nd:KPC due to fast relaxation out of the $^4F_{5/2}+^2H_{9/2}$ level, nor for Nd:RPB due to low Nd concentration and thus, absence of significant cross relaxation of the $^4I_{13/2}$ lower laser level. The ratio of reabsorption transitions emanating from the $^4I_{13/2}$ and $^4I_{11/2}$ levels proved that the $^4I_{13/2}$ population is reduced compared to the $^4I_{11/2}$ level population, which is likely due to cross relaxation and/or radiative processes. The investigation of crystals of different Nd dopant concentrations suggest that the $^4I_{13/2}$ lower laser level depopulation occurs via cross relaxation leading to less reabsorption of transitions from the $^4I_{13/2}$ level compared to the $^4I_{11/2}$; as a result, the $^4F_{5/2}+ {}^2H_{9/2} \rightarrow {}^4I_{13/2}$ transition is more favorable for

efficient laser operation at 1.18 μm for longer pulses or maybe even cw pumping at high Nd concentration. Gain resulting from the $^4F_{3/2} \rightarrow {}^4I_{13/2}$ transition at ~1.35 μm is observed if the $^4I_{13/2}$ level is rapidly depopulated by cross relaxation (and the $^4F_{3/2}$ level is directly pumped in the bromide crystals). In future studies the follow up of gain measurements involving a pulsed pump source would be useful in order to explain the population dynamics and to study the influence of different rare earth ion concentrations on laser oscillation in more detail.

Upconversion

Bright upconversion fluorescence was observed in the neodymium-doped crystals which could enable short-wavelength lasing. By exciting the $^4F_{3/2}$ level at 0.89 μm emission bands at 0.44 μm, 0.48 μm, 0.54 μm, 0.60 μm, 0.64 μm, 0.67 μm, 0.72 μm, 0.75 μm, (0.79 μm), and 0.82 μm in Nd^{3+}:KPB were measured. Possible transitions were identified. Slope measurements of the emission intensity versus pump power and emission lifetime measurements suggest e.g. two step energy transfer upconversion (ETU) processes where two Nd^{3+} ions in the $^4F_{3/2}$ level are involved (Fig. 4-2). Gain could be observed in first upconversion laser experiments at 0.67 μm and 0.60 μm.

Summary Statement

In particular the low-phonon energy, moisture-resistance, wide transmission range, broadband luminescence features in the long wavelength region as well as the potential to incorporate rare earth ions render these actively-doped alkali-lead-halide compounds especially useful as practical solid state materials lasing at new wavelengths, e.g. in the LWIR region. Those (tunable) sources would be beneficial for e.g. remote sensing in the vibrational fingerprint region, thermal scene illumination, and infrared spectroscopy in clinical and diagnostic analysis. Furthermore, the fabrication of waveguides and fibers (as described for silver halide crystals [Dek01], [San98]) made of these low-phonon energy materials of high refractive index can be interesting as integrated optical elements, especially in the LWIR region. These could be used as detectors, small chemical sensors for surface sensitive spectroscopy, thin film sources, modulators, etc. Different A, B and X ions can be tested in the AB_2X_5 compound family ([Bec86a], [Bec86b]) in order to identify further host materials and to study the influence of the different participating ions on the phonon energies in detail. Mixtures of bromides with iodides or chlorides could be feasible in order to maybe incorporate even higher concentrations of the active dopant ion and especially, to achieve even lower phonon energies.

References

[Alm04] Almaz Optics, Inc., www.almazoptics.com (2004)

[Aul82] B.F. Aull, H.P. Jenssen, *Vibronic interactions in Nd:YAG resulting in nonreciprocity of absorption and stimulated emission cross sections*, IEEE J. Quant. Electr. **QE-18**, no. 5, 925-930 (1982)

[Auz76] F. Auzel, *Multiphonon-assisted anti-stokes and stokes fluorescence of triply ionized rare earth ions*, Phys. Rev. B **13**, no. 7, 2809- 2817 (1976)

[Bal01a] R. Balda, M. Sanz, A. Mendioroz, J. Fernandez, L.S. Griscom, J.-L. Adam, *Infrared-to-visible upconversion in Nd^{3+}-doped chalcohalide glasses*, Phys. Rev. B **64**, 144101-1-8 (2001)

[Bal01b] R. Balda, L.M. Lacha, A. Mendioroz, M. Sanz, J. Fernandez, J.-L. Adam, M.A. Arriandiaga, *Upconversion processes in Nd^{3+}-doped fluorarsenate glasses*, J. Alloys and Comp. **323-324**, 255-259 (2001)

[Bal02] R. Balda, M. Voda, M. Al-Saleh, J. Fernandez, *Visible luminescence in $KPb_2Cl_5:Pr^{3+}$ crystal*, J. Lum. **97**, 190-197 (2002)

[Bal03a] R. Balda, J. Fernandez, A. Mendioroz, M. Voda, M. Al-Saleh, *Infrared to visible upconversion in Pr^{3+}-doped KPb_2Cl_5 crystal*, Opt. Mat. **24**, 91-95 (2003)

[Bal03b] R. Balda, J. Fernandez, A. Mendioroz, M. Voda, , M. Al-Saleh, *Infrared to visible upconversion processes in Pr^{3+}/Yb^{3+}-codoped potassium lead chloride crystal*, Phys. Rev. B **68**, 165101-1-7 (2003)

[Bas02] T.T. Basiev, Y.U. Orlovskii, B.I. Galagan, M.E. Doroshenko, I.N. Vorobèv, L.N. Dmitruk, A.G. Papashvili, V.N. Skvortsov, V.A. Konyushkin, K.K. Pukhov, G.A. Ermakov, V.V. Osiko, A.M. Prokhorov, S. Smith, *Evaluation of rare earth-doped crystals and glasses for 4-5 μm lasing*, Las. Phys. **12**, no. 5, 859-877 (2002)

[Bas05] T.T. Basiev, M.E. Doroshenko, V.V. Osiko, D.V. Badikov, *Mid IR laser oscillations in new low phonon $PbGa_2S_4:Dy^{3+}$ crystal,* Advanced Solid State Photonics, OSA TOPS 20, TuB10, Opt. Soc. Am. (2005)

[Bea90] R. Beach, M.D. Shinn, L.Davis, R.W. Solarz, W.F. Krupke, *Optical absorption and stimulated emission of neodymium in Yttrium Orthosilicate*, IEEE J. Q. Electr. **26**, no. 8, 1405-1412 (1990)

[Bec03] M. Beck, D. Hofstetter, T. Aellen, S. Blaser, J. Faist, U. Oesterle, E. Gini, *Continuous wave operation of quantum cascade lasers*, J. Cryst. Growth **251**, 697-700 (2003)

[Bec86a] H.P. Beck, G. Clique, and H. Nau, *A Study on AB_2X_5 Compounds (A: K, In, Tl; B: Sr, Sn, Pb; X: Cl, Br, I)*, Z. anorg. Allg. Chem. **536**, 35-44 (1986)

[Bec86b] H.P. Beck, *A study on AB_2X_5 compounds. II refinement of the structures of $InSn_2Br_5$ and $InSn_2I_5$,* Z. anorg. Allg. Chem. **536**, 45-52 (1986)

[Bel73] R.F. Belt, J.P. Moss, *Growth striae in single crystals of gadoulinium gallium garnet*, Mat. Res. Bull. **8**, 1197-1204 (1973)

[Ben78] J.M. Benett, H.E. Bennett, *Polarization* in Handbook of Optics, W.G. Driscoll (ed.), W. Vaughan (asc. ed.), Optical Society of America, McGraw-Hill book company, New York, 10 (1978)

[Bib95] C. Bibeau, *Evaluation of the $^4I_{11/2}$ terminal level lifetime for several neodymium-doped laser crystals and glasses*, Ph.D. thesis, University of California, Davis (1995)

[Bor27] M. Born und R. Oppenheimer, *Zur Quantentheorie der Molekeln*, Ann. Physik., 4th part, **84**, 457-484 (1927)

[Bow01] S.R. Bowman, S.K. Searles, N.W. Jenkins, S.B. Qadri, E.F. Skelton, J. Ganem, *New mid-IR laser based on an erbium activated low-phonon energy crystal*, Technical Digest of conference on Lasers and Electro-Optics CLEO 2001, Baltimore, Maryland, USA, 557-558 (2001)

[Bow96] S.R. Bowman, L.B. Shaw, B.J. Feldman, J. Ganem, *A 7-μm praseodymium-based solid-state laser*, IEEE J. Quantum Electron. **32**, no. 4, 646-649 (1996)

[Bri86] J.C. Brice, *Crystal growth processes*, Blackie&Son Ltd., Halsted Press (1986)

[Bur72] A.I. Burshtein, *Hopping mechanism of energy transfer*, Sov. Phys. JETP **35**, 882-885 (1972)

[Bur85] A.I. Burshtein, *Energy transfer kinetics in disordered systems*, J. Lum. **34**, 167-188 (1985)

[But02] L.N. Butvina, E.M. Dianov, A.G. Okhrimchuk, N.V. Lichkova, V.N. Zavgorodnev, *The MIR spectroscopy of Tb^{3+}-doped low-phonon crystals and polycrystalline fibers*, Proc. SPIE **4766**, 37-42 (2002)

[Cai91] J.A. Caird, A.J. Ramponi, P.R. Staver, *Quantum efficiency and excited-state relaxation dynamics in neodymium-doped phosphate laser glasses*, J.Opt. Soc. Am. B. **8**, 1391-1403 (1991)

[Car77] W.T. Carnall, H. Crosswhite, H.M. Crosswhite, *Energy level structure and transition probabilities of trivalent lanthanides in LaF_3*, Chem. Divison, Argonne National Laboratory (1977)

[Car79] W.T. Carnall, *Handbook on the physics and chemistry of rare earths*, K.A. Gschneidner, L. Eyring (eds.), North Holland, Amsterdam, 3, (1979)

[Cas67] H.H. Caspers, H.E. Rast, H.R. Marlin, *Solid state spectroscopy: optical spectrum of EuF_3*, H.H. Caspers, R.L. Conger, R.H. Marlin, D.E. McCarthy, A. Nedoluha (eds.), Naval Ordnance Laboratory Report 705, Corona, CA (1967)

[Cas90] W.E. Case, M.E. Koch, A.W. Kueny, *The photon avalanche in rare earth crystals*, J. Lum. **45**, 351-353 (1990)

[Chu96] T. Chuang, H.R. Verdun, *Energy transfer up-conversion and excited state absorption of laser radiation in Nd:YLF laser crystals*, IEEE J. Quant. Electr. **32**, no. 1, 79-91 (1996)

[Coc92] N.J. Cockroft, G.D. Jones, D.C. Nguyen, *Dynamics and spectroscopy of infrared-to-visible upconversion in erbium-doped cesium cadmium bromide ($CsCdBr_3:Er^{3+}$)*, Phys. Rev. B **45**, no. 10, 5187-5198 (1992)

[Col71] M. Cola, V. Massarotti, R. Riccardi, and C. Sinistri, *Binary systems formed by lead bromide with (Li, Na, K, Rb, Cs and Tl)Br: a DTA and diffractometric study*, Z. Naturforsch. **26 a**, 1328-1332 (1971)

[Con70] E.U. Condon, G.H. Shortley, *The theory of atomic spectra,* University Press, Cambridge 1970

[Crc82] CRC Handbook of Chemistry and Physics, 63rd edition, R.C. Weast, M.J. Astle, F-216, CRC Press, Florida (1982)

[Cze02] C. Czeranowsky, *Resonatorinterne Frequenzverdopplung von diodengepumpten Neodym-Lasern mit hohen Ausgangsleistungen im blauen Spektralbereich*, PhD thesis, University of Hamburg (2002)

[Dek01] B. Dekel, Z. Barkay, A. Katzir, *The study of waveguides made by diffusion of Br into AgCl substrates and the transmission of mid-IR radiation through these waveguides*, Opt. Comm. 199, 383-388 (2001)

[Dek02] B. Dekel, A. Katzir, *Mid-infrared diffused planar waveguides made of silver halide chloro-bromide*, Appl. Opt. **41**, no. 18, 3622-3627 (2002)

[Dem02] R. Demirbilek, J. Heber, S.L. Nikitin, *Charge transfer and $4f^n$-$4f^{n-1}5d$ transitions of trivalent rare earth ions in $CsCdBr_3$*, XI Feovilov Symposium of crystals activated by rare earth and transition metal ions, A.A. Kaplyanskii, B.Z. Malikn, S.I. Nikitin (eds.), Proc. SPIE **4766** (2002)

[Dex53] D.L. Dexter, *A theory of sensitized luminescence in solids*, J. Chem. Phys. **21**, 836-850 (1953)

[Die68] G.H. Dieke, *Spectra and energy levels of rare earth ions in crystals*, Interscience Publishers, John Wiley&Sons, New York 1968

[Fai94] J. Faist, F. Capasso, D.L. Sivco, C. Sirtori, A.L. Hutchinson, A.Y. Cho, *Quantum cascade laser*, Science **264**, 553-556 (1994)

[Fan59] U. Fano, G. Racah, *Irreducible tensioral sets*, Academic Press Inc., New York (1959)

[Foe48] T. Foerster, *Zwischenmolekulare Energiewanderung und Fluoreszenz*, Ann. Phys. **2**, 55-75 (1948)

[For98] L. Fornasiero, S. Kueck, T. Jensen, G. Huber, B.H.T. Chai, *Excited state absorption and stiumlated emission of Nd^{3+} in crystals. Part II: YVO_4, $GdVO_4$, $Sr_5(PO_4)_3F$*, Appl. Phys. B **67**, 549-553 (1998)

[For99] L. Fornasiero, T. Kellner, S. Kueck, J.P. Meyn, P.E.-A. Moebert, G. Huber, *Excited state absorption and stimulated emission of Nd^{3+} in crystals III: $LaSc_3(BO_3)_4$, $CaWO_4$, $YLiF_4$*, Appl. Phys. B **68**, 67-72 (1999)

[Gab85] A. Gabriel, A.D. Pelton, *Phase diagram measurements and thermodynamic analysis of the $PbCl_2$-NaCl, $PbCl_2$-KCl, and $PbCl_2$-KCl-NaCl systems.*, Can. J. Chem. **63**, no. 11, 3276-3282 (1985)

[Gan02] J. Ganem, J. Crawford, P. Schmidt, N.W. Jenkins, S.R. Bowman, *Thulium cross-relaxation in a low-phonon energy crystalline host*, Phys. Rev. B **66**, 245101-1-15 (2002)

[Goe98] C. Goerller-Walrand, K. Binnemans, *Spectral intensities of f-f transitions*, Handbook on the physics and chemistry of rare earths **25**, 167, K.A. Gschneidner, L. Eyring (ed.), Elsevier Science B.V. (1998)

[Gru89] J.B. Gruber, M.E. Hills, R.M. Macfarlane, C.A. Morrison, G.A. Turner, G.J. Quarles, G.J. Kintz, L. Esterowitz, *Spectra and energy levels of Tm^{3+}:$Y_3Al_50_{12}$*, Phys. Rev. B, **40**, 14, 9464-9478 (1989)

[Gue00] H.U. Guedel, M. Pollnau, *Near-infrared to visible photon upconversion processes in lanthanide-doped chloride, bromide and iodide lattices*, J. All. Comp. **303-304**, 307-315 (2000)

[Hah95] T. Hahn, *International Tables for Crystallography, Volume A: Space-Group Symmetry*, 4th edn., Published for the International Union of Crystallography by Kluwer Academic Publishers, Dordrecht-Boston-London (1995)

[Heh94] M.P. Hehlen, K. Kraemer, H.U. Guedel, R.A. McFarlane, R.N. Schwartz, *Upconversion in Er^{3+}-dimer systems: Trends within the series $Cs_3Er_2X_9$ (X= Cl, Br, I)*, Phys. Rev. B **49**, 12475-12484 (1994)

[Hen74] D.E. Henrie, B.K. Henrie, *Oscillator strengths of f-f transitions in hexachloroneodym(III) anion*, J. Inorg. Nucl. Chem. 36, 2125-2128 (1974)

[Hen89] B. Henderson and G.F. Imbusch, *Optical spectroscopy of inorganic solids*, Clarendon Press, Oxford 1989

[Hit00] Ontar Corporation, High-resolution transmission molecular absorption (Hitran) database, www.ontar.com/Software/product_HITRANDatabase.htm or http://cfa-www.harvard.edu/hitran// (2000)

[Hoe04] U. Hoemmerich, E. Nyein, S.B. Trivedi, *Crystal growth, upconversion, and emission properties of Er^{3+}-, and Nd^{3+}-doped KPb_2Br_5*, CLEO, San Francisco, CA, USA (2004)

[Hoe05] U. Hoemmerich, E. Nyein, S.B. Trivedi, *Crystal growth, upconverssion, and infrared emission properties of Er^{3+}-doped KPb_2Br_5*, J. Lumin., in press, (2005)

[Höf79] O. Höfling, *Physik,* Vol. II, part 3: Quanten und Atome, 12th ed., Ferd. Dümmlers Verlag, Bonn 1979

[Hub88] G. Huber, E.W. Duczynski, K. Petermann, *Laser pumping of Ho-, Tm-, Er-doped garnet lasers at room temperature*, IEEE J. Quant. Electr. **24**, no. 6, 920-923 (1988)

[ISA96] Instruments S.A., Inc., *Fluorolog-3, Operation and Maintenance Manual*, 1996

[Isa98] L.I. Isaenko, A.P. Yelisseyev, V.A. Nadolinny, V.I. Pashkov, M.C. Nostrand, R.H. Page, S.A. Payne, R. Solarz, *Spectroscopic investigation of rare earth-doped chloride single crystals for telecommunication amplifiers*, Solid State Lasers VII, R. Scheps (ed.), Proc. SPIE **3265**, 242-249 (1998)

[Jan68] P.W.J. Jansen, *The unit cell dimensions of some alkali lead and alkali strontium halides*, Rec. Trav. Chim. **87**, 1021-1024 (1968)

[Jen01] N.W. Jenkins, S.R. Bowman, *Lifetime measurements for a potential neodymium 5-μm Laser*, Technical Digest of conference on Lasers and Electro-Optics CLEO 2001, Baltimore, Maryland, USA, 280-281 (2001)

[Jen02] N.W. Jenkins, S.R. Bowman, L.B. Shaw, J.R. Lindle, *Spectroscopic analysis and laser modelling of neodymium-doped potassium lead chloride*, J. Lum. **97**, 127-134 (2002)

[Jen03] N.W. Jenkins, S.R. Bowman, S. O'Connor, S.K. Searles, J. Ganem, *Spectroscopic characterization of Er-doped KPb_2Cl_5 laser crystals*, Opt. Mat. **22**, no. 4, 311-320 (2003)

[Jos72] B.D. Joshi, B.M. Patel, A.G. Page, T.R. Bangia, R.N. Saxena, *Energy levels of Tb^{3+} in $LaBr_3$*, Bhabha Atomic Research Centre, Bombay, India 1972

[Jos77] B.D. Joshi, A.G. Page, *Fluorescence and absorption spectra of Tb^{3+} ions in Yttrium-Gallium Garnet*, J. Lum. 15, 29-34 (1977)

[Jud62] B.R. Judd, *Optical absorption intensities of rare earth ions*, Phys. Rev. **127**, no. 3, 750-761 (1962)

[Jud63] B.R. Judd, *Operator techniques in atomic spectroscopy*, McGraw-Hill Book Company, New York (1963)

[Kam90] A.A. Kaminskii, *Laser crystals, their physics and properties*, 2. Aufl., Springer Verlag, Berlin-Heidelberg (1990)

[Kam96] A.A. Kaminskii, *Crystalline lasers: physical processes and operating schemes*, CRC Press, New York (1996)

[Kie62] A. Kiel, *The interaction of paramagnetic ions with lattice vibrations, Ph.D. thesis*, Johns Hopkins University, Baltimore, MD (1962)

[Kie63] A. Kiel, *Multiphonon spontaneous emission in paramagnetic crystals*, Quant. Electr. proceedings of the third international congress, P. Grivet and N. Bloembergen (eds.), Columbia University Press, New York, 765-772 (1963)

[Kob80] T. Kobayasi, S. Mroczkowski, J.F. Owen, L. Brixner, *Fluorescence lifetime and quantum efficiency for 5d-4f transitions in Eu^{2+}-doped chloride and fluoride crystals*, J. Lum. **21**, 247-257 (1980)

[Koe95] J. Koetke, G. Huber, *Infrared excited-state absorption and stimulated-emission cross sections of Er^{3+}-doped crystals*, Appl. Phys. B **61**, 151-158 (1995)

[Kor04] Korth Kristalle GmbH, www.korth.de, 2004

[Kru65] W.F. Krupke, J.B. Gruber, *Optical-absorption intensities of rare earth ions in crystals: the absorption spectrum of thulium ethyl sulfate* , Phys. Rev. **139**, no. 6, A2008-A2016 (1965)

[Kru66] W.F. Krupke, *Optical absorption and fluorescence intensities in several rare earth-doped Y_2O_3 and LaF_3 single crystals*, Phys. Rev. **145**, no. 1, 325-337 (1966)

[Kru71] W.F. Krupke, *Radiative transition probabilities within the $4f^3$ ground configuration of Nd:YAG*, IEEE J. Quantum Electron. **QE-7**, 153-159 (1971)

[Kru74] W.F. Krupke, *Induced-emission cross sections in neodymium laser glasses*, IEEE J. Quantum Electron. **QE-10**, no. 4, 450-457 (1974)

[Kue98] S. Kueck, L. Fornasiero, E. Mix, G. Huber, *Excited state absorption and stimulated emission of Nd^{3+} in crystals. Part I: $Y_3Al_5O_{12}$, $YAlO_3$, and Y_2O_3*, Appl. Phys. B **67**, 151-156 (1998)

[Lau70] R.A. Laudise, *The growth of single crystals*, Prentice-Hall, Inc., Englewood Cliffs, New Jersey (1970)

[Lay75] C.B. Layne, *Multiphonon relaxation and excitation transfer in rare earth-doped glasses*, Ph.D. thesis, University of California, Davis (1975)

[Lay77] C.B. Layne, W.H. Lowdermilk, M.J. Weber, *Multiphonon relaxation of rare earth ions in oxide glasses*, Phys. Rev. B **16**, no. 1, 10-17 (1977)

[Lei81] M. Leiss, Halbleitende *Seltenerdsesquisulfide: Herstellung, optische Verstaerkung und Wechselwirkung zwischen Band-, 5d- und 4f-Zustaenden*, PhD thesis, Universitaet Hamburg (1981)

[Loe03] H.V.D. van Loef, P. Dorenbos, C.W.E. van Eijk, K.W. Kraemer, H.U. Guedel, *Influence of the anion on the spectroscopy and scintillation mechanism in pure and Ce^{3+}-doped KLa_2X_5 and LaX_3 (X= Cl, Br, I)*, Phys. Rev. B **68**, 045108-1-9 (2003)

[Mcc78] R.A. McClatchey, R.W. Fenn, J.E.A. Selby, F.E. Volz, J.S. Garing, *Optical properties of the atmosphere* in Handbook of Optics, W.G. Driscoll (ed.), W. Vaughan (asc. ed.), Optical Society of America, McGraw-Hill book company, New York, 14.1-14.65 (1978)

[Mea84] R.M. Measures, *Laser remote sensing, fundamentals and applications*, Krieger Publishing Company, Florida (1984)

[Men04] A. Mendioroz, R. Balda, M. Voda, M. Al-Saleh, J. Fernandez, *Infrared to visible and ultraviolet upconversion processes in Nd^{3+} -doped potassium lead chloride crystal*, Opt. Mat. **26**, 351-357 (2004)

[Miy70] T. Miyakawa, D.L. Dexter, *Phonon sidebands, multiphonon relaxation of excited states, and phonon-assisted energy transfer between ions in solids*, Phys. Rev. B **1**, no. 7, 2961-2969 (1970)

[Mya99] S.V. Myagkota, *Reflection spectra and luminescence-kinetic parameters of perovskite-like $A_mPb_nBr_p$ crystals (A=Cs, Rb, K; m=1, 4; n=1,2; p=3,5,6), J. Phys. Stud. **3**, no. 2, 213-223 (1999)*

[Nie64] C.W. Nielsen, G.F. Koster, *Spectroscopic coefficients for p^n, d^n, f^n configurations*, M.I.T. Press, Cambridge, Mass. (1964)

[Nik91] M. Nikl, K. Nitsch, I. Velicka, J. Hybler, K. Polák, T. Fabian, *Photoluminescence of KPb_2Cl_5*, Phys. Stat. Sol. (b) **168**, K37-K42 (1991)

[Nit93] K. Nitsch, M. Rodova, *Differential thermal analysis study of lead bromide*, J. Crys. Growth **134**, 386-387 (1993)

[Nit95] K. Nitsch, M. Dušek, M. Nikl, K. Polák, M. Rodová, *Ternary alkali lead chlorides: crystal growth, crystal structure, absorption and emission properties*, Prog. Crystal Growth Charakt. **30**, 1-22 (1995)

[Nit96] K.Nitsch, V. Hamplová, M. Nikl, K. Polák, M. Rodová, *Lead bromide and ternary alkali lead bromide single crystals – growth and emission properties*, Chem. Phys. Letters **258**, 518-522 (1996)

[Nos00a] M.C. Nostrand, R.H. Page, S.A. Payne, W.F. Krupke, P.G. Schunemann, L.I. Isaenko, *Laser demonstrations of rare earth ions in low-phonon chloride and sulfide crystals*, Advanced Solid State Lasers, H. Injeyan, U. Keller, C. Marshall (eds.), OSA TOPS 34, Opt. Soc. Am., 459-463 (2000)

[Nos00b] M.C. Nostrand, New *Mid-IR Lasers based on rare earth-doped sulfide and chloride materials*, Ph.D. Dissertation, Lawrence Livermore National Laboratory, U.S. Department of Energy (2000)

[Nos01] M.C. Nostrand, R.H. Page, and S.A. Payne, L.I. Isaenko, A.P. Yelisseyev, *Optical properties of Dy^{3+}- and Nd^{3+}-doped KPb_2Cl_5*, J. Opt. Soc. Am. B **18**, no. 3, 264-276 (2001)

[Nos02] M.C. Nostrand, Lawrence Livermore National Laboratory, UC California, USA, unpublished results (2002)

[Nos98] M.C. Nostrand, R.H. Page, S.A. Payne, W.F. Krupke, *Spectroscopic data for infrared transitions in $CaGa_2S_4:Dy^{3+}$ and $KPb_2Cl_5:Dy^{3+}$*, Advanced Solid State Lasers, W.R. Bosenberg, M.M. Fejer (eds.), OSA TOPS 19, Opt. Soc. Am., 524-528 (1998)

[Nos99] M.C. Nostrand, R.H. Page, S.A. Payne, W.F. Krupke, P.G. Schunemann, L.I. Isaenko, *Room temperature $CaGa_2S_4:Dy^{3+}$ laser action at 2.43 and 4.31 μm and $KPb_2Cl_5:Dy^{3+}$ laser action at 2.43 μm*, Advanced Solid State Lasers, M.M. Fejer, H. Injeyan, U. Keller (eds.), OSA TOPS 26, Opt. Soc. Am., 441-449 (1999)

[Ofe62] G.S. Ofelt, *Intensities of crystal spectra of rare earth ions*, J. Chem. Phys. **37**, 511-520 (1962)

[Okh03] A.G. Okhrimchuk, L.N. Butvina, E.M. Dianov, N.V. Lichkova, V.N. Zavgorodnev, *Sensitization of MIR Tb^{3+} luminescence by Tm^{3+} ions in $CsCdBr_3$ and KPb_2Cl_5 crystals*, OSA TOPS 83, ASSP, J.J. Zayhowski (ed.), 303-308 (2003)

[Orl02] Y.V. Orlovskii, T.T. Basiev, I.N. Vorob'ev, E.O. Orlovskaya, N.P. Barnes, *Temperature dependencies of 3-5 phonon (4-6 μm) transitions in the YAG, LuAG and YLF crystals doped with trivalent holmium, thulium, and erbium*, Opt. Mat. **18**, 355-365 (2002)

[Pag97] R.H. Page, K.I. Schaffers, S.A. Payne, W.F. Krupke, *Dy-doped chlorides as gain media for 1.3 μm telecommunications amplifiers*, J. Lightwave Technol. **15**, no. 5, 786-793 (1997)

[Par67] W.D. Partlow, H.W. Moos, *Multiphonon relaxation in $LaCl_3:Nd^{3+}$*, Phys. Rev. **157**, no. 2, 252-256 (1967)

[Pay92] S.A. Payne, L.K. Smith, W.L. Kway, J.B. Tassano, W.F. Krupke, *The mechansim of Tm→Ho energy transfer in $LiYF_4$*, J. Phys.: Condens. Matter **4**, 8525-8542 (1992)

[Pay98] S.A. Payne, C. Bibeau, *Picosecond nonradiative processes in neodymium-doped crystals and glasses: mechanism for the energy gap law*, J. Lum. **79**, 143-159 (1998)

[Pfa52] W.G. Pfann, *Principles of zone-melting*, J. Metals, 747-753 (July, 1952)

[Pfl03] C. Pfluegl, W. Schrenk, S. Anders, G. Strasser, C. Becker, C. Sirtori, Y. Bonetti, A. Muller, *High temperature performance of GaAs- based bound-to-continuum quantum cascade lasers*, Appl. Phys. Lett. **83**, 23, 4698-4700 (2003)

[Pid97] M.S. Pidzynailo, S.V. Miagkota, A.S. Voloshinovskii, M.V. Kutsyk, *Vibronic interactions in $CsPbCl_{3x}Br_{3(1-x)}$ (x=0...1) and $CsPbCl_2I$ crystals*, Int. Soc. Opt. Eng. Proceedings of SPIE- the international society of Opt. Eng. 2967, USA (1997)

[Pla65] G.N. Plass, *Atmospheric phenomena*, Handbook of Military Infrared Techn., W.L. Wolfe (ed.), Office of Naval Research, Department of the Navy, Washington D.C. (1965)

[Poh32] R. Pohlman, *Ultrarotspektren von Ammoniumsalzen im Gebiet ihrer anomalen spezifischen Waerme*, Z. f. Phys. **79**, 394-420 (1932)

[Pow37] H.M. Powell, H.S. Tasker, *The valency angle of bivalent lead: The crystal structure of Ammonium, Rubidium, and Potassium Pentabromodiplumbites.*, J. Chem. Soc., 119-123 (1937)

[Pug76] L.A. Pugh, K.N. Rao, *Intensities from infrared spectra*, in Molecular Spectroscopy: Modern Research, Vol. II, K.N. Rao (ed.), Academic press, New York (1976)

[Qui03] R.S. Quimby, B.G. Aitken, *Mutliphonon energy gap law in rare earth-doped chalcogenide glass*, J. Non-Cryst. Sol. **320**, 100-112 (2003)

[Rac42] G. Racah, *Theory of complex spectra. II*, Phys. Rev. **62**, 438-462 (1942)

[Rad00] K. Rademaker, *Praeparation und Spektroskopische Charakterisierung von Yb^{2+} dotierten Fluoridkristallen*, Diplomarbeit (Diploma Thesis), 2000

[Red05] RedOptronics, www.redoptronics.com, 2005

[Red83] B.R. Reddy, P. Venkateswarlu, *Energy upconversion in $LaF_3:Nd^{3+}$*, J. Chem. Phys. **79**, no. 12, 5845-5850 (1983)

[Ree73] E.D. Reed, H.W. Moos, *Multiphonon relaxation of excited states of rare earth ions in YVO_4, $YAsO_4$, and YPO_4*, Phys. Rev. B **8**, no.3, 980-987 (1973)

[Rei21] O. Reinkober, Ultrarote *Absorptionsspektren fester Substanzen in duennen Schichten*, Z. f. Phys. **5**, 192-197 (1921)

[Rei77] R. Reisfeld, C.K. Jorgensen, *Laser and excited states of rare earths*, Springer, Berlin (1977)

[Ren00] Q. Ren, L.Q. Liu, Z.G. Wang, X.S. An, G.H. Zhang, D. Xu, *Refractive index and absorption of lead bromide crystals*, Materials Research Bulletin **35**, 471-476 (2000)

[Ric63] I. Richman, R.A. Satten, F.Y. Wong, *Lattice vibrations of $LaCl_3$ and $LaBr_3$ from vibronic spectra*, J. Chem. Phys. **39**, 1833-1846 (1963), note [Ric64]

[Ric64] I. Richman *et al.*, *Erratum: Lattice vibrations of $LaCl_3$ and $LaBr_3$ from vibronic spectra*, J. Chem. Phys. 40, 1451 (1964)

[Ris67] L.A. Riseberg, H.W. Moos, *Multiphonon Orbit-lattice relaxation in $LaBr_3$, $LaCl_3$, and LaF_3*, Phys. Rev. Letters **19**, no. 25, 1423-1426 (1967)

[Ris68] L.A. Riseberg, H.W. Moos, *Multiphonon orbit-lattice relaxation of excited states of rare earth ions in crystals*, Phys. Rev. **174**, no. 2, 429– 438 (1968)

[Rot59] M. Rotenberg, R. Bivens, N. Metropolis, J.K. Wooten, *The 3-j and 6-j symbols*, Techn. Press, M.I.T., Cambridge, MA (1959)

[Roy03] U.N. Roy, Y. Cui, M. Guo, M. Groza, A. Burger, G.J. Wagner, T.J. Carrig, S.A. Payne, *Growth and characterization of Er-doped KPb_2Cl_5 as laser host crystal*, J. Cryst. Growth **258**, 331-336 (2003)

[San98] J.S. Sanghera, I.D. Aggarwal, *Infrared Fiber Optics*, CRC Press, Boca Raton (1998)

[Sch73] P. Schuster, *Ligandenfeldtheorie*, Verlag Chemie GmbH, Weinheim 1973

[Sch80] H.L. Schläfer und G. Gliemann, *Einführung in die Ligandenfeldtheorie*, 2nd ed., Akademische Verlagsgesellschaft Wiesbaden 1980

[Sch88] F. Schwabl, *Quantenmechanik*, Springer-Verlag, Berlin-Heidelberg-New York 1988

[Sch99] T. Schweizer, B.N. Samson, J.R. Hector, W.S. Brocklesby, D.W. Hewak, D. N. Payne, *Infrared emission and ion-ion ineractions in thulium- and terbium-doped gallium lanthanum sulphide glass*, J. Opt. Soc. Am. B **16**, no. 2, 308-316 (1999)

[Sha01] L.B. Shaw, B. Cole, P.A. Thielen, J.S. Sanghera, I.D. Aggarwal, *Mid-wave IR and long-wave IR laser potential of rare earth-doped chalcogenide glass fiber*, IEEE J. Quant. Electr. **48**, no. 9, 1127-1136 (2001)

[Sha63] L.G. de Shazer, G.H. Dieke, *Spectra and energy levels of Eu^{3+} in $LaCl_3$*, J. Chem. Phys. **38**, no. 9, 2190-2199 (1963)

[She03] N. Shebanin, A.P. Yelisseyev, L.I. Isaenko, Design and Technological Institute for Monocrystals, Novosibirsk, Russia, unpublished results (2003)

[Sve89] O. Svelto, *Principles of lasers*, 3rd ed., Plenum Press, New York 1989

[Tig01] P.Y. Tigréat, J.L. Doualan, R. Moncorgé, B. Ferrand, *Spectroscopic investigation of a 1.55 μm emission band in Dy^{3+}-doped $CsCdBr_3$ and KPb_2Cl_5 single crystal*, J. Lum. **94-95**, 107-111 (2001)

[Tka02a] A.M. Tkachuk, S.E. Ivanova, L.I. Isaenko, A.P. Yelisseyev, D.I. Mironov, M.C. Nostrand, R.H. Page, S.A. Payne, *Spectroscopic properties of TR^{3+}-doped double chloride crystals*, Proc. SPIE **4766**, 22-36 (2002)

[Tka02b] A.M. Tkachuk, S.E. Ivanova, L.I. Isaenko, A.P. Yelisseyev, S.A. Payne, R. Solarz, R.H. Page, M.C. Nostrand, *Spectroscopic study of neodymium-doped potassium lead double chloride Nd^{3+}:KPb_2Cl_5 Crystals*, Opt. Spectr. **92**, no. 1, 83-94 (2002)

[Tka03] A.M. Tkachuk, S.E. Ivanova, L.I. Isaenko, A.P. Yelisseyev, M.-F. Joubert, Y. Guyot, S.A. Payne, *Spectroscopic studies of erbium-doped potassium lead double chloride crystals KPb_2Cl_5:Er^{3+}. 1. Optical spectra and relaxation of the erbium excited states in potassium-lead double chloride crystals*, Opt. Spectr. **95**, 722-740 (2003)

[Tka99a] A.M. Tkachuk, S.E. Ivanova, L.I. Isaenko, A.P. Yelisseyev, W.F. Krupke, S.A. Payne, R. Solarz, M.C. Nostrand, R.H. Page, *Dy^{3+}-doped KPb_2Cl_5 crystal of double chlorides and double fluorides as the active media of IR solid state lasers and telecommunication amplifiers*, J. Opt. Technol. **66**, no. 5, 460-462 (1999)

[Tka99b] A.M. Tkachuk, S.E. Ivanova, L.I. Isaenko, A.P. Yelisseyev, R. Solarz, M.C. Nostrand, R.H. Page, S.A. Payne, *Comparative spectroscopic study of the Dy^{3+} doped double chloride and double fluoride crystals for telecommunication amplifiers and IR lasers*, Act. Phys. Polonica A **95**, no. 3, 381-394 (1999)

[Vod04] M. Voda, M. Al-Saleh, G. Lobera, R. Balda, J. Fernandez, *Crystal growth of rare earth-doped ternary potassium lead chloride single crystals by the Bridgman method*, Opt. Mat. **26**, 359-363 (2004)

[Web67] M.J. Weber, *Probabilities for radiative and nonradiative Decay of Er^{3+} in LaF_3*, Phys. Rev. **157**, no. 2, 262-272 (1967)

[Web68] M.J. Weber, *Radiative and multiphonon relaxation of rare earth ions in Y_2O_3*, Phys. Rev. **171**, no. 2, 283-291 (1968)

[Web72] M.J. Weber, B. Matsinger, V.L. Donlan, G.T. Surratt, *Optical transition probabilities for trivalent Holmium in LaF_3 and $YAlO_3$*, J. Chem. Phys. **57**, 562-567 (1972)

[Web73] M.J. Weber, *Multiphonon Relaxation of rare earth ions in Yttrium Orthoaluminate*, Phys. Rev. B **8**, no. 1, 54-64 (1973)

[Web86] M.J. Weber, CRC Handbook of Laser Science and Technology, Supplement 2: Optical Materials, CRC Press, London (1986)

[Wic99] C. Wickleder, personal communication, Universität zu Köln (1999)

[Wyb61] B.G. Wybourne, *Composition of the electronic states of Nd(IV) and Er(IV)*, J. Chem. Phys. **34**, no. 1, 279-281 (1961)

[Wyb65] B.G. Wybourne, *Spectroscopic properties of rare earths,* Interscience Publishers John Wiley&Sons, Inc., New York-London-Sydney 1965

[Yel02] A.P. Yelisseyev, personal communication (2002)

Appendix

Appendix A

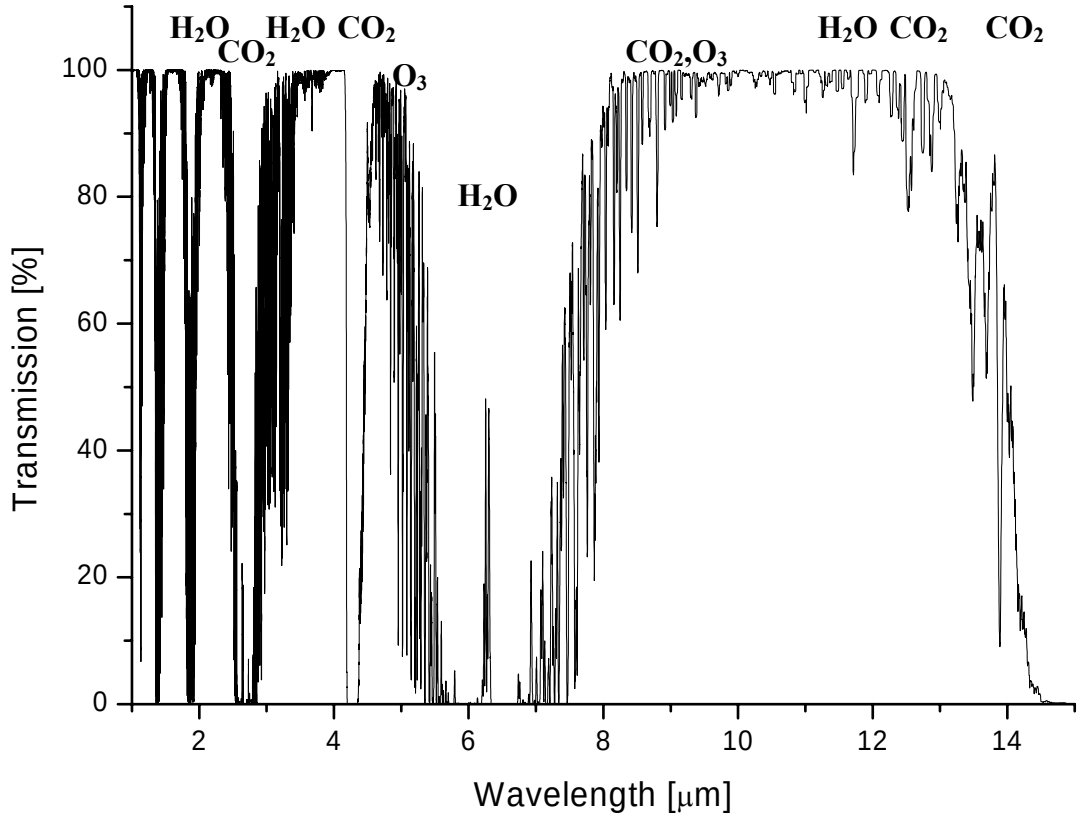

Figure A-1. *Smoothed spectral transmission of the atmosphere, transmission of 300 m horizontal, air path at sea level, T= 296 K (calculated with Hitran [Hit00] database). Some of the absorbing molecules are indicated [Mea84].*

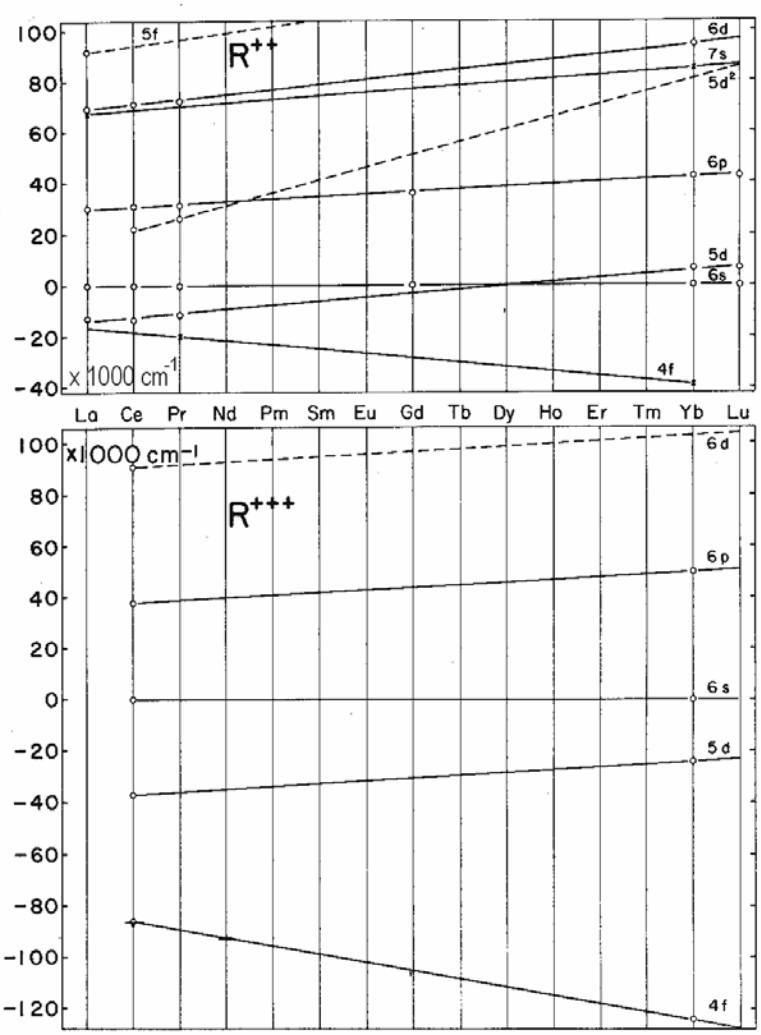

Figure A-2. *Relative positions of the" energetic centroids" [Die68] of some configurations for divalent and trivalent rare earth ions (empirical data). As can be seen the spacing of the 4f and 5d configuration is much closer in the divalent case than in the trivalent case.*

Appendix B

1. The **fractional thermal population factor** $X_a(T)$ of the initial level a can be determined by using the formula for the Boltzmann distribution:

$$X_a(T) = \frac{g_a \exp(-\Delta E_a / kT)}{\sum_b g_b \exp(-\Delta E_b / kT)} \text{ [Goe98],} \qquad \text{(B-1)}$$

where g_a and g_b are the degeneracies of level a and b, k the Boltzmann`s constant, T the temperature and ΔE_b the energy difference between level b and the ground state. In principle the summation runs over all energy levels of the $4f^n$ configuration, but in principle contributions from higher lying states are small if $\Delta E >> kT$. In this formula the level a can be both a crystal field Stark level or a $^{2S+1}L_J$ level. In the latter case the degeneracy is 2J+1.

2. A general measure of the **relative error of the fit in the Judd-Ofelt calculation** is given by the quotient rmsΔS/rmsS [Bea90] where the rmsΔS is defined as

$$rms\Delta S = \sqrt{\frac{\sum (\Delta S)^2}{no.\ of\ transitions - 3}} \qquad \text{(B-2)}$$

and ΔS is the difference between the measured and calculated line strength S values. The number 3 indicates that three parameters are involved. Typically, the relative error is within the range of 5-25%.

Appendix C

Here, the derivation of equation 2-4 in the experimental pump-probe section 2.2.6 is described.

The signal intensity I_u in absence of the pump beam is given by Lambert-Beer's-law (Eqn. 2-1, section 2.2.2):

$$I_u = I_0 \cdot e^{-\sigma_{GSA} \cdot n_{ion} \cdot l} \tag{C-1}$$

The signal intensity I_p in presence of the pump beam measures amplification of the probe beam by stimulated emission (em) as well as excited state absorption (ESA) and reabsorption (RA) in addition to the ground state absorption (GSA):

$$I_p = I_0 \cdot e^{-\sigma_{GSA}(n_{ion}-n_e)\cdot l + (\sum_i \frac{n_i}{n_e}(\sigma_{em,i}-\sigma_{ESA/RA,i}))\cdot n_e \cdot l} \tag{C-2}$$

Here, σ_{em}, $\sigma_{ESA,RA}$, σ_{GSA} are the cross sections, l the transmission length (=thickness of crystal), n_{ion} is the ion density in the crystal, n_i the population density of level i and $n_e = \Sigma n_i$ the total excitation density summed over all excited levels i.

Dividing I_u by I_p and taking the logarithm gives:

$$\ln(\frac{I_u}{I_p}) = n_e \cdot l \cdot [-\sigma_{GSA} + \sum_i \frac{n_i}{n_e}(\sigma_{ESA/RA,i} - \sigma_{em,i})] \tag{C-3}$$

With the assumption of small changes in transmission this logarithm can be set in first approximation equal to the measured signals described above:

$$-\ln(\frac{I_u}{I_p}) = \ln[1 + (\frac{I_p - I_u}{I_u})] \approx \frac{I_p - I_u}{I_u} \tag{C-4}$$

This is valid in the case of small pump power densities meaning when the number of excited ions is small compared to the ion density in the crystal.

The following formula shows that if ESA and/or RA predominates the measured signal is negative while the signal is positive due to GSA and/or stimulated emission:

$$\frac{I_p - I_u}{I_u} = C \cdot n_e \cdot l \cdot [\sigma_{GSA} + \sum_i \frac{n_i}{n_e}(\sigma_{em,i} - \sigma_{ESA/RA,i})] \tag{C-5}$$

In general the constant C or the factor $A = C \cdot n_e \cdot l$ can be determined in the spectral region where no ESA is assumed to occur and the cross sections of ground state absorption and stimulated emission are known. Further details are given in Koetke [Koe95].

Appendix D

Table D: *The energetic positions of the Stark levels for $KPb_2Br_5:Nd^{3+}$ (uncertain values are written in brackets). Note, that these positions could still change by including further results such as polarization dependent spectra. The values were determined by transmission measurement (spectral resolution: 0.08 nm) if not otherwise noted.*

Multiplet (no. of levels expected)	Stark level positions [cm^{-1}]	no. of levels found
$^4I_{9/2}$ (5)	[a] 0, 25, 73, 138, 254	5
$^4I_{11/2}$ (6)	[a] 1912, 1929, 1943, 1986, 2036, 2066	6
$^4I_{13/2}$ (7)	[a] 3874, 3886, 3899, 3927, 4001, 4025, 4049	7
$^4I_{15/2}$ (8)	[a] ((5817), (5830), 5855, 5869, 5903, 5951) 6076, 6094, 6116, 6150	4+(4) +((2))
$^4F_{3/2}$ (2)	11278, 11323	2
$^4F_{5/2}$ (3)	12297, 12336, 12371	3
$^2H_{9/2}$ (5)	12434, 12487, 12507, 12556, 12586	5
$^4F_{7/2}$ (4)	13254, 13271, 13285, 13314	4
$^4S_{3/2}$ (2)	13393[b], 13397	2
$^4F_{9/2}$ (5)	14519, 14552, 14581, 14639, 14661	5
$^2H_{11/2}$ (6)	15777, 15800, (15856), 15893	3+(1)
$^4G_{5/2}$ (3)	16766, 16876, 16912	3
$^2G_{7/2}$ (4)	17057, (17100), 17114, 17163	3+(1)
$^2K_{13/2}$ (7)	-[c]	-
$^4G_{7/2}$ (4)	18744, 18784, 18810, 18831	4
$^4G_{9/2}$ (5)	19175, 19210, 19266, (19332), (19362), (19521), (19616)	3+(4)
$^2K_{15/2}$ (8) $^2G_{9/2}$ (5) $^2D_{3/2}$ (2) $^4G_{11/2}$ (6)	20788, 20810, 20838, 20850, (20897), 20956, 20980, 20989, 21079, 21096; also observed[d]: 20799, 20826, 20875, 20945, 20962, 21076, 21262, 21346, 21364, 21426, 21470, 21493, 21574, 21601	
$^2P_{1/2}$ (1)	22979	1
$^2D_{5/2}$ (3)	[d]23492, 23567	2
$^2P_{3/2}$ (2)	-	-
$^4D_{3/2}$ (2) $^4D_{5/2}$ (3)	[d]27569, 27704, 27796, 27871	4
$^2I_{11/2}$ (6)	-	-
$^4D_{1/2}$ (1)	[d]28115	1

[a] Mainly determined by emission measurement (spectral resolution: 0.32 nm).

[b] Determined by comparing the splitting with the data from Nd^{3+} in $LaBr_3$ [Ric62] and $LaCl_3$ [Rei77]. There is another possible peak at 13379 cm^{-1}.

[c] Values uncertain, $^2K_{13/2}$ peaks might be overlapped by the peaks of the $^4G_{7/2}$ multiplet.

[d] Peaks measured by additional transmission or excitation measurements with a resolution of ~ 0.32 nm.

Acknowledgments

I am grateful for the support from the Universität Hamburg (UH), Hamburg, Germany and from the Lawrence Livermore National Laboratory, Livermore (LLNL), CA, USA over the past three years of this PhD thesis. This includes the support of the Deutsche Forschungsgemeinschaft within the frame of the Graduierten-Kolleg no. 463, the support of National Science Foundation grants DMR-0097272 and HER-0090526, Basic Energy Sciences Grants to LLNL, and the support through the LLNL Research Collaborations Program for HBCUs & MIs under grant DE-FG03-94SF20368.

I would like to thank Prof. Dr. Günter Huber for giving me the possibility to make my PhD at the University of Hamburg, for his support and his trust to do research also at LLNL, and especially for his advice and his reliability over the past years of my Master and PhD thesis studies.

I would like to thank Dr. Stephen A. Payne for the possibility to do research at LLNL, for his support and confidence in me, and therefore, that I could count on him at any time. I am especially grateful for his advice and thoughts regarding my research and growth as a scientist over the past years of my PhD thesis studies.

I would like to thank Dr. William F. Krupke (LLNL) for the input he provided toward this work. I am grateful for his advice, encouragement and participation in this project over the years of my research.

I am very pleased to acknowledge the support of Prof. Dr. Ernst Heumann (UH). I am especially grateful for his contribution to the achievement of laser activity. I am thankful for the "open door policy" from Dr. Klaus Petermann (UH) and his advice, especially in material aspects and crystal growth. Both of them I would like to thank for their participation on proof-reading of this thesis.

This project depends on collaborative efforts, especially in the area of crystal growth. I am grateful to:

- Prof. Dr. Arnold Burger (Center for Photonic Materials and Devices, Department of Physics, Fisk University, TN, USA),
- Prof. Dr. Ludmila I. Isaenko and Dr. Alexander P. Yelissejev (Design and Technological Institute for Monocrystals, Novosibirsk, Russia),
- Dr. Krishna C. Mandal (EIC Laboratories, Inc., MS, USA),
- Dr. Karel Nitsch (Institute of Physics, Academy of Sciences of the Czech Republic, Prague, Czech Republic).

I am thankful to Prof. Dr. Alexandra Tkachuk (SI Vavilov State Optical Institute, St. Petersburg, Russia) regarding our collaboration within the upconversion studies.
I greatly appreciate the advice regarding spectroscopy from Dr. Stefan Kück (Physikalisch-Technische Bundesanstalt, Germany), Dr. Mike Nostrand (LLNL), and Dr. Eugen Osiac (also regarding his support with lifetime measurements within the upconversion studies; Institute of Atomic Physics, Bucharest, Romania).
I am thankful to Dr. John J. Adams (also regarding the CO_2-laser transmission measurement, LLNL), Dr. Andy J. Bayramian (LLNL), Dr. Raymond J. Beach (LLNL), Dr. Chris Ebbers (LLNL), Dr. Dione Fagundes-Peters (UH), Dr. Ralph H. Page (LLNL), Dr. Volker Peters (Europaeisches Patentamt, Den Haag), and Dr. Kathleen I. Schaffers (LLNL) for their advice e.g. regarding spectroscopy, crystal growth, and/or material properties.
I am grateful for the polishing service of Peter Thelin (LLNL), as well as the concentration measurements of Fowzia Zaka (LLNL) and Beate Cornelisen (UH). Thanks a lot to Everett Utterback (LLNL) regarding his help with the equipment programming. I acknowledge the help from Dr. Annalehne Dethlefsen (UH) with the Raman scattering spectra. I would like to thank Robert Fischer (UH), Alexander D. Drobshoff, V. Keith Kanz, Scott C. Mitchell, Joel A. Speth, and John B. Tassano (LLNL) for technical advice and/or supply of equipment, especially during the time of the move of my lab at LLNL. Special thanks go to Silke Frömmig (UH), Dolores Lambert (LLNL), and Dustin Riggs (LLNL) regarding their administrative support.
I am grateful for the support and the cheering up of many more members of the NIF Directorate, LLNL, USA and the Institute of Laser Physics, University of Hamburg, Hamburg, Germany.
Finally, I would like to thank friends and family (including my “American family”) for their encouragement and support. I am especially grateful for the support and love of my parents.

LLNL's portion of this work was performed under the auspices of the U.S. Department of Energy by the University of California at Lawrence Livermore National Laboratory under contract W-7405-Eng-48.